Investigation of rare-earth pyrochlore thin films

Stephen Mann

University College London

Thesis submitted for the degree of

Doctor of Philosophy

30th September 2022

Declaration

I, Stephen Mann do solemnly swear that the work I have presented in this thesis is my own. Where information has been derived from other sources, I confirm that this has been indicated in the thesis.

Abstract

This thesis reports on a number of systematic studies that were carried out on thin films of spin ice and its related materials. Specifically, three series were carried out: a thickness series and an epitaxial strain series reporting on $Yb_2Ti_2O_7$ thin films; a series investigating the thickness-dependence of $Tb_2Ti_2O_7$ films' specific heat; and lastly, a characterisation of thick $Dy_2Ti_2O_7$, $Tb_2Ti_2O_7$ and $Yb_2Ti_2O_7$ films. The epitaxial strain series of $Yb_2Ti_2O_7$ showed that fully strained films of $Yb_2Ti_2O_7$ could be grown on $Y_2Ti_2O_7$ substrates with an out-of-plane crystal direction of $[1\bar{1}0]$ and [100]. The thickness series was carried out on films with an out-of-plane crystal direction of [111], but it is shown that this particular orientation is more challenging to grow fully strained films along because in all instances the films were relaxed. The aim of the $Tb_2Ti_2O_7$ series was to investigate the nature of the films' ground states, which have been subject to debate in the bulk. Single-ion model fittings imply that the ground state of the $Tb_2Ti_2O_7$ thin films is a doublet state. The thick film series shows that a fully strained $Dy_2Ti_2O_7$ film was grown, but that the other films created additional phases and, in the case of $Tb_2Ti_2O_7$, did also relax. Specific heat measurements reveal that the thick $Dy_2Ti_2O_7$ film has recovered some but not all of its residual entropy, which is seen in the bulk. This means that the phase grown is both different to the previous thin films grown and to the bulk. Fits to M vs H measurements give a magnetic moment of 9.4(1) μ_B, which is within error of the bulk.

Impact Statement

The modern world of today has been built upon thin film technology and electricity. The research presented in this thesis aims to contribute to this and hopefully help usher in another key element to the future of our technology, magnetricity. Spin ice and its related materials, which are investigated in this work, are given by $RE_2Ti_2O_7$ where RE represents the rare-earth ions Dy, Tb and Yb. These materials share an almost identical pyrochlore structure, and exceptionally high quality thin films of $Dy_2Ti_2O_7$ and $Tb_2Ti_2O_7$ films have already been grown on the non-magnetic pyrochlore $Y_2Ti_2O_7$. Spin ice materials have been shown to display excitations that are equivalent to magnetic monopoles, which were thought to be impossible to find in nature. Magnetricity is the flow of magnetic monopoles or magnetic charges. Our current world has been drastically changed since we harnessed the power of flowing electric charges. It could be possible that our world will be changed once more if we can harness flowing magnetic charges. For this future to be possible, greater understanding of spin ice and its related materials' exotic phenomena needs to be acquired. Thin films of these materials offer a perturbed perspective on these phenomena, which will help to improve our understanding of these excitations. From a practical standpoint, it is likely that technology in the present and future will continue to use and benefit from thin film research.

Acknowledgements

My PhD journey has been challenging, but made possible and most special by the wonderful people who I have met and who have supported me. Beginning right at my beginning, I would like to thank my mother who throughout my life has been my most fervent supporter and who has always encouraged me to strive to be the very best version of myself in all aspects of my life. It goes without saying, though I shall say it, I do not think I would ever have reached this point without her love and her willingness to always go above and beyond to help me, even at times at her own expense. You have been the wind beneath my wings all my life! I would next like to thank my friend and postdoc Dr. Daan Arroo who arrived onto the scene not long after my traumatising transfer viva. I would like to thank him for being such a wonderfully reassuring presence who helped pick up the pieces. From our conversations all over UCL, in numerous cafes and many Chinese restaurants, you have expanded my interests and given me so much to think about. There are very few people whose opinions I respect as much as yours, even when we disagree! I hope we are always able to stay in contact as I enjoy talking with you so much. My supervisor, Prof. Steven Bramwell, has made this difficult journey enjoyable and is such an inspiration to me. From the very beginning, I have been in awe of his mind, his humility and his understanding. Thank you for spending so much time talking to me about literally anything that I find interesting. I shall strive to see the world in a similarly sophisticated way. I think it is only right that I also thank Steves wife for letting me keep him at times late into the evening so we could have those important conversations, sometimes physics ones too! My PhD has been special because I have had him as my supervisor and I hope that as I move on from being a student we can be friends, though I would already consider us that. Lastly, I would like to thank all of my unnamed friends and family who have been supportive and kept my spirits up throughout this journey.

Contents

List of Figures

List of Tables

Chapter 1

Introduction

Frustrated magnetism is a field in condensed matter physics that has been active for over fifty years and to this day it continues to interest experimentalists and theoreticians [1, 2]. Frustrated magnetism arises when two competing interactions are unable to be simultaneously satisfied. This can take the form of two or more competing magnetic interactions such as ferromagnetic and anti-ferromagnetic exchange. Another cause is *geometric frustration*, which arises when the crystal structure prevents magnetic ordering. This typically occurs in systems containing triangles or tetrahedra of spins.

1.1 Geometric frustration

Geometric frustration can lead to high ground state degeneracy, which enables the magnet's spins to continuously switch their orientation. The simplest example of a geometrically frustrated system is an antiferromagnetic triangle of spins. In an antiferromagnetic system, all the spins are orientated such that they point in the opposite direction to one another. This results in a zero net magnetisation. The problem is that in an antiferromagnetic triangle of spins there is an odd number of spins, which prevents the spins from cancelling completely. An antiferromagnetic triangle of spins has a degenerate ground state because there are six possible configurations which have the lowest energy; these are shown in Figure 1.1 [2]. For this reason, antiferromagnetic materials with triangular symmetry often display degenerate ground states. The degree of ground state degeneracy is reduced in real materials compared with triangles of spins due to corner-sharing in lattices. A number of magnetic phases arise from geometrically frustrated magnetism, including spin ice, quantum spin ice, spin liquids and quantum spin liquids.

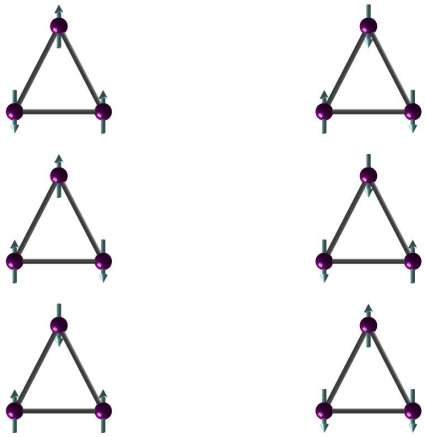

Figure 1.1: Ground states for an antiferromagnetic triangle of spins, where the circles represent the atoms and the arrows represent the direction of the atoms' spins.

1.2 Water ice

The first known example of a frustrated system is water ice, which was studied by Pauling (Fig. 1.2a). He applied a set of rules to describe the structure of water ice called the ice rules. These rules state: each oxygen atom is attached to two hydrogen atoms, with a bond angle of ≈ 105 °; these hydrogen atoms must point towards two of the four surrounding oxygen atoms; between each pair of oxygen atoms there can be only one hydrogen atom. Under normal conditions, none of the configurations that satisfy the above rules can be stabilised from interactions with non-adjacent molecules [3].

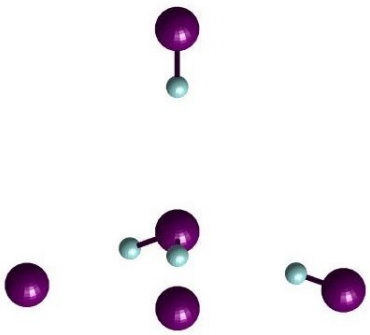

(a) The relative positions of oxygen atoms and hydrogen atoms in a tetrahedron of water ice.

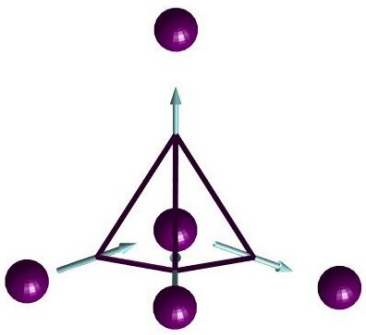

(b) The direction of effective spins corresponding to the hydrogen and oxygen positions in (a).

Figure 1.2: The relative hydrogen positions (blue circles) in water ice can be mapped onto effective spins (blue arrows) positioned at the midpoints of oxygen-oxygen bonds (purple circles).

Pauling calculated the degeneracy of the ground state of water ice. Using the ice rules stated above, each oxygen atom has a total of six configurations of two-near and two-far hydrogen atoms. There is a 50 % chance for an oxygen atom to have a nearby hydrogen atom and a 50 % chance for it to have a far away hydrogen atom; these probabilities apply to all oxygen atoms. Only 25 % of the total six configurations are allowed because adjacent oxygen atoms require one oxygen atom to have a nearby hydrogen and the other to have a far away hydrogen [3]. For N atoms $\Omega = \left(\frac{6}{4}\right)^N = \left(\frac{3}{2}\right)^N$ microstates with a ground state entropy of $S = R\ln\left(\frac{3}{2}\right)$ per mole of water molecules.

1.3 Spin ice

Spin ice is a class of frustrated magnet that obeys the ice rules. Spin ice has a pyrochlore structure consisting of two inter-penetrating lattices of corner-sharing tetrahedra (Fig. 1.3), one of titanium ions (which have weak Van Vleck paramagnetism) and one of rare-earth ions (which are strongly paramagnetic). In the spin ice phase the spins can be treated as Ising-like, pointing towards the centre of the rare-earth corner-sharing tetrahedra or out from their centres (see Fig. 1.2b). The most energetically favourable state at low temperature has two spins pointing in and two pointing out. This is known as the 'two-in two-out' phase, which is analogous to the two-near and two-far hydrogen atom phase in water ice; materials that exhibit this magnetic phase are called spin ices. The orientation of the spins in this phase can be mapped onto the relative positions of hydrogen and oxgyen atoms in water ice by converting the displacement between hydrogen atoms and their closest oxygen atoms into spins, which point towards the closest oxygen atoms. Spin ice materials' spins freeze below 0.5 K and (in simulations but not in experiment) order at around 0.1 - 0.2 K. This spin-freezing effect is caused by a single spin flip, requiring at least another five spins to flip simultaneously, to maintain the two-in two-out rule. When the temperature drops sufficiently low, the energy barrier to flip six spins simultaneously becomes too great.

There are three characteristic experimental features of spin ice, which when found together can identify a spin ice phase without needing to do neutron scattering. One of these features involves measuring different, and unusually large, saturation magnetisations, when a field is applied along different crystal directions. Secondly, after demagnetisation corrections have been accounted for, spin ice phases depart in a systematic way from the Curie law, $\chi = \frac{C}{T}$, as a function of temperature [4]. Lastly, the magnetic entropy of spin ices increase

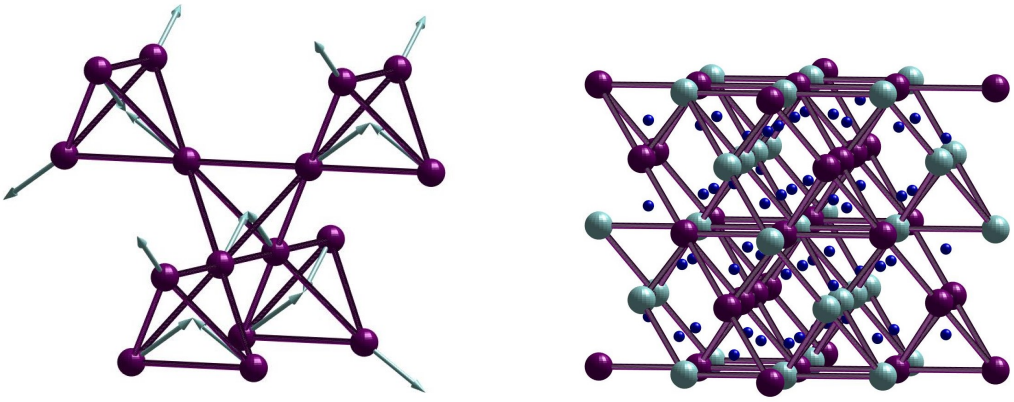

(a) A lattice of corner-sharing tetrahedra with spins, obeying the ice rules.

(b) The structure of $A_2B_2O_7$ spin ice materials.

Figure 1.3: (a) The corner-sharing tetrahedra structure found in spin ice materials with its spins obeying the ice rules. (b) The structure of spin ice materials that possess a chemical formula given by $A_2B_2O_7$. The blue, light blue and purple spheres represent oxygen, titanium and rare-earth ions respectively. The cylinders, connecting the rare-earth ions, have no physical significance and are only present to highlight the corner-sharing tetrahedra structure.

with temperature from the low temperature entropy of $S(0) = \left(\frac{R}{2}\right)\ln\left(\frac{3}{2}\right)$ to $S(T > 10\text{K}) = R\ln(2)$ per mole of rare-earth ion [4].

1.4 Quantum spin ice

Quantum spin ices have a more complex magnetic phase whose defining feature is that the spins can change their orientation and superimpose at very low temperatures. This process involves flipping a ring of 6 spins, the smallest loop possible, such that ice rules are still obeyed. The energy barrier for this new state is too large to overcome without quantum tunnelling. Materials that maintain ice rules and rely on quantum tunnelling to change their low temperature states are called quantum spin ices.

1.5 Spin liquids

A spin liquid's spins are able to fluctuate in the same fashion as in spin ice materials, without needing to adhere to the ice rules. There are two ways spins can fluctuate in a spin liquid: classical fluctuations, which are fluctuations that are driven by thermal energy and dominate large spins; and quantum fluctuations, which reflect the uncertainty principle and affect smaller spins, $S = \frac{1}{2}$. They involve zero-point motions, which are spin flips that are the same size as the spin. While classical fluctuations eventually stop at low

$k_{\mathrm{B}}T$, quantum fluctuations can continue down to $T = 0$ K. Spin liquids get their name from the comparison made between their spin behaviour and how molecules in liquids form highly dense correlated states with no static order. A quantum spin liquid is a material that has strong quantum fluctuations [2].

1.6 Thesis outline

The materials discussed in this thesis have a difference in rare-earth ion and are virtually identical in structure, having only a small difference in their unit cell size. These minor differences result in dramatically different properties and host a wide variety of rich exotic excitations such as magnetic monopoles and spinons. For this reason, there is great interest in trying to understand what mechanisms are responsible for causing these differences. The study of thin films adds another data point in this quest, by allowing the structural properties to be altered, while preserving their chemical makeup. This in essence creates a perturbation on the many different exotic excitations, which are present in this group of materials and dominate their properties.

This thesis reports on the findings of several systematic studies, in which thin films of spin ice and its related materials were epitaxially grown on $Y_2Ti_2O_7$ substrates and subsequently characterised. The films varied from a few monolayers in thickness to a nearly macroscopic dimension ("thick films"). The thin films grown were: the spin ice $Dy_2Ti_2O_7$, the quantum spin ice candidate $Yb_2Ti_2O_7$, and the quantum spin liquid candidate $Tb_2Ti_2O_7$. The characterisation of $Yb_2Ti_2O_7$ thin films is split into two series, characterised by thickness and epitaxial strain, which describes magnetometry, X-ray diffraction and heat capacity (Chapter 5). Thick films of $Dy_2Ti_2O_7$, $Yb_2Ti_2O_7$ and $Tb_2Ti_2O_7$ were characterised using the same techniques (Chapter 6). A study investigating the thickness-dependence of $Tb_2Ti_2O_7$'s heat capacity is made (Chapter 7). Lastly, neutron scattering measurements on the thick $Dy_2Ti_2O_7$ film are reported on (Chapter 8). Before describing the the experimental results, some background (Chapter 2), a literature review (Chapter 3) and a description of the thin film growth (Chapter 4) are given. At the end of the thesis, conclusions are drawn concerning the experimental results (Chapter 9).

Chapter 2

Background

2.1 Crystal field

The crystal field or Crystal Electric Field (CEF) arises from neighbouring atoms electric fields interacting with one another inside of a crystal. Each neighbouring atoms can be modeled as a point charge. As different orbitals have different shapes and charge distributions, the symmetry of the local environment inside of the crystal plays a significant role in determining the size and nature of the crystal field. The crystal field's influence is strongest along the direction of the orbital's angular momentum, but this does not directly affect the spins. A lower energy state involves the atom's orbitals pointing away from its neighbouring atoms and a higher energy state involves the atom's orbitals pointing towards its neighbouring atoms. This phenomena can cause an atom's degenerate energy levels in free space to be split when inside a crystal. However, this does not apply to materials with an odd number of electrons because they have time-reversal symmetry (Kramer's doublet), which prevents them from being split by an electric field; this includes the CEF. Both $Yb_2Ti_2O_7$ and $Dy_2Ti_2O_7$ have Kramer's doublets, but $Tb_2Ti_2O_7$ does not and so its degenerate states could be split by electric fields.

2.2 Spin ice models

2.2.1 Nearest-neighbour model

The first model that described spin ice behaviour was the ferromagnetic nearest-neighbour model, which consists of a ferromagnetic pyrochlore structure with a local [111] Ising anisotropy. This model can take on either a ferromagnetic or an antiferromagnetic phase. Frustration arises due to the combined effect of ferromagnetic coupling and single-ion anisotropy [5]. A more in-depth look into

the frustration generated in spin ices was conducted. In this paper four models are compared: a ferromagnetic pyrochlore with uniaxial anisotropy, a ferromagnetic pyrochlore with $\langle 111 \rangle$ anisotropy, an antiferromagnetic pyrochlore with uniaxial anisotropy and an antiferromagnetic pyrochlore with $\langle 111 \rangle$ anisotropy. Anderson originally used the models with uniaxial anisotropy to describe a diamond-like oxide lattice of cubic ice. It was discovered that both the $\langle 111 \rangle$ ferromagnetic model and Anderson's antiferromagnetic uniaxial model could be equivalently mapped onto the ice model, provided that the sign of the exchange coupling in the Anderson model was reversed. Anderson's model takes advantage of there being two oxide lattices that are identical but distinct, by treating opposite spins on different lattices as being equivalent. This means that an up-spin represents a 'proton near the oxygen atom' on one lattice and an up-spin on the other lattice represents a 'proton not near the oxygen atom'; the same logic follows for a down-spin [6]. A similar comparison can be made with the other two models. The problem with Anderson's model is that there is no direct connection between the spin directions and their positions. For this reason, Anderson's models are inferior to the other models. The ferromagnetic pyrochlore model with $\langle 111 \rangle$ anisotropy is the most dominant model and it is for this reason $Ho_2Ti_2O_7$ is a spin ice [7].

The first model used on spin ice is the Hamiltonian for the indirect exchange interaction between rare-earth ions and is shown below:

$$H = -J \sum_{(ij)} S_i^{\hat{z}_i} \cdot S_j^{\hat{z}_j}$$

where H is the Hamiltonian and J is the exchange energy. $S_i^{\hat{z}_i}$ *and* $S_j^{\hat{z}_j}$ correspond to spin vectors, which point along the local $\langle 111 \rangle$ axis given by $\hat{z}_i$ and $\hat{z}_j$ respectively. These spin vectors have a magnitude of 1. For each tetrahedron, the spins have the following normalised orientations:

$$\hat{S}_1 = \frac{(1,1,1)}{\sqrt{3}}$$

$$\hat{S}_2 = \frac{(-1,-1,1)}{\sqrt{3}}$$

$$\hat{S}_3 = \frac{(-1,1,-1)}{\sqrt{3}}$$

$$\hat{S}_4 = \frac{(1,-1,-1)}{\sqrt{3}}$$

The spin is either positive or negative depending on whether the spin is pointing into or out of the tetrahedron. These normalised spins result in:

$$S_{\mathrm{i}}^{\hat{z}_{\mathrm{i}}} \cdot S_{\mathrm{j}}^{\hat{z}_{\mathrm{j}}} = \pm\frac{1}{3}$$

where the negative sign corresponds to a lower energy interaction between one spin pointing out of a tetrahedron and one spin pointing into a tetrahedron. The positive sign corresponds to a higher energy interaction between two spins where they both point either out of a tetrahedron or into a tetrahedron. The lowest energy state for spin ice is, therefore, when two spins point into a tetrahedron and two spins point out of a tetrahedron [8].

2.2.2 Dipolar spin ice model

The first attempt at including dipole-dipole interactions in spin ice models was by Siddharthan *et al.* [9]. Before the dipolar spin ice model, only the nearest-neighbour model had been used. The type of materials Siddharthan investigated were $A_2Ti_2O_7$ pyrochlores, where A represents rare-earth metal ions. These materials have large magnetic moments from the rare-earth metal ions, which are strong enough to cause an appreciable dipolar interaction. When performing simulations, Siddharthan truncated the long-range dipolar interaction, which prevented each dipole from interacting with other dipoles that were further than five tetrahedra away. A follow-up paper by Hertog [10] simulated the dipolar spin ice model without truncating the dipolar interaction. Siddharthan's model showed a transition in the specific heat of $Ho_2Ti_2O_7$ from a paramagnetic state to a partially-ordered state. Hertog showed that this transition was eliminated if the range of dipolar interactions was increased beyond ten tetrahedra. Thus, it is believed that Siddharthan's attempt at including the dipolar interactions was incorrect.

The Hamiltonian for the dipolar spin ice model is shown below:

$$H = -J\sum_{(\mathrm{ij})} S_{\mathrm{i}}^{\hat{z}_{\mathrm{i}}} \cdot S_{\mathrm{j}}^{\hat{z}_{\mathrm{j}}} + Dr_{\mathrm{NN}}^3 \sum_{\mathrm{i>j}} \left(\frac{S_{\mathrm{i}}^{\hat{z}_{\mathrm{i}}} \cdot S_{\mathrm{j}}^{\hat{z}_{\mathrm{j}}}}{|r_{\mathrm{ij}}|^3} - \frac{3(S_{\mathrm{i}}^{\hat{z}_{\mathrm{i}}} \cdot r_{\mathrm{ij}})(S_{\mathrm{i}}^{\hat{z}_{\mathrm{i}}} \cdot r_{\mathrm{ij}})}{|r_{\mathrm{ij}}|^5} \right)$$

where the first term is the near-neighbour spin ice model and the other two terms represent the dipolar interaction. The coupling constant, D, is given by $D = \frac{\mu_0 \mu^2}{4\pi a_{\mathrm{p}}^3}$; the nearest-neighbour dipolar interaction and exchange interaction are given by $D_{\mathrm{NN}} = \frac{5D}{3}$ and $J_{\mathrm{NN}} = \frac{J}{3}$ respectively. Since the spins are not collinear, a factor of $\frac{1}{3}$ is introduced to the nearest-neighbour interactions [8].

2.3 X-ray diffraction

Due to the vast technological applications of thin films, more sophisticated X-ray techniques have been created to better characterise and improve our understanding of them. X-ray diffraction is particularly useful for analysing thin films because it has a penetration depth that can probe a thin film's interface(s). Thin films are normally examined from either the in-plane or the out-of-plane view; thin film layers tend to have a strong anisotropy associated with one of these views. A comparison of these perspectives will lead to a better insight into how thin film properties deviate from their bulk.

There are a number of key components and functions of the Rigaku Smartlab. The X-ray source is comprised of a cathode and a copper anode which are both sealed inside a tube. An electric potential (or tube voltage) is used to accelerate electrons, which are released from the cathode, towards the copper anode. The resulting X-ray spectrum is dependent on the tube voltage and the anode material (in this case copper) and is accompanied by a background of Bremstrulung radiation. A parallel beam slit is used to select vertically parallel beams by positioning it such that only X-rays that are reflected off a mirror are allowed through, resulting in a beam that has a divergence of $\sim 0.01°$. This type of optics is well suited for samples that have a strongly preferred direction, such as thin films. Horizontal divergence is limited through the use of soller slits, which consist of metal sheets that are parallel to the plane of diffraction. Soller slits can reduce the beam divergence to $\sim 5°$. To prevent the horizontal beam footprint from being larger than the sample, a length-limiting slit is used. The use of parallel beam optics necessitates the use of a Parallel Slit Analyser (PSA) and a Parallel Slit Collimator (PSC); both of these have the same construction as the soller slit, but the metal sheets are perpendicular to the plane of diffraction. The PSA and PSC are responsible for setting the resolution of the measurement. The receiving slits, which impact the resolution of the measurement, need to be set to their smallest slit size (0.03 mm) in order to maximise the resolution. Positioned on the incident beam side is a Ge monochromator, which consists of blocks of crystals cut such that the incident X-ray beams are reflected twice inside each block. When X-ray beams diffract off the same set of lattice planes, they become highly parallel and monochromatic. Ge can form very pure crystals, which makes it an ideal material for monochromators. A 1D detector, consisting of narrowly spaced strips of detecting elements, was used throughout all of the XRD measurements. This type of detector measures the intensity on each strip and so has positional sensitivity.

2.3.1 Understanding crystal structures

The international table for crystallography uses the Hermann-Mauguin notation, which will be used and explained in this thesis. In particular, the space groups $Fd\bar{3}m$ and $Fm\bar{3}m$ are of interest; these represent the pyrochlore and fluorite crystals. There are 7 different crystal systems, which are: triclinic, monoclinic, orthorhombic, tetragonal, trigonal/hexagonal, rhombohedral and cubic.

The symmetry of a unit cell is described by symmetry operations, which are transformations of the unit cell, that return the original unit cell. These operations can take the form of a rotation, reflection or an improper rotation, a rotation followed by an inversion, also known as a rotoinversion. Hermann-Mauguin notation describes a proper axis by assigning a number. This represents the number of times the original unit cell is returned throughout a full 360° rotation. An example of this is an equilateral triangle, which has 3-fold symmetry. The original triangle is returned three times after rotations of 120°, 240° and 360°. A bar over a number represents an improper rotation. There are a couple of special improper rotations, the first being $\bar{1}$ because it represents a rotation of 360° and an inversion. Since 360° is equivalent to a 0° rotation, $\bar{1}$ is the equivalent of an inversion. An inversion point is the point from which the inversion operation takes place. For instance:

$$Inversion\ point = \begin{bmatrix} 0 \\ 0 \\ 0 \end{bmatrix} \tag{2.1}$$

$$Crystal\ point = \begin{bmatrix} x \\ y \\ z \end{bmatrix} \tag{2.2}$$

$$Crystal\ point\ post\ inversion = \begin{bmatrix} -x \\ -y \\ -z \end{bmatrix} \tag{2.3}$$

The other special rotoinversion is $\bar{2}$, which is denoted m, because it is equivalent to a reflection from a mirror. An example of m acting on an equilateral triangular prism is displayed in Figure 2.1.

There are a number of characteristic symmetry operations, which can identify a crystal structure's symmetry. There are 32 allowed combinations of

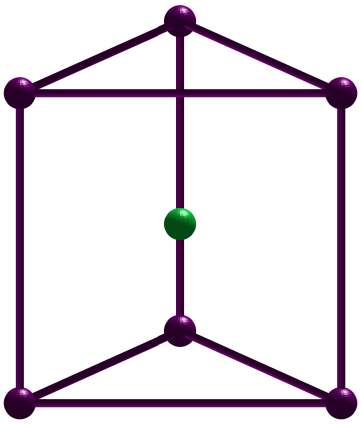

(a) Starting position of a triangular prism.

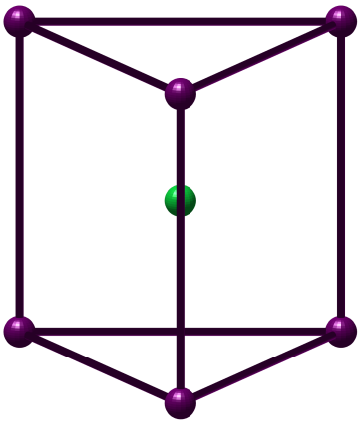

(b) The starting position has been rotated by 180°.

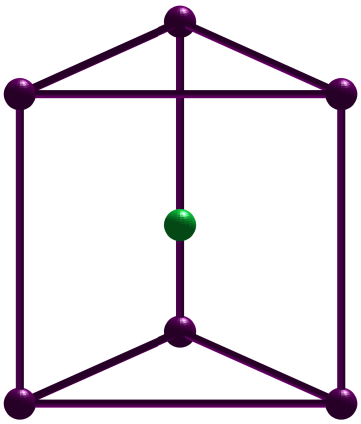

(c) The rotated triangular prism is returned to its original starting position by an inversion around the central green point.

Figure 2.1: The steps for a $\bar{2}$ rotoinversion on a triangular prism, where the purple and green points represent the lattice and inversion points respectively.

proper and rotoinversion axes, which are called point groups or crystal classes. These axes are limited to order 1, 2, 3, 4 and 6. The Hermann-Mauguin notation uses a maximum of three symbols to describe a point group's characteristic symmetry. In the case of a cubic system, the first symbol describes the symmetry of the x, y and z axes. The second symbol is always 3 or $\bar{3}$, which refers to the four body diagonals of a cube; these are shown in Figure 2.2 below. The third symbol describes the plane diagonals between axial directions. There are two rules that a point group must follow: any combination of two symmetry transformations is equivalent to an existing symmetry transformation and every axis of rotation must go through the centre of the unit cell. The last requirement results in a point which never moves. It is from this that point groups get their name.

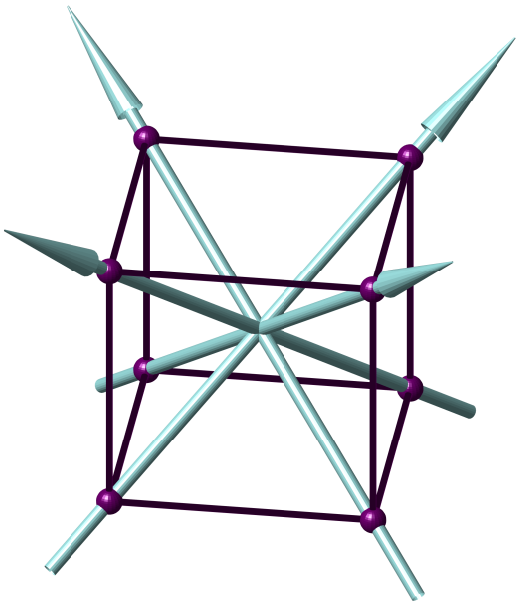

Figure 2.2: The four threefold rotation axes, light blue arrows, that are characteristic of cubic symmetry.

Crystals are comprised of repeating structures called unit cells. In general, unit cells are chosen to be small, simple and with the highest possible symmetry; these properties are listed with increasing priority. Unit cells can be translated by an integer number of its edges and can be expressed using vectors, which represent the unit cell's edges. For example a shift is given by $n_1a + n_2b + n_3c$; where n_1, n_2 and n_3 are integers and a, b and c are vectors describing the unit cell's edges. Nodes or lattice points can be generated using this shift equation. A lattice, the sum of all lattice points, is an abstract way of viewing the crystal's interior. In the simplest case lattice points have only integral coordinates, situated on the corners of unit cells. Depending on the crystal's complexity, a larger unit cell may be necessary to truly reflect its interior because they contain more lattice points. The different types of unit cell centering in the Bravais lattices are broken down in Table 2.1.

Point groups describe the characteristic symmetries of finite objects. Crystals can be thought of as infinite objects or periodic crystal lattices. Space groups describe periodic crystals in a similar way to the way in which point groups describe finite objects; they get their name for the exact opposite reason point groups get theirs. Point groups have an invariant point, but space groups do not; their name implies a lack of such a point. There are 230 different space groups. The notation that describes them can be broken into two parts: the crystal's Bravais lattice and its point group.

Unit cell type	Additional node coordinates	Total nodes	Symbol
Primitive	N/A	1	P
Body centered	$\left(\frac{1}{2}, \frac{1}{2}, \frac{1}{2}\right)$	2	I
Opposite faces	$\left(\frac{1}{2}, \frac{1}{2}, 0\right)$	2	C
Face-centered	$\left(\frac{1}{2}, \frac{1}{2}, 0\right)$, $\left(\frac{1}{2}, 0, \frac{1}{2}\right)$, $\left(0, \frac{1}{2}, \frac{1}{2}\right)$	4	F
Rhombohedral	N/A	1	R
Rhombohedral (hexagonal axes)	$\left(\frac{2}{3}, \frac{1}{3}, \frac{1}{3}\right)$, $\left(\frac{1}{3}, \frac{2}{3}, \frac{2}{3}\right)$	3	R

Table 2.1: The unit cell centering in the different Bravais lattices and their properties.

Additional symmetry operations

More complex symmetry operations are used to describe increasingly more elaborate crystals. An example of this is the glide plane operation, which is labelled with a letter a, b or c, which indicates that the glide plane is perpendicular to y or z, x or z and x or y respectively. They consist of a translation, parallel to the mirror plane, followed by a mirror reflection. The translation is given by half its lattice translation such that it is represented in the notation, where a glide plane with a translation of $a/2$ is denoted a instead of $a/2$. Figure 2.3 visually breaks down the individual components of a glide plane. A special variation of this symmetry operation is the double glide plane, which consists of two separate glide plane operations performed one after the other. The glide planes use the same mirror plane, but have perpendicular translations. The second operation also acts on the image created by the first glide plane operation, resulting in four objects. This special case is denoted e.

Glide plane operations can be carried out along diagonal directions. If the translational component of the glide plane is half of the diagonal lattice translation then it is denoted n. This notation can represent three different glide planes: $(b + c)/2$, $(a + c)/2$ or $(a + b)/2$; all of which are perpendicular to one axis. A special group of diagonal glide planes are given by d; due to their presence in diamonds, they are sometimes referred to as diamond planes. These glide planes have a translation that is 1/4 of the diagonal lattice translation and can be explicitly expressed as: $(b \pm c)/4$, $(a \pm c)/4$ or $(a \pm b)/4$. The mirror plane is parallel to all of these translations. For example, if the d glide plane is described by $(b \pm c)/4$ then its mirror plane will be in the bc plane. Figure 2.4 breaks down the different stages in a diamond glide plane. Repetition of glide plane operations will generate a point in the next unit cell, which is in the same relative position as the original point.

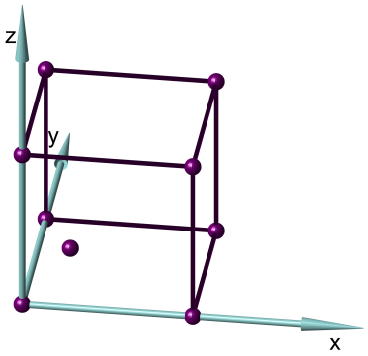

(a) A cube with an additional point located at $\left(\frac{a}{4}, \frac{b}{4}, \frac{c}{4}\right)$, where a, b and c are the lattice edges ($a = b = c$).

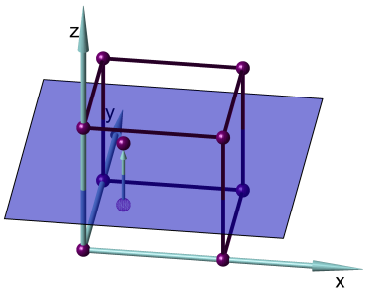

(b) A mirror reflection in the xy plane creates an image of the point at $\left(\frac{a}{4}, \frac{b}{4}, \frac{3c}{4}\right)$. This image does not relate to any point in the crystal because there is another step to the glide operation.

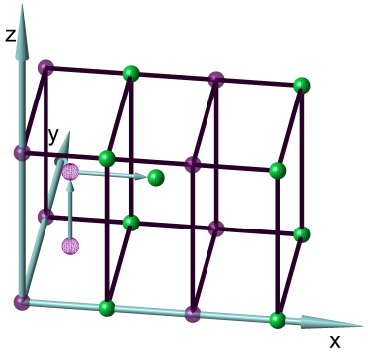

(c) All lattice points undergo a lattice translation along the x direction.

Figure 2.3: The different steps involved in a glide plane operation, where the purple, green and hollow points represent the lattice points, the new position of the lattice points and the previous positions of the inner lattice points as they were transformed. The original outer lattice points in (c) were made transparent to emphasise the translation of the inner points.

Another symmetry operation that can be used to describe a crystal's symmetry is the screw axis, which combines a rotation and a lattice translation along the axis of rotation. The notation for a screw axis is given by two numbers N and n in the form of N_n. N represents the axis order (the number of rotations required to rotate 360°). The number n is given by the inequality $1 \leq n < N$. The screw axis operation is given by a rotation of $\frac{360°}{N}$ followed by a translation along the rotation axis given by $\frac{n}{N}$ lattice vectors. Figure 2.5 displays these steps. Depending on the size of $\frac{n}{N}$ the screw axis is said to be either left or right-handed. If $\frac{n}{N} < 0.5$ the screw axis is said to be right-handed and if $\frac{n}{N} > 0.5$ the screw axis is left-handed. If $\frac{n}{N} = 0.5$ the axis is neutral.

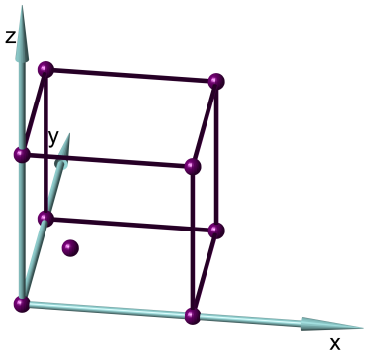

(a) A cube with an additional point given by $\left(\frac{a}{4}, \frac{b}{4}, \frac{c}{4}\right)$, where a, b and c are the lattice edges ($a = b = c$).

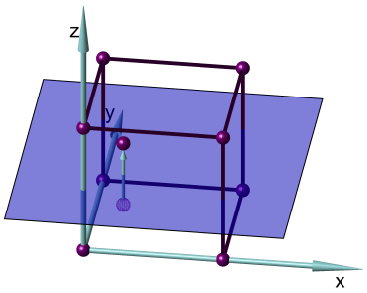

(b) A mirror reflection in the xy plane creates an image of the point at $\left(\frac{a}{4}, \frac{b}{4}, \frac{3c}{4}\right)$. This image does not relate to any point in the crystal because the glide operation has another step.

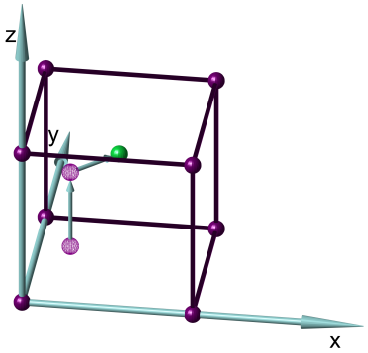

(c) All lattice points undergo a lattice translation in the xy direction given by $\left(\frac{a}{4}, \frac{b}{4}, 0\right)$.

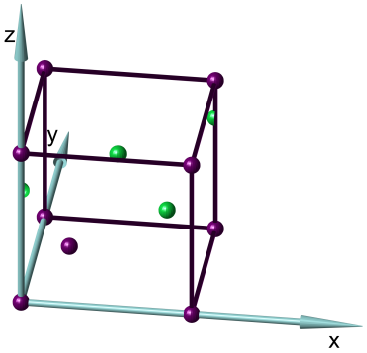

(d) The generated (green) points from repeated diamond glide plane operations on the inner (purple) point.

Figure 2.4: The different steps involved in a diamond glide plane operation, where the purple, green and hollow points represent the lattice points, the final position of the lattice points and the previous positions of the inner lattice points as they are transformed. All lattice points are shifted in (c), but only the inner points are shown to be shifted. (d) shows the inner generated points from repeated diamond plane operations.

Another method for identifying if a screw axis is left- or right-handed is to imagine walking up a spiral staircase. If your right hand is on the outer railing of the staircase then the screw axis is right-handed and vice versa.

Special and general positions are used when describing a point's position in a crystal. Crystal structures are given by specifying the symmetry operations required to produce all the points from a given initial set of points. If an initial point is positioned such that it remains stationary after a symmetry operation is performed, it is referred to as 'special'. Special positions reduce the number of points produced by symmetry operations because normally symmetry operations create replicas of the initial point. For instance Figure

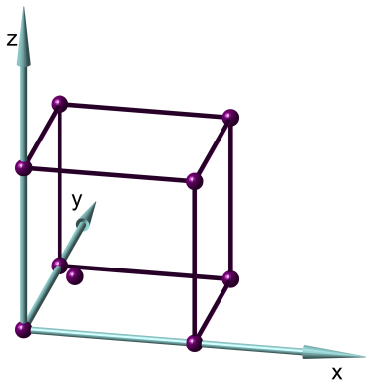

(a) A cube with an additional point given by $\left(\frac{a}{4}, \frac{b}{4}, \frac{c}{4}\right)$, where a, b and c are the lattice edges ($a = b = c$).

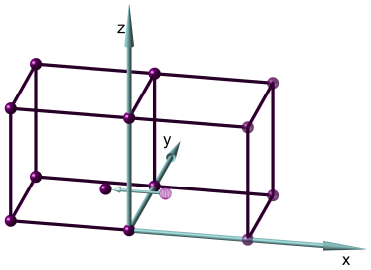

(b) The screw axis rotation is clockwise so the lattice points are rotated clockwise around the z axis by 90°. The inner point has an image at $\left(\frac{-a}{4}, \frac{b}{4}, \frac{c}{4}\right)$.

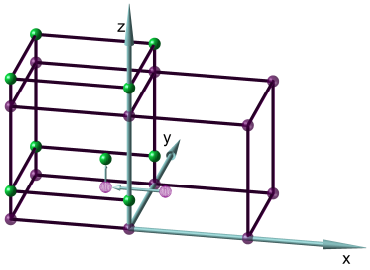

(c) The rotated points are shifted along the screw axis by $\left(0, 0, \frac{c}{4}\right)$. The inner point's final position is $\left(\frac{-a}{4}, \frac{b}{4}, \frac{3c}{4}\right)$.

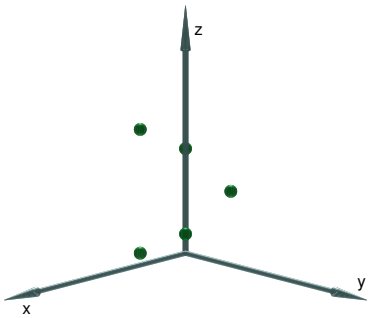

(d) The generated points from repeated 4_1 screw axis operations. It can be seen that this screw axis is right-handed.

Figure 2.5: The different steps involved in a 4_1 screw axis operation along the z axis, where the purple, green, hollow and transparent points represent the lattice points, the final position of the lattice points, the previous positions of the inner lattice point as it is transformed and the previous positions of the outer lattice points as they are transformed.

2.4 shows the diamond glide plane producing multiple points. An example of a special point would be a point positioned on an inversion point. General positions refer to positions where a number of points are produced from the symmetry operations.

Pyrochlore spin ices have the space group Fd$\bar{3}$m. Using the knowledge gained from the above explanation of Hermann-Mauguin notation and symmetry operations, the space group Fd$\bar{3}$m can be dissected. The first symbol represents the Bravais lattice and in this case the F stands for face-centered. A face-centered cubic structure is shown in Figure 2.6. It is known that this material has cubic symmetry so the second symbol d refers to a diamond glide plane, which applies to all axial directions. The third symbol is $\bar{3}$, which is

a rotoinversion with a rotation of 120° followed by an inversion. The fourth symbol m refers to a mirror reflection along the diagonals of the cube's faces.

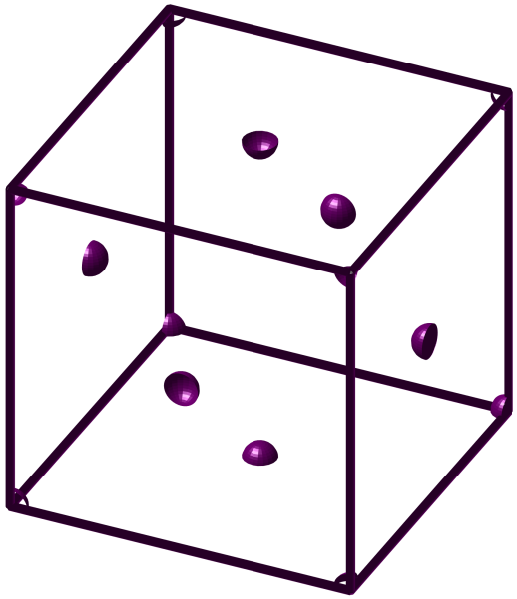

Figure 2.6: A face-centered cubic unit cell.

2.3.2 X-ray diffraction in thin films

Key equations in XRD

Some of the most important equations that describe X-ray behaviour are Snell's law and Fresnel's equations. Snell's law relates the incident angle with its reflected/refracted angle and is given by equation 2.4. Fresnal's equations relate the incident amplitude with the reflected and transmitted amplitudes, which give the reflectivity and transmittivity amplitudes shown in equations 2.5 and 2.6, respectively. All three equations are derived by assuming that the amplitude and its derivative is continuous at the interface.

$$\cos(\alpha) = n\cos(\alpha') \tag{2.4}$$

$$r = \frac{a_{\mathrm{R}}}{a_{\mathrm{I}}} = \frac{\alpha - \alpha'}{\alpha + \alpha'} \tag{2.5}$$

$$t = \frac{a_{\mathrm{T}}}{a_{\mathrm{I}}} = \frac{2\alpha}{\alpha + \alpha'} \tag{2.6}$$

Reflectivity

When an incident beam interacts with an interface, it can be reflected, refracted, absorbed or have some combination of the three. In the case of thin films the

incident beam can be refracted by the air - film interface and reflect off the film - substrate interface. This reflected beam could pass through the film - air interface or be reflected an infinite number of times between the film - air and film - substrate interface before leaving the film. After each reflection a phase shift is introduced to the beam. Since parts of the beam can reflect a different number of times from each other, there is a spectrum of phase factors in the exiting beam, which are related to the thickness of the film. The exiting beam interferes with itself, creating a series of oscillations known as Kiessig fringes. The peaks of these oscillations correspond to constructive interference in the exiting beam and the troughs correspond to destructive interference. An experimental example of reflectivity is shown in Figure 2.7. The oscillations in both the reflectivity and the specular reflection are examples of Kiessig fringes.

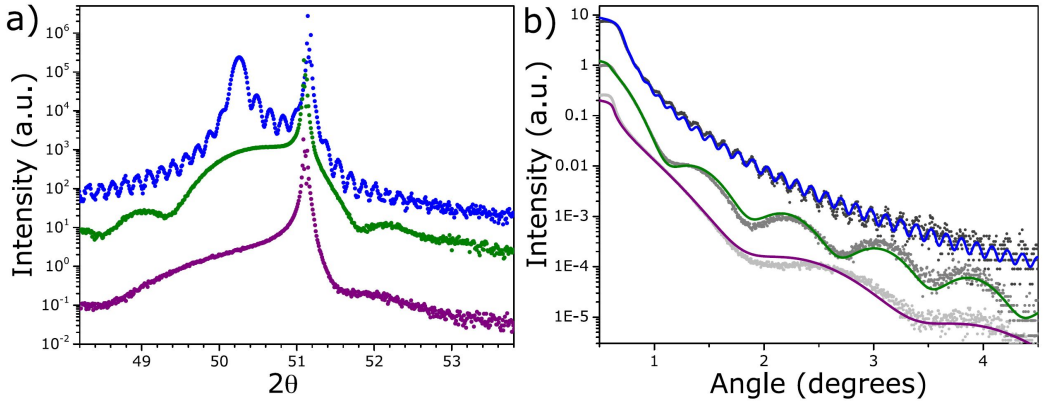

Figure 2.7: Experimental example of Keissig fringes in both specular and reflectivity data. This figure has been reproduced from [12].

2.3.3 Epitaxial strain in thin films

Oxygen deficiencies in epitaxially grown thin films can lead to an increased electrical conductivity; dislocations can suppress the electrical conductivity [11]. Tuning properties of materials via the use of strain is called strain engineering. In thin films strain is biaxial, which means that the strain is applied equally along two in-plane directions and the third out-of-plane direction is allowed to change itself. Since a perfect crystal structure represents the lowest energy configuration of a crystal, a defect in the crystal structure comes at an energy cost. Assuming a film grows layer-by-layer, the strain increases with every new layer. There is a thickness, h_C, that represents the point where it becomes energetically favourable for the crystal to introduce some form of defect. Strain

along the in-plane directions of thin films is given by equation 2.7:

$$\epsilon = \frac{(a - a_0)}{a_0} \tag{2.7}$$

where a is the in-plane lattice constant of the thin film and a_0 is the bulk lattice constant of the thin film. The out-of-plane strain can be calculated by replacing the in-plane lattice constant with the out-of-plane lattice constant. Negative values indicate compressive strain and positive values indicate tensile strain. The amount of force required to produce a given strain is called stress and is given by equation 2.8:

$$\sigma = \epsilon E \tag{2.8}$$

where E is the elastic modulus.

2.3.4 XRD geometry

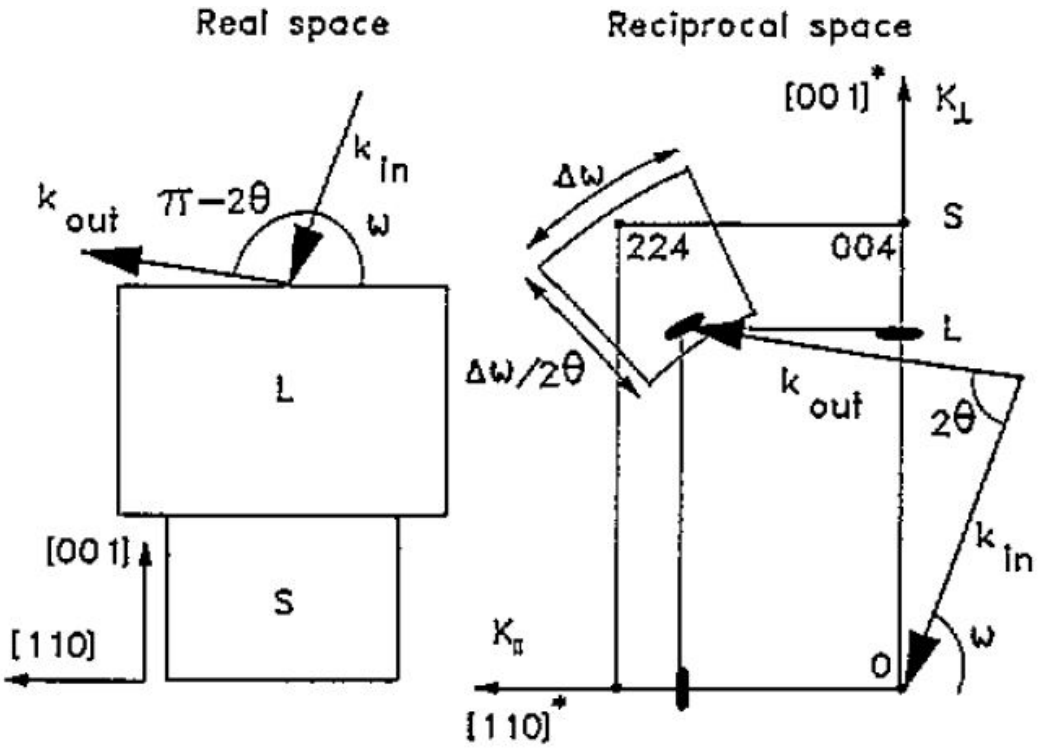

Figure 2.8: Real (left) and reciprocal space (right) representations of a diffraction experiment on a substrate (S) with a film layer (L). The film's out-of-plane direction is [001] and its in-plane direction is [110]. This figure has been reproduced from [13].

Figure 2.8 presents the views of an incoming beam on a relaxed film and the beam's geometry in reciprocal space. Using Sluis's geometry, the diffractometer's angles for a given reflection can be calculated by defining k_{in}

to have positive components in both the [001] and [110] directions and that $k = k_{\text{in}} - k_{\text{out}}$.

$$k_{\parallel} = k_{\parallel_{\text{in}}} - k_{\parallel_{\text{out}}}$$

$$k_{\perp} = k_{\perp_{\text{in}}} - k_{\perp_{\text{out}}}$$

$$k_{\parallel_{\text{in}}} = k_{\parallel_{\text{in}}} \cos(\omega)$$

$$k_{\parallel_{\text{out}}} = k_{\parallel_{\text{out}}} \cos(2\theta - \omega)$$

$$k_{\perp_{\text{in}}} = k_{\perp_{\text{in}}} \sin(\omega)$$

$$k_{\perp_{\text{out}}} = -k_{\perp_{\text{out}}} \sin(2\theta - \omega)$$

$$k_{\parallel} = k_{\text{in}} \cos(\omega) - k_{\text{out}} \cos(2\theta - \omega)$$

$$k_{\perp} = k_{\text{in}} \sin(\omega) + k_{\text{out}} \sin(2\theta - \omega)$$

$$k = k_{\text{in}} = k_{\text{out}} = \frac{2\pi}{\lambda}$$

$$k_{\parallel} = \frac{2\pi}{\lambda} (\cos(\omega) - \cos(2\theta - \omega))$$

$$k_{\perp} = \frac{2\pi}{\lambda} (\sin(\omega) + \sin(2\theta - \omega))$$

The equations in Sluis's paper are obtained by defining k_{out} as having positive components along both the [001] and [110] directions and that $k = k_{\text{out}} - k_{\text{in}}$. The difference between these two results is a minus sign in the $k_{\parallel}$ equation.

2.3.5 Experimental considerations

2.3.6 Miscuts

There are a number of experimental considerations, when performing X-ray diffraction on thin films. Miscuts are one factor that must be accounted for. These arise when substrates are cut at an angle to the desired crystal plane. This issue does not apply to bulk materials because its effect on the intensity is drowned out by the significantly larger bulk signal. Due to the much smaller size of the thin films, a miscut can have a significant contribution to the

intensity. A graphical example of a miscut is displayed in Figure 2.9. Different measurements require the incident X-rays to be aligned to a different part of the sample: reflectivity measurements require the X-rays to be aligned to the sample's surface, while diffraction measurements require the X-rays to be aligned to the sample's crystal structure.

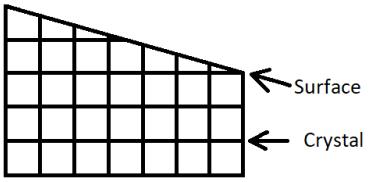

Figure 2.9: A graphical depiction of a crystal that has been miscut, where each square represents a unit cell.

Miscuts can arise along any of the sample's crystal directions, both out-of-plane and in-plane. In-plane miscuts create an offset in the sample rotation parameter ϕ. An out-of-plane miscut results in a wedge-shaped sample, which complicates the experimental system in a more discrete way. During specular scans, both ω and θ should be equal to each other, provided the sample is correctly aligned. This is true, even through a ϕ rotation. If the sample is wedge-shaped, a rotation in ϕ will cause its Bragg peak intensity to drop because as it rotates the angle of the incident beam and the sample surface changes, which introduces an ω offset. This issue is not exclusive to samples with miscuts. The same effect occurs when a sample is stuck at an angle to its sample platform. The equipment has a sample alignment procedure, which accounts for these ω offsets, but it must be repeated every time ϕ is changed. It is for this reason that the Reciprocal Space Map's (RSM's) ϕ is set before accounting for this offset.

2.3.7 Low and high angle geometries

Another experimental factor to consider is the X-ray beam's divergent nature and how this negatively affects the scan's resolution. This effect can be reduced by aligning ϕ to an off-specular peak with $\chi \neq 0$ instead of a peak with $\chi = 0$. There are fewer reflection conditions surrounding off-specular peaks with a finite χ. The more isolated the reflection condition is, the more precisely the beam can be aligned, which improves the scan's resolution. This is because divergent elements of the beam will meet fewer neighbouring reflection conditions. An example of the improved resolution and intensity is displayed in Figure 2.10. It is clear that the $\chi \neq 0$ has a sharper substrate peak and a slightly higher intensity than the $\chi = 0$ scan.

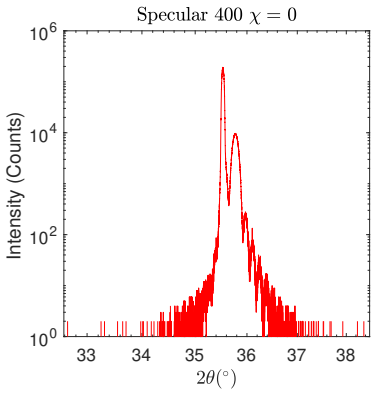

(a) Aligned with an off-specular peak, with a $\chi = 0$ value.

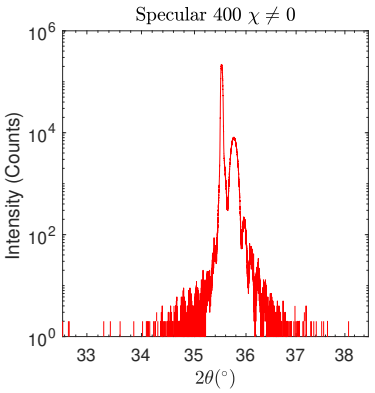

(b) Aligned with an off-specular peak, with a $\chi \neq 0$ value.

Figure 2.10: The difference in resolution between 400 specular reflections of sample 30:Yb68nm(100) when different alignments are used for ϕ. (a) ϕ was aligned using an off-specular peak with a $\chi = 0$ value. (b) ϕ was aligned using an off-specular peak with a $\chi \neq 0$ value. The Keissig fringes in (b) are slightly more pronounced, particularly on its left-hand side.

The geometry of the incident and exiting X-ray beams has a significant impact on the appearance of RSMs. The two types of beam geometry, low-incident and low-exit angle, use different ω values, where the former has a small ω value and the latter has a large ω value. A low-incident angle creates a larger beam footprint on a sample, making this type of geometry particularly good at measuring weak signals, hence it is often used to measure thin films. The downside to this technique is a loss in the scan's resolution because the exit beam is particularly long. If the low-incident angle is extreme then streaks are created in RSMs. An example of this is displayed in Figure 2.11. The low-exit angle scans do not suffer from this downside because the incident beam has a small footprint on the sample, so the exiting x-ray beam is significantly more narrow. A low-exit scan is preferable to a low-incident scan because the main objective of the RSM scans in this study was to confirm if the films were fully strained, meaning scans with a higher spacial resolution are preferable.

To switch between different geometries, the ω angle must be changed using the equation 2.9:

$$\omega_{\text{high/low}} = \theta \pm \Delta\omega \tag{2.9}$$

where $\omega_{\text{high/low}}$ is the other geometry's ω value and $\Delta\omega$ represents the difference between θ and the known peak's ω value, regardless of the current geometry.

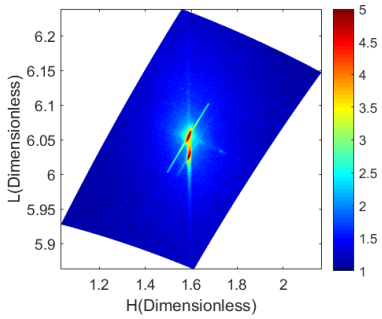

Figure 2.11: A RSM that was measured with a low-incident geometry setup, resulting in the film and substrate peaks becoming streaks.

2.4 Specific heat

2.4.1 PPMS

A Quantum Design Physical Properties Measurement System (PPMS) with its ^{3}He option was used to measure the heat capacity of the thin films. A schematic of the PPMS is displayed in Figure 2.12. The PPMS has an onion-like structure consisting of, from outermost to innermost, a super insulating layer, a liquid nitrogen layer, an evacuated layer and a liquid helium dewar. At the centre of the PPMS, there is a hole where the ^{3}He probe can be inserted. The probe also consists of multiple layers. From outermost to innermost, there is an evacuated layer, super insulation and a cooling annulus. At the centre of the probe there is a sample chamber. The liquid nitrogen layers are used to reduce the amount of liquid helium needed to cool the sample chamber. The evacuated layers are used to insulate the liquid helium bath from the sample chamber and to separate the liquid nitrogen and liquid helium baths. The cooling annulus is the region between the innermost vacuum and the sample chamber and exists to provide uniform cooling to the sample chamber when helium is pulled through the impedance assembly, which is located at the bottom of the probe. The impedance assembly is a tube, which when heated prevents the flow of helium from the dewar into the cooling annulus by forming a bubble that blocks it [14].

The heat capacity measurement involves the PPMS supplying a known amount of heat at a constant rate to the sample over a fixed time and allowing the sample to cool for the same duration of time. It is the change in temperature over both the heating and cooling phases that is measured. Small wires are used as the platform's structural support, thermal connection and its connection to both the platform heater and thermometer. A pump is used to control the pressure of the sample chamber so that the conductance of the wires is the dominant variable in the thermal conductance between the sample platform and the puck. Throughout the whole of the measurement, the PPMS pressure

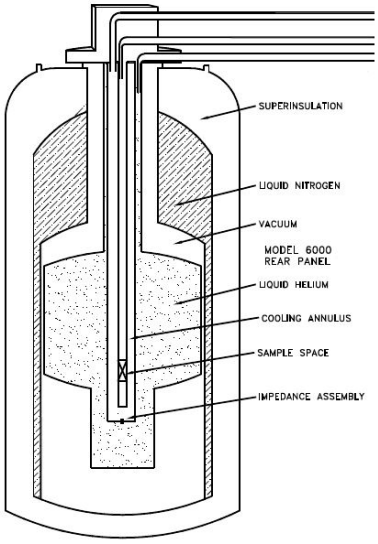

Figure 2.12: Schematic outlining the onion-like structure of the PPMS equipment that was used. This figure has been reproduced from [14].

remains constant, C_{P}. At ≈ 1 mTorr alternative thermal links through residual gas are eliminated. This heat link to the puck is reproducible and large enough such that thermal equilibrium between the platform and sample can be obtained during measurements, provided the time constant is large enough [15].

PPMS programmed analysis

The PPMS is designed to measure the heat capacity of samples that weigh between 1 - 500 mg. Its accuracy drops from 3 % to 5 % when measuring a sample between 88 mg to 4.5 mg at a temperature below 4 K. The thin films' masses are significantly lower than 4.5 mg, and so it is logical to have concerns over the accuracy of the measurements. While the mass of the thin films is low, their magnetic entropy is so large that the films' entropy is comparable with their much larger substrates. This particularly large signal eliminates concerns over a decrease in the accuracy of the measurements arising from the mass [4] (supplementary).

The idealised equation for relaxation calorimetry is given by equation 2.10:

$$Alc\frac{dT}{dt} = K\Delta T \tag{2.10}$$

where A is the film area, c is the specific heat per unit volume, l is the film thickness, K is the thermal conductivity per unit length of the 'weak link' (mechanical connection between the platform and the bath, and the sample and platform), $\frac{dT}{dt}$ is the rate of change of temperature and ΔT is the temperature difference between the thermal bath and the film. The effect of this equation

can be seen when comparing the raw calorimetry data of a film and the bulk; the former relaxing faster than the later. With most films, all the values in equation 2.10 are pretty consistent apart from l and $\frac{dT}{dt}$. These values are inversely proportional and so a smaller volume causes there to be a faster change in temperature (relaxation).

A couple of tests of the analytical software of the PPMS have been carried out by a Prof. S. T. Bramwell and Dr. L. Bovo. The PPMS uses numerical integration of the equations 2.11 and 2.12 to experimentally determine the sample heat capacity, sample temperature and the conductance of the sample platform link.

$$P = C_{\mathrm{a}}\frac{dT_{\mathrm{P}}}{dt} + K_2(T_{\mathrm{P}} - T_{\mathrm{x}}) + K_1(T_{\mathrm{P}} - T_0) \tag{2.11}$$

$$0 = C_{\mathrm{x}}\frac{dT_{\mathrm{x}}}{dt} + K_2(T_{\mathrm{x}} - T_{\mathrm{P}}) \tag{2.12}$$

Where T_{x}, C_{x} and K_2 are the values to be experimentally determined, respectively. The sample, platform and bath temperatures are given by T_{P}, T_{x} and T_0, respectively. The constants that are known are C_{a}, P and K_1 represent the addenda heat capacity, the delivered power and the conductance of the bath to the platform link respectively. In the event that $K_2 \gg K_1$ then to a good approximation $T_{\mathrm{x}} = T_{\mathrm{P}}$, which allows equations 2.11 and 2.12 to be simplified to give equation 2.13:

$$P = (C_{\mathrm{a}} + C_{\mathrm{x}})\frac{dT_{\mathrm{P}}}{dt} + K_1(T_{\mathrm{P}} - T_0) \tag{2.13}$$

The PPMS's analytical software uses time constants, which describe the thermal coupling between the bath and the platform and the platform and the sample. These are denoted τ_1 and τ_2, respectively. When equation 2.13 is used, only τ_1 is required. There are a number of instances when it is necessary to use τ_2 and equations 2.11 and 2.12, if $\frac{K_2}{K_1}$ is too small or the sample heat capacity is strongly temperature-dependent. In the case of the thin films, the simplified equation is mainly used because its relatively large surface area to mass ensures that it will have a large thermal conductance, K_2. It is thought that the samples themselves have a slow relaxation time, which is the cause of needing to use the full set of equations for some measurements.

Schottky anomaly

A specific heat capacity feature which is present in both bulk and thin film spin ice is the Schottky anomaly. When the temperature is raised, the excited

energy levels' states become accessible, producing a broad peak in the specific heat. This feature arises most commonly at very low temperatures. A two-level system has a Schottky anomaly given by the equation 2.14, where Δ is the energy difference between the ground state and the excited state.

$$C_{\text{Schottky}} = R\left(\frac{\Delta}{T}\right)^2 \frac{e^{\frac{\Delta}{T}}}{\left(1+e^{\frac{\Delta}{T}}\right)^2} \tag{2.14}$$

2.4.2 Debye model

The Debye model aims to predict the heat capacity contribution from vibrations. The model treats vibrations as quantised particles (phonons) that are trapped inside a box. Its predictions for high and low temperatures successfully match experimental results, but fail to produce correct results in the intermediate temperature range. At the low temperature limit, the model predicts that the heat capacity has a $\approx T^3$ dependence and is given by equation 2.15:

$$C = \frac{12Nk_{\text{B}}\pi^4}{5}\left(\frac{T}{\Theta_{\text{D}}}\right)^3 \tag{2.15}$$

where N is the number of atoms in the system, T is the temperature and Θ_{D} is the Debye temperature. The Debye temperature is a constant that accounts for all the material specific contributions to the heat capacity, including the phonon heat capacity.

2.4.3 Entropy

Entropy has been defined and calculated in many different ways, but for the purposes of this thesis the equations 2.16 and 2.17 are most appropriate.

$$S = R\ln(\Omega) \tag{2.16}$$

$$S = \int \frac{c}{T} dT \tag{2.17}$$

where S is the entropy, R is the ideal gas constant, Ω is the number of accessible microstates, c is the specific heat and T temperature. Equation 2.16 expresses entropy in the form which is quoted throughout this thesis as it relates entropy to the system's available microstates and thus has the greatest physical relevance in the context of spin ice and its related materials. Equation 2.17 explains that the entropy of a sample is given by the area under the specific heat divided by the temperature curve.

2.5 Magnetometry

2.5.1 SQUID

The key component to understanding how a SQUID system works is the Josephson junction, which consists of two superconductors that sandwich an insulator. The superconductor wavefunction is given by equation 2.18:

$$\Psi(\overrightarrow{r}) = \sqrt{n_s} e^{i\phi(\overrightarrow{r})} \tag{2.18}$$

where the Cooper pair density is given by $n_s = \Psi \cdot \Psi^*$ and $\phi(\overrightarrow{r})$ is the phase of the electrons in the superconductor. Cooper pairs are formed when pockets of positively charged ions are close enough to form a dense positive charge, which causes the electron - electron repulsion to be overcome, resulting in electron pairs forming. These pairs behave as bosons, meaning the Pauli exclusion principle does not apply to them. This allows all of the electron pairs to occupy the same lowest energy state. This is what allows superconducting currents. These pairs can be formed over a distance of 100s nm. In the case of the Josephson junction, provided the insulator that is being sandwiched is sufficiently thin, Cooper pairs can be formed such that the paired electrons are in separate superconductors. The Josephson equations describe how the tunnelling current changes with phase difference and how the phase difference changes with time. When measuring a sample, it is moved back and forth inside of pick-up coils, which generates a relative voltage and sample position. This voltage is transformed so that the signal is not too large to interact with the Josephson junctions. This is a necessary step because the Josephson junctions are so sensitive that they have to be isolated from the sample inside of the SQUID. The outputted voltage from the Josephson junctions is used in an algorithm to calculate the sample's magnetic flux [16, 17]. An account of how the first SQUID device was made and used is given in [18].

2.5.2 Magnetometry experimental features

The M vs H measurements will be described in greater detail later in this thesis, but for now some of its experimental features will be discussed. First of all, the sample's magnetic moment can be determined through M vs H measurements, but the measured values can change based on the sample orientation; this applied to both bulk and thin films of $Dy_2Ti_2O_7$ [4]. In M vs H measurements there can be a jump in the magnetisation, which is indicative of sample impurities or another magnetic phase.

Element	Atomic number	Ion	Coordination number Å			
			6	7	8	9
Lanthanum	57	La^{3+}	1.03	1.10	1.16	1.22
Cerium	58	Ce^{3+}	1.01	1.07	1.14	1.20
Praseodymium	59	Pr^{3+}	0.99	-	1.13	1.18
Calcium	20	Ca^{2+}	1	1.06	1.12	1.18
Neodymium	60	Nd^{3+}	0.98	-	1.11	1.16
Samarium	62	Sm^{3+}	0.96	1.02	1.08	1.13
Europium	63	Eu^{3+}	0.95	1.01	1.07	1.12
Gadolinium	64	Gd^{3+}	0.94	1.00	1.05	1.11
Terbium	65	Tb^{3+}	0.92	0.98	1.04	1.10
Dysprosium	66	Dy^{3+}	0.91	0.97	1.03	1.08
Yttrium	39	Y^{3+}	0.90	0.96	1.02	1.08
Holmium	67	Ho^{3+}	0.90	-	1.02	1.07
Erbium	68	Er^{3+}	0.89	0.95	1	1.06
Thulium	69	Tm^{3+}	0.88	-	0.99	1.05
Ytterbium	70	Yb^{3+}	0.87	0.93	0.99	1.04
Lutetium	71	Lu^{3+}	0.86	-	0.98	1.03
Magnesium	12	Mg^{2+}	0.72	-	0.89	-

Table 2.2: The effective ionic radii for the lanthanide $^{3+}$ ions. This table has been recreated from [20].

For χ vs T measurements there are two features which suggest the presence of ferromagnetic impurities. The first is a splitting of Field-Cooled (FC) and Zero-Field-Cooled (ZFC) measurements. Ferromagnetic materials are history-dependent, and so the two different experimental procedures of FC and ZFC produce different sized magnetic moments in the impurities, causing the FC and ZFC results to split apart. Ferromagnetism has the strongest coupling between magnetic moments so more energy is required to destroy this magnetic phase. As a result, a large magnetic moment seen at a high temperature is likely to be ferromagnetic in nature.

2.5.3 Single ion properties

The effective magnetic moments of Tb^{3+}, Dy^{3+} and Yb^{3+} when in compounds, range from 9.5 - 9.8 μ_B, 10.4 - 10.6 μ_B and 4.3 - 4.9 μ_B respectively. Their free ion states are as follows: $^7F_6$, $^6G_{\frac{15}{2}}$ and $^2F_{\frac{7}{2}}$ respectively [19].

Table 2.2 displays the effective ionic radii of the $^{3+}$ lanthanide ions [20]. As the lanthanide's atomic number increases its ionic radius decreases. Of the lanthanides used in this thesis terbium has the largest ionic radius of 0.92 Å, followed by dysprosium with 0.91 Å and lastly ytterbium with 0.87 Å (using coordination number 6). Dysprosium has the closest ionic radius to yttrium (0.90 Å), which could assist in $Dy_2Ti_2O_7$ growing more successfully on $Y_2Ti_2O_7$.

Chapter 3

Literature Review

3.1 Spin ice systems and models

Before the first paper on spin ice in 1997 by Harris *et al.* [5], no one thought that a ferromagnet could display geometrical frustration. This paper revealed that a ferromagnetic pyrochlore with local Ising anisotropy could be mapped onto the ice model, giving birth to the "spin ice model". The first known material to exhibit spin ice behaviour was $Ho_2Ti_2O_7$. Neutron scattering experiments were performed on it, revealing two possible ordered magnetic phases in an applied field. The most dominant phase displayed ferromagnetic behaviour, $q = 0$. The other phase displayed anti-ferromagnetic behaviour, $q = X$, and only became significant in the temperature range 0.8 - 2 K. For both phases only half of their spins align with the magnetic field. The $q = 0$ magnetic phase's other half of spins point 45° away from the applied field. The $q = X$ magnetic phase's other half of spins point in alternating anti-ferromagnetic chains of spins that are transverse to the applied magnetic field. These magnetic phases arise from frustration between single-ion anisotropy and ferromagnetic coupling. This frustration is also partly responsible for the spin-freezing process.

Bramwell and Harris [21] report on the key discoveries in the field of spin ice. They address the initial interest in pyrochlores and the significance of their $Ho_2Ti_2O_7$ results. The theoretical spin ice models, the nearest-neighbour spin ice model and the DSIM, are described along with how they compare to experiment. The authors discuss the exotic excitations and phase space that is accessible to this group of materials. The breadth of its phase space was realised when it was observed that the energy of different sets of spin configurations could be manipulated by using the external variables: temperature, applied field, strain, chemical substitution, etc. In addition, the authors discuss the experimental search for the quantum spin ice phase. They also delve into

the properties of magnetic monopoles, including their thermodynamics and currents. The authors conclude that the biggest insight over the last two decades of spin ice research is the applicability of simple vertex models to a diverse range of real systems, phenomena and exotic physics.

Barry *et al.* [22] reported a systematic study on $Ho_2Ti_2O_7$ thin films, which were grown on commercially available Yttria-Stabilized-Zirconia (YSZ) substrates. The paper investigates the films through a thickness and epitaxial strain series. The film out-of-plane directions studied are [111], [110] and [001]. Transmission Electron Microscopy (TEM) and X-ray Photoelectron Spectroscopy (XPS) measurements suggested that there is anti-site disorder in the films, but no stuffing. In all of the samples, there was a portion of it at the film-substrate interface that had relaxed. The hallmark spin ice magnetisation plateau is present in the [110] film, which has a [111] in-plane direction. The [111] and [001] film do not display the spin ice plateau. A RSM along each orientation was presented, all of which displayed signs of relaxation, with the [111] film appearing to be the most strained film. The films grown on the [111], [110] and [001] YSZ substrates had rhombohedral, orthorhombic and tetragonal structures respectively. XPS measurements showed that the films have the correct stoichiometric quantity of Ho and Ti atoms. High-Angle Annular Dark-Field Scanning Transmission Electron Microscope (HAADF-STEM) measurements revealed that there was anti-site disorder inside the films. Field-cooled neutron scattering on the [111] 400 nm film showed only the $Q = 0$ reflections, which implied that there were only parallel β chains and polarised α chains. M vs H measurements revealed that the films' magnetic moments saturated around highly polarised states. It was also noted, thinner films reached saturation faster than thicker films. Another feature that was seen across the films was their ability to saturate faster when the field was applied along one of their in-plane directions. The authors believe this may indicate shape anisotropy. The $\frac{dM}{dH}$ vs H was plotted for the films, which highlighted the [110] film's spin ice plateau state. This state has been simulated via Monte Carlo simulations of the dipolar spin ice model. The authors conclude by stating that their [110] film exhibits perturbed spin ice behaviour, which likely arises from defects and anti-site disorder and results in the suppression of the ordering temperature.

Jaubert *et al.* [23] report on surface-ordering effects in spin ice thin films. The paper focuses heavily on the effects from orphan bonds, which are bonds that lie on the surface of a thin film and so are missing a neighbouring tetrahedron. The authors treat them as a chemical potential for an ordered surface of magnetic charges, which means that after adding an amount of

additional orphan bonds (or monopoles), the authors expect, a transition to a surface-ordered state to become energetically favourable. In their modelling they used the DSI model with added perturbations that accounted for the film's strain and its orphan bonds. Monte Carlo simulations were performed on a system, which was truncated along its [001] cubic axis and was periodic along its perpendicular directions. These simulations were performed over multiple film thicknesses, 1 - 3 monolayers. When the model only included perturbations from the sample's orphan bonds, the specific heat displayed a large Shottkey anomaly that became more bulk-like the thicker the sample became implying a surface transition. By varying the strength of surface effects on orphan bonds at low temperature, the entropy could display two ordering transitions. The first represented the surface-ordering at $T \approx 900$ millikelvin; this also caused the bulk of the film to obtain square-ice ordering. At $T \approx 300$ millikelvin, dipolar interactions caused the system to order into an f-model anti-ferromagnetic phase. Due to the restrictions on which directions the orphan bonds can point in, the entropy released by the square-ice was $\frac{1}{4}\left(\frac{3}{4}\ln\left(\frac{4}{3}\right)\right)$. Taking into account only the perturbation from positive strain effects, the transition to an ordered state was smooth and occurred at a higher temperature than bulk spin ice. A negative strain produced a KDP transition to a ferromagnetic state.

Twengström *et al.* [24] have reported a systematic study on the different analytical models of spin ice and their ability to replicate the pinch-points observed in neutron scattering. The structure factor tensor can be given by two eigenvalues: the longitudinal and transverse eigenvalues. Twengström *et al.* expressed these in terms of a wavevector whose centre is at the origin of a Brilloin zone, q. They could also be visualised as an ellipsoid. If the ellipsoid was more disk-shaped, then the projection along two different axes could create an infinitely sharp point (the pinch-points). A number of different analytical models were fit to simulations. The Near Neighbour Spin Ice (NNSI) model described the simulated results incredibly well. The model was then modified through the addition of dipolar interactions without screening effects. It was hoped that this would accurately describe Dipolar Spin Ice (DSI). Even without screening there was good agreement with the simulated Spin Flip (SF) results. However, the Non-Spin Flip (NSF) results showed slightly worse agreement. The screening effect was added in by treating the dipolar integral as the sum of the thermally-generated monopoles, which partially screen each other. Complete screening was not modelled because the unscreened contribution is necessary for the infinitely sharp pinch-points and so is essential to the model. Finally, the analytical theory and simulation were compared with experiment, which revealed the pinch-point paradox. This paradox is that

the DSI model can be used to fit both experiment and simulation while using different conditions. The unscreened model fits the simulation and the screened model fits the experiment. While the simulation has a delta function, the experiment has a Lorentzian; both are considered correct, hence the paradox.

3.2 Rare-earth pyrochlores

Bramwell *et al.* [25] presents a systematic magnetic study of rare-earth titanate pyrochlores. Specifically, $Gd_2Ti_2O_7$, $Dy_2Ti_2O_7$, $Ho_2Ti_2O_7$, $Er_2Ti_2O_7$ and $Yb_2Ti_2O_7$ were investigated. These materials are known to be chemically-ordered electrical insulators. The authors used X-ray and magnetometry experiments in their characterisation. Powder diffraction was used to obtain the materials' lattice parameters. The parameters of $Dy_2Ti_2O_7$ and $Yb_2Ti_2O_7$ were 10.1171 $\mathring{A}$ and 10.024 $\mathring{A}$ respectively. The Curie-Weiss constant and magnetic moment were obtained through an inverse susceptibility plot. After subtracting the Van Vleck term, $\theta_{\mathrm{CW}} = -0.24(1)$ kelvin and $\mu = 9.615(5)\mu_{\mathrm{B}}$ for $Dy_2Ti_2O_7$. These results imply weak anti-ferromagnetism. However, when the demagnetising effect was taken into account $\theta_{\mathrm{CW}} \approx 1$ K, which implies that it is ferromagnetic. Its magnetic moment was similar to both the ground state $m_{\mathrm{J}} = \pm\frac{15}{2}$ doublet and the ground term ${}^6G_{\frac{\pm 15}{2}}$ of Dy^{3+}. The saturation moment of $Dy_2Ti_2O_7$ was half of the expected, which implies that it is anisotropic. A series of M vs T measurements were carried out from 1.8 kelvin to 20 kelvin. Several fits were made to find the effective g-factor which best described all of the measured data sets. The value chosen was $g = 18.5(1)$. This effective g is slightly off from the expected value for a pure doublet ground state and so it was thought that the ground state contained a small admixture of other terms present in the m_{J} manifold. $Yb_2Ti_2O_7$ was more complicated than $Dy_2Ti_2O_7$ because its effective magnetic moment was temperature-dependent and ranged from $\approx 4\mu_{\mathrm{B}}$ to $\approx 3mu_{\mathrm{B}}$. After a Van Vleck correction was made, the results became less temperature-dependent, with an effective magnetic moment of $\approx 3\mu_{\mathrm{B}}$. The justification for this correction was seen as dubious because the first excited state of $Yb_2Ti_2O_7$ is much closer than that of $Dy_2Ti_2O_7$ and so its temperature-dependence may arise from thermal populations. Its Curie-Weiss constant varied little between calculations with and without the Van Vleck correction: $\theta_{\mathrm{CW}} = 0.59(1)$ kelvin and $\theta_{\mathrm{CW}} = 0.49(1)$ kelvin respectively. When taking the demagnetising correction into account, the $\theta_{\mathrm{CW}} \approx 0.7$ kelvin. The authors were unable to fit a suitable g-value over all of the experimental data and so settled for the compromise result of $g = 7.2$. Due to the poor fit, they speculated that there was a perpendicular g-value.

3.3 $Dy_2Ti_2O_7$

Ramirez *et al.* [26] revealed that specific heat measurements on bulk $Dy_2Ti_2O_7$ display a residual entropy. By integrating the specific heat divided by the temperature, Ramirez showed that the total accessible spin entropy had been reduced to two thirds of its value. This reduced entropy had been predicted by extrapolating earlier data, but the authors were the first to experimentally confirm this prediction. This is because their measurements began at a lower temperature than previous studies. The authors believe that below the value their measurements began, 0.2 K, it is unlikely that the missing entropy would be recovered because the specific heat divided by the temperature dropped rapidly from 1 to 0.5 K, which implies that the spins are freezing. Also, there would need to be a bimodal distribution and there is no reason structurally why this would occur.

The first $Dy_2Ti_2O_7$ thin films were reported by Bovo *et al.* [4]. The films were grown on top of a $Y_2Ti_2O_7$ substrate because it is isostructural to $Dy_2Ti_2O_7$. The structure of the samples was characterised using XRD measurements. The films' thicknesses were determined by fitting reflectivity measurements and measuring the films' Kiessig fringes. The films were confirmed to be epitaxial via an off-specular RSM. There are three experimental signatures that spin ice exhibits outside of neutron scattering: a magnetic moment that saturates at different values along different crystal directions, its susceptibility when corrected for demagnetisation does not follow the Curie law, and its residual entropy is given by the Pauling entropy. The main focus of this study is on how their films compare with these features. The magnetometry revealed that there was good agreement with the 2-in 2-out theoretical calculations for the magnetic moment's saturation point. The samples' susceptibility results matched the bulk values at higher temperatures, but at lower temperatures there was a significant departure from the bulk. The magnetic entropy, obtained through heat capacity measurements, revealed that the films were similar to bulk $Dy_2Ti_2O_7$ down to $\approx$ 2 K. Beyond this point the films and the bulk measurements deviated as the films lost all of their entropy by $\approx$ 0.3 K. This result was confirmed again via magnetometry. It is thought that this departure is related to the epitaxial strain breaking the spin ice state's degeneracy.

Bovo *et al.* [27] reported on the Curie law crossover, which was predicted for the spin ices $Dy_2Ti_2O_7$ and $Ho_2Ti_2O_7$. The crossover was calculated using the NNSI model with the isothermal susceptibility. It was predicted that between $\approx 4K$ and the low temperature limit the Curie constant would double, $C = 2C$. Experimental results were in agreement with this theory down to 10 K. At lower

temperatures there was still agreement with both magnetometry and neutron scattering at the Brillouin zone boundary, but the neutron scattering at the zone centre did not. This article aimed to resolve this disagreement between experimental results and theory. The earliest susceptibility measurements on bulk single crystals of spin ice were block-like in shape and were prone to more crystal defects, due to a different method of growth. These issues were thought to have introduced systematic errors into the isothermal susceptibility estimation. Bovo *et al.* used spherical crystals. Low field susceptibility measurements were carried out using both FC and ZFC procedures. The results did not show any splitting between FC and ZFC. The diamagnetic and Van Vleck contributions to the susceptibility were subtracted, leaving the Langevin contribution. This was plotted in a $\frac{\chi T}{C}$ vs T plot, which revealed a difference between experiment and theory below 10 K. The experimental Curie crossover reached a maximum of approximately $1.4C$ instead of the theoretical value of $2C$. A number of non-spherically-shaped $Dy_2Ti_2O_7$ samples were also measured. It was shown that when using the nominal value for the demagnetising factor there appeared to be agreement with the theoretical value of $2C$. When the demagnetising factors were changed such that the non-spherical results were mapped onto the spherical results, it was noted that these corrections did not correspond to either the magnetometric or ballistic demagnetising factors, but were somewhere in between. This led the authors to conclude that the sample fields were not homogeneous, $Dy_2Ti_2O_7$ exhibits shape-dependent physics or a combination of the two.

Arroo and Bramwell report on experimentally measurable features of the F-model [28]. To begin with, they walk through how to calculate the exact free energy of the F-model inside an applied field. This involves solving two functions, which represent different phases. These functions can only be solved numerically but, once completed, experimentally important equilibrium values of the polarisation, susceptibility and specific heat can be calculated. The infinite-order anti-ferromagnetic phase transition in the F-model is modified in the presence of an applied field such that it becomes a second-order transition. The authors revealed an unusual property of this second-order transition, which was that its free energy was identical to the free energy after the infinite-order transition. This was explained as a cause of the system's polarisation, arising only from system-spanning windings. When the field was varied, it was shown that the polarisation turned into a step function at zero temperature where $m = 0$ for $H < \epsilon$, $m = 1$ for $H = 2\epsilon$ and m is some intermediate value for $H = \epsilon$. The authors were able to demonstrate that topological behaviour was present in the F-model by showing the violation of Fisher's relation, which requires that

the energetic susceptibility ($\frac{\chi T}{C}$) should mimic the internal energy of the system. At the end of the paper, the F-model was compared with experimental systems. In the case of the near-neighbour spin ice model, there are excitations that obscure the F-model, but in real systems such as thin films of $Dy_2Ti_2O_7$ the high epitaxial strain shifts these excitations to a higher energy such that the F-model becomes relevant again. The authors conclude that topological effects from the F-model are likely to be found in many experimental systems.

3.4 $Yb_2Ti_2O_7$

Arpino *et al.* [29] reported a systematic study about the impact of stoichiometry on $Yb_2Ti_2O_7$. This was an area of interest because there was a lack of consistency in the literature regarding a low temperature transition to long-range order in $Yb_2Ti_2O_7$. The impact of off-stoichiometry in $Yb_2Ti_2O_7$ was tracked by doping $Yb_2Ti_2O_7$, so that its form followed $Yb_{2+x}Ti_{2-x}O_{7-\delta}$. X-ray, heat capacity and magnetometry measurements were carried out to characterise the changes in the samples. It was shown that as x increased so did the lattice parameter, which was expected because the Yb^{3+} ion is larger than the Ti^{4+} ion. The doping also produced secondary phases of TiO_2 and Yb_2TiO_5 for negative and positive x respectively. The specific heat measurements displayed a peak just under 300 millikelvin for the stoichiometric single crystal. The latent heat and sharpness of the heat capacity peak are consistent with a first-order transition. This peak decreases in temperature and broadens as the $Yb_2Ti_2O_7$ is doped further away from stoichometric $Yb_2Ti_2O_7$. It is suspected that most literature samples were doped off stoichometry by $x \approx 0.02$. The magnetic entropy of a $Yb_2Ti_2O_7$ single crystal measured up to 10 kelvin was greater than the Pauling entropy, $R\ln(2) - \left(\frac{R}{2}\right)\ln\left(\frac{3}{2}\right)$, confirming that the ground state of $Yb_2Ti_2O_7$ is not a spin ice state. The non-stoichometric $Yb_2Ti_2O_7$ samples were measured up to only 2 kelvin because up to this point they closely matched the stoichometric $Yb_2Ti_2O_7$ single crystal, which led the authors to assume that the samples would recover an entropy of $R\ln(2)\,Jk^{-1}(\text{Yb ion})^{-1}$ if they were measured to a higher temperature. The magnetic susceptibility displayed a linear relationship with temperature along the measured range, 2 kelvin to 30 kelvin. The series had a randomly distributed effective magnetic moment of around 3.171 $\mu_B(\text{Yb ion})^{-1}$. This implies that the Yb^{3+} ions, which were replaced, were replaced by Ti^{4+} ions instead of Ti^{3+} ions because the magnetisation would increase from Ti^{3+} ions. The authors also noticed that, as the Yb content was increased (stuffing), the Curie-Weiss temperature decreased.

Neutron scattering measurements on bulk $Yb_2Ti_2O_7$, at 30 millikelvin with an applied field of 2 and 5 tesla, were reported on by Ross *et al.* [30]. A spin wave model was fitted to these results with good agreement and from this the microscopic exchange constants were obtained. The largest exchange interaction came from the frustrated ferromagnetic (spin ice) component. This was surprising because $Yb_2Ti_2O_7$ has x-y spins, which means its spins' largest magnetic component is perpendicular to the local [111] direction it points in. The fitted parameters accurately reproduced the field-induced ferromagnetic state. However, at low fields the model broke down because it lacked an ordering transition or its ordering was strongly suppressed, which indicates strong fluctuations. The nature of these fluctuations could be classical, quantum or both. Two possible explanations for the lack of ordering were given, the first of these being that defects in the crystal produce nano-scale domain walls, which hinder ferromagnetic-order. The second explanation was that at low fields $Yb_2Ti_2O_7$ has a Quantum Spin Liquid (QSL) state. A zero-field Hamiltonian was cast in terms of spins along the C_3 axis, which suggested that $Yb_2Ti_2O_7$ could have a stable QSL state. This is significant because interest in $Yb_2Ti_2O_7$ stems from theoretical studies, which suggest unusual ground states in antiferromagnetic pyrochlore materials, the most desired state of these being the Quantum Spin Liquid (QSL) state. This state does not order and has dual electric monopoles, emergent photons and magnetic monopoles as possible excitations.

Chang *et al.* [31] presented a different view on bulk $Yb_2Ti_2O_7$. Through specific heat measurements and Extended X-ray Absorption Fine Structure (EXAFS) they showed that the tendency of $Yb_2Ti_2O_7$ to order at low temperature is dependent on its proportion of Yb atoms. The more deficient the sample is in Yb, the harder it is to order. The authors speculate that this is the reason why their sample was able to order ferromagnetically at low temperatures, but Ross *et al.*'s was not. Chang *et al.* proposed that there is a magnetic Coulomb liquid phase in the temperature range $T_C < T < 2J$, where 2J corresponds to the temperature required to get monopolar spinon excitations. For this phase to exist, there must be uniform proliferation of monopole charges to prevent the breaking of symmetry. Chang *et al.* also proposed that there was a Higgs transition between this magnetic coulomb liquid and the ferromagnetic phase. To identify a Higg's transition, three features are required: pinch-points, the system's spins have a finite planar component, and a magnetically-ordered low temperature phase that has gapped spin excitations. The authors present diffuse neutron scattering on the hhl plane. Pinch-points were seen in the high temperature paramagnetic phase, which became increasingly sharp as the

temperature dropped. Calculations of the hhl plane using the random phase approximation were made, which successfully reproduced the profiles of the experimental results. From this calculation, it was determined that the Ising exchange favoured the 2-in 2-out configuration. A plot presenting the sum of the SF and NSF signals through the [111] rod was presented at different temperatures. There was a drop in intensity on the 1.5 1.5 1.5 reflection at 0.2 K, which suggests a change in the spin correlations. The 111 reflection was measured with polarised neutron spins as a function of temperature. The results obtained displayed a hysteresis around T_C, which indicates a first-order phase transition. From these observations, Chang *et al.* concluded that the Higgs transition was only hinted at and that more experiments were required to confirm its existence.

A further study on the ground state of $Yb_2Ti_2O_7$ was reported by Scheie *et al.* [32]. They presented elastic neutron scattering along with theoretical simulations, which they used to deduce multiphase magnetism in the ground state of YbTO. This multiphase magnetism is thought to form through one of two different mechanisms. The first mechanism requires the ground state to consist of ferromagnetic domains with anti-ferromagnetic domain walls, which are stablised through the dipolar interaction. The second theory involves the Hamiltonian being on the phase boundary of ferromagnetism and anti-ferromagnetism, which enables dynamic fluctuations to cause anti-ferromagnetism. The authors conclude by saying that more work is required to deduce which mechanism is the cause for $Yb_2Ti_2O_7$'s multi-phase magnetism.

Blundred *et al.* [33] reported on new oxidation states in pyrochlore materials. A reduction of both $Yb_2Ti_2O_7$ and $Lu_2Ti_2O_7$ was achieved by heating the titanates with the reducing agent CaH_2. This reaction is dependent on the size of the (lanthanide) rare-earth ions in the titanates. When reduced, Sm and Eu titanates form Ti^{3+} perovskites, but titanates with a smaller lanthanide ion are able to produce reduced pyrochlore structures. The largest reduction was observed in Lu and Yb titanates, the most extreme case being in $Lu_2Ti_2O_7$. In $Ln_2Ti_2O_7$ materials, oxygen is removed from the centre of the Ti tetrahedra, which corresponds to the O sub-lattice instead of the O' sub-lattice. These sub-lattices can be represented in the rare-earth titanate empirical formula as $A_2B_2O_6O'$.

3.5 $Tb_2Ti_2O_7$

Chapuis *et al.* measured the magnetic entropy of bulk $Tb_2Ti_2O_7$ using a PPMS and a ^{3}He - ^{4}He dilution refrigerator [34]. The measurements revealed

that the total accessible entropy in $Tb_2Ti_2O_7$ up to 20 K was $R\ln(4)$. The authors reasoned that if its ground state was a doublet then the entropy should not drop below $R\ln(2)$ at low temperature. Since the entropy did drop below $R\ln(2)$, the authors concluded that the ground state was a singlet and that there was a nearby excited singlet state at $\approx$ 1.8 K.

There has been some controversy regarding the ground state energy levels of $Tb_2Ti_2O_7$ [35]. A follow-up paper by Gaulin *et al.* challenged the energy level structure that Chapuis *et al.* proposed because they had ignored important short-range correlations, which resulted in an incorrect conclusion. In this paper, inelastic neutron scattering results were presented, which did not reveal any singlet-singlet splitting. A spin-3/2 Ising model on a 1D chain with ferromagnetic nearest-neighbour exchange was used to show that the interactions in $Tb_2Ti_2O_7$ could eliminate the $R\ln(2)$ entropy plateau that Chapuis *et al.* expected for a ground state doublet.

3.6 $Y_2Ti_2O_7$

Hayward [36] studied the effects of topotactic reduction on bulk $Y_2Ti_2O_7$. Three samples of powdered $Y_2Ti_2O_7$ were mixed with powdered CaH_2 and left under vacuum at 575 °C for different lengths of time. The longer the time, the greater the sample's reduction. From X-ray powder diffraction and neutron powder diffraction measurements, it was deduced that each sample contained two reduced phases: $Y_2Ti_2O_{6.48(2)}$ and $Y_2Ti_2O_{5.90(6)}$. The bond-lengths of these two phases were analysed, which revealed that some of the oxygen from one particular site had been taken in the phase $Y_2Ti_2O_{6.48(2)}$. Besides this change, the rest of the phase remained the same as stoichometric $Y_2Ti_2O_7$. The second phase, $Y_2Ti_2O_{5.90(6)}$, is more complicated because it involves the mixing of Y and Ti sites. The authors believe this partial mixing introduces two defect oxygen sites. A susceptibility curve was fit to ZFC measurements, which showed that as oxygen decreased the phase's Curie constant and temperature-independent susceptibility increased. Attempts to create additional phases of $Y_2Ti_2O_7$ failed, which implies that there are phase gaps or a different methodology is required to access the different possible phases.

3.7 SQUID magnetometer

The Superconducting Quantum Interference Device or SQUID is one of the most sensitive experimental techniques available in magnetism. It does not measure the magnetic field directly, but instead measures the changes in current

exiting its superconducting loops of wire (flux transformer). This allows the SQUID sensor to be positioned outside of the sample chamber. This has the benefit of enabling measurements in fields close to the flux transformer's critical field and allowing temperature ranges that correspond to the material limits of the sample chamber. To reduce other sources of flux, the sample end of the flux transformer acts as a second-order gradiometer. This gradiometer produces a unique time-dependent current when a sample is passed through it. Provided that other spurious fluxes are weak or have a different frequency to the sample's time-dependent flux, then a numerical fitting can be made to give the sample's magnetic moment. Since the movement of the sample is precise and regular, the time-dependent current is dependent on sample position. This is then converted into what is referred to as the SQUID voltage. From this the sample's magnetic moment can be extracted. The SQUID has two operating modes: the RSO option and the DC-transport option. The advantage of the RSO option is its higher sensitivity.

Chapter 4

Thin Film Growth

4.1 Equipment

4.1.1 Pulsed Laser Deposition

The thin films were grown using Pulsed Laser Deposition (PLD). A 248 nm excimer laser was used, which delivers 1 Joule of energy per pulse at a rate of 1 to 20 Hz. Its fluence, the amount of radiant energy that is travelling through a particular area, is given by sub 1 J cm^{-2} up to 4 J cm^{-2} at the target. The spot size at the target is adjustable, ranging from less than a millimetre up to a few millimetres. Typically, to maintain uniform growth, substrates with dimensions ranging from 5 mm $\times$ 5 mm to 10 mm $\times$ 10 mm are used. The base pressure of the equipment is 2×10^{-7} Torr and it can accommodate argon or oxygen pressure-controlled environments up to 100s of mTorr. The equipment can also be heated up to 800 °C.

4.1.2 Reflection High Energy Electron Diffraction

Reflection High Energy Electron Diffraction (RHEED) was used to monitor the growth of the thin films. A typical RHEED system has an electron gun that can emit electrons in the energy range of 10 keV to 50 keV. RHEED is a surface sensitive technique. Its probing electrons are aimed such that they hit the sample at a glancing angle of 1 ° to 5 °, which minimises the penetration depth of the technique, ensuring surface sensitive results. The diffracted electrons are detected on a florescent screen. Provided the sample surface is clean and has a crystalline structure, a diffraction pattern will form from the diffracted electrons constructively interfering. RHEED's surface sensitivity makes it an ideal technique to monitor the growth of thin films.

By probing only a 2D surface, RHEED leaves the third direction, perpendicular to the sample surface, without any diffraction conditions, which in reciprocal space causes all reciprocal lattice points to be converted into infinite reciprocal lattice rods. Diffraction conditions in this setup are now fulfilled whenever the reciprocal lattice rods intersect the Ewald sphere. The reflection with the smallest angle to the sample surface, which is also the brightest reflection, is referred to as the zeroth-order beam. The order of the reflections increases as more lattice rods intersect the Ewald sphere.

4.2 Preparation

4.2.1 Laser beam

To measure the energy density of the laser beam, the spot size was measured by firing the laser at Kentek alignment paper. The size of the burn mark was measured by using software which could interact with a microscope's view of the burn mark. An energy meter was used to measure the laser beam's total energy. The microscope, the software used to measure the burn mark, and the energy meter are displayed in Figure 4.1.

4.2.2 Annealing

Before the thin films could be grown on top of the substrates, they first needed to be annealed. This process involved placing the substrates in the centre of a furnace so that they are heated as uniformly as possible. The furnace was set to heat the substrates at a rate of 200 °C per hour up to 850 °C. The substrates were held at 850 °C for 2 more hours before cooling down at a rate of 200 °C per hour. This annealing process aimed to make the substrate more thermodynamically stable. In particular, this process reduces oxygen deficiency in the substrate, which should help improve the films' growth.

After annealing the substrate, it was adhered to the sample platform using silver paste. This process involved heating the sample platform to 90°C and holding it there for 15 minutes. This heating dried out the substrate's silver paste, which fixed it in place. Figure 4.2 displays both the furnace and the small heater that was used in the preparation of the substrates.

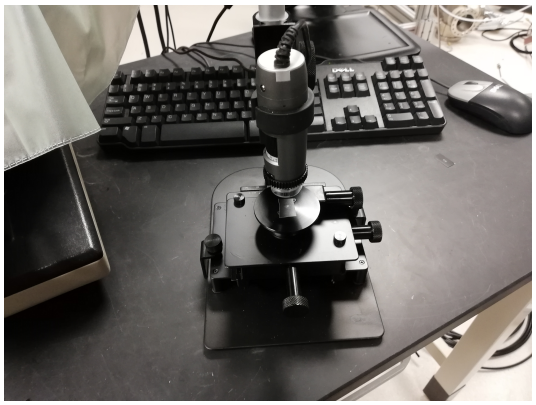

(a) The burn spot was viewed through this microscope.

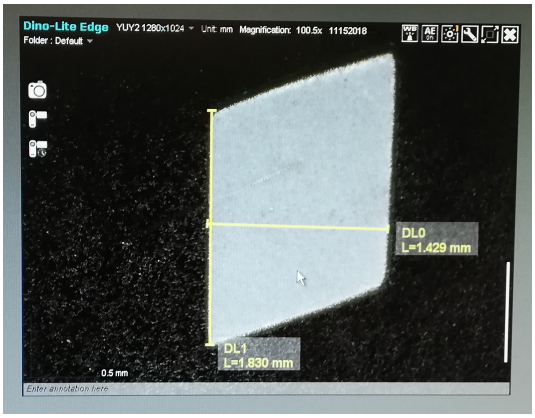

(b) How the burn spot was measured using the software available.

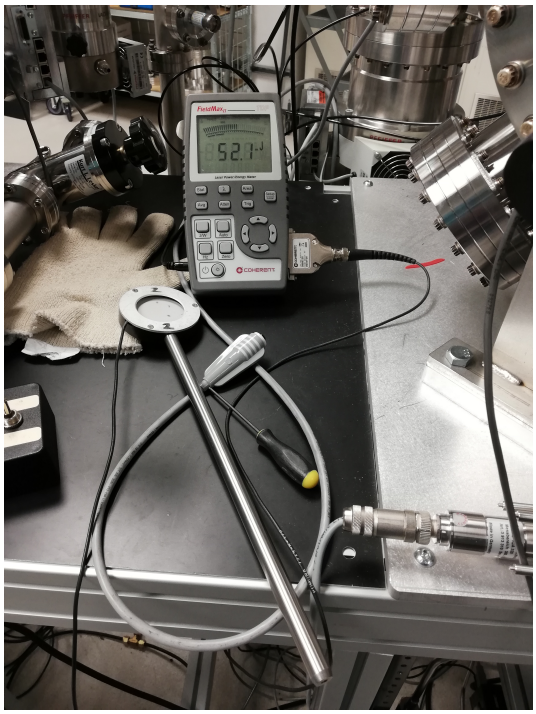

(c) The energy meter used to measure the beam's energy.

Figure 4.1: The equipment used to obtain the laser beam's energy density. (a) The burn spot was small and so this microscope was used to view it. (b) Software was used in conjunction with the microscope to measure the burn spot. (c) The energy of the laser beam was measured using an energy meter.

4.3 Procedure

Before the substrate could be inserted into the Ultra High Vacuum (UHV) equipment, a venting procedure had to be followed. This involved closing all gate valves that were directly connected to the main chamber. Figure 4.3 displays a schematic of the different chambers and valves inside the UHV equipment. The valves are portrayed larger than they are physically so that

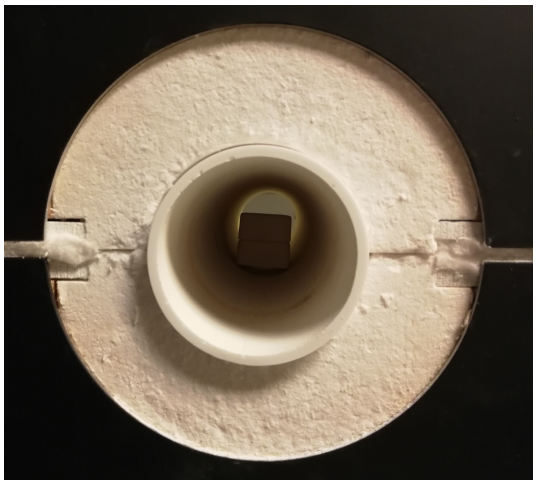

(a) Substrates annealing inside of the furnace.

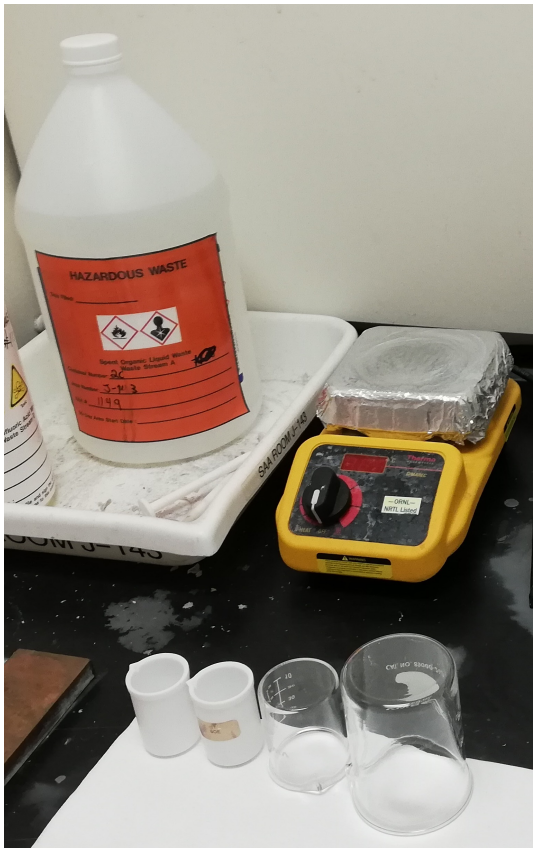

(b) Heater used to adhere the substrates to the sample platform.

Figure 4.2: (a) The substrates were annealed inside this furnace. (b) This heater was used to adhere the samples to the PLD's sample platform, using silver paste as an adhesive.

their connection between different chambers is more clear; the actual size of the valves is displayed in Figure 4.4. After the main chamber was isolated from the rest of the system, the vent inlet was opened, introducing Nitrogen into the chamber. Once the main chamber's pressure reached an atmosphere ($\approx 7 \times 10^2$ Torr), the main chamber was opened and the sample platform was fixed into place. The shutter, which covers the sample platform, was closed. At this point, the beam's total energy was measured using the equipment/procedure that was described earlier, which allowed the energy density to be calculated using equation 4.1.

$$\text{Energy Density} = \frac{\text{Total Energy}}{\text{Spot Size}} \tag{4.1}$$

The energy density thought to be required to grow the desired films lays in the range $\approx 2 \sim 3\,\text{J cm}^{-2}$. This energy density was obtained by placing quartz plates in front of the beam and by changing the aperture size, both of which

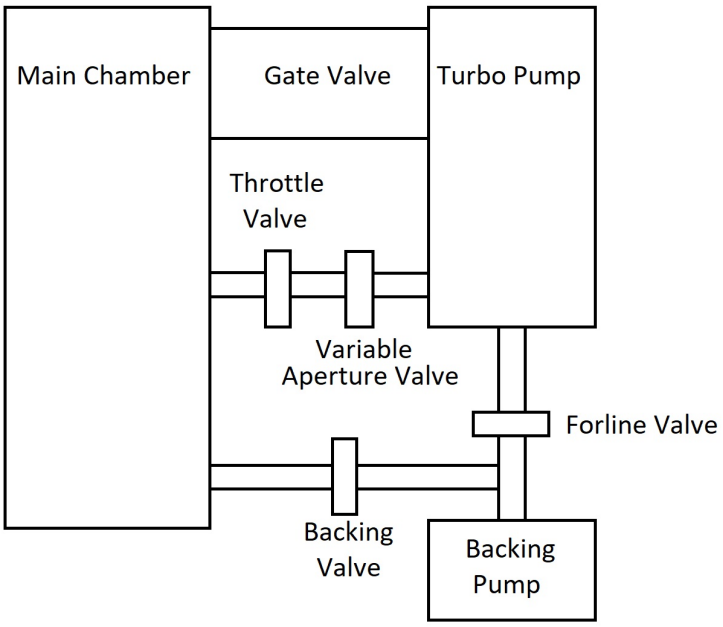

Figure 4.3: Schematic of the different valves and chambers that comprise the UHV equipment that was used at Oak Ridge National Laboratory (ORNL).

are displayed in Figure 4.5. Once the adjustments to the energy density were complete, the main chamber was sealed and the vent inlet was closed. The foreline valve, which connects the turbo pump to the main chamber, was closed (if it was not already). The valve connecting the backing pump to the main chamber was opened. At a pressure of $\approx 10^{-2}$ Torr, the valve to the backing pump was closed and the foreline valve was then opened. This was followed by opening both the gate valve and the throttle valve, which enabled the turbo pump to pump down the main chamber from a safe pressure. The heater was set to 300 °C. This part of the process aimed to eliminate any volatiles (organic matter/solvents) that may have remained inside the silver paint. Next the sample platform was lowered by 1.5 inches, the gate valve was closed and the main chamber ion gauge was switched off. The Oxygen inlet valve was opened and the Oxygen control setting on the computer was set to 30. The aperture between the turbo and the main chamber was set to 0.1 control. The valve pos %, which represents the size of the aperture between the turbo and main chamber, was required to lie between 30 % and 40 %. With these settings, the turbo pump should be using less than 1 A and a stable pressure of ≈ 100 mTorr inside the main chamber should have been created. The main chamber's temperature set point was set to 950 °C, which was later adjusted to give the sample an actual temperature of 750 °C. While the system's temperature was ramping, the RHEED was prepared. This involved adjusting the RHEED's current, the beam's deflection and its horizontal and vertical positions.

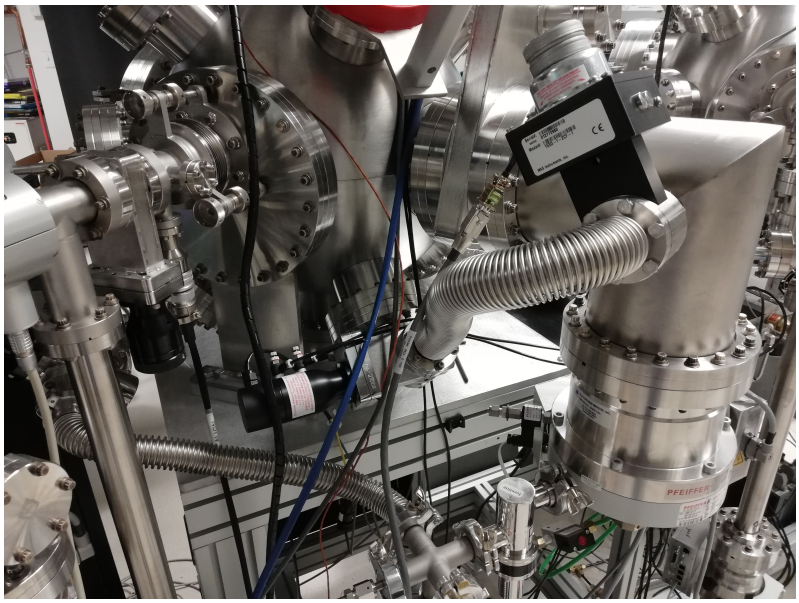

Figure 4.4: The UHV equipment's valves and chambers.

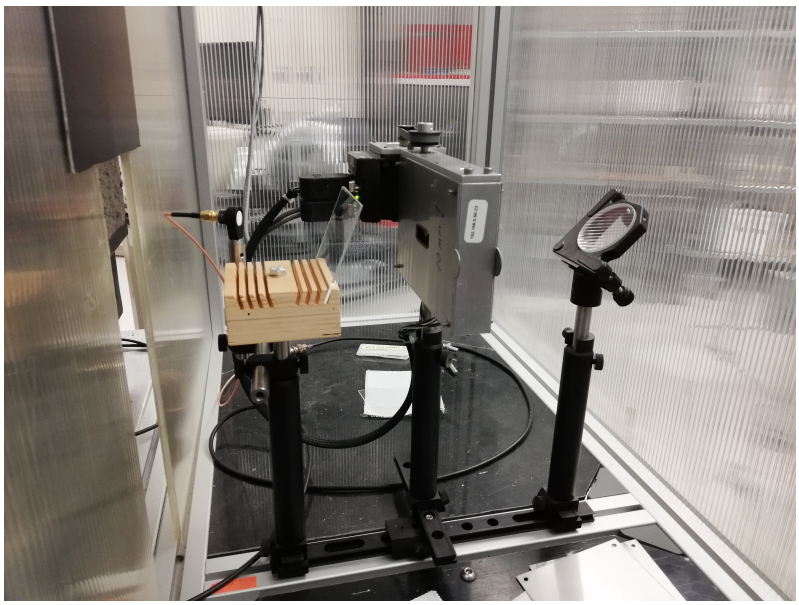

Figure 4.5: The adjustable aperture and the quartz plate holder that was used to change the laser beam's energy density.

The laser had three settings: frequency of shots (Hz), number of shots, and sweeps (mm), all of which could be varied between film growths. Sweeps corresponds to the arc length that the laser traces out on the target, which is set to spin. The combination of a spinning target and the beam's tracing of an arc prevents the formation of a surface, which would be difficult for the laser to ablate. Prior to beginning the film growths, all of the targets were pre-ablated and allowed time to re-oxidise. This involved firing 2000 shots at each target and waiting for the targets to return to their original colours. Once the film had been grown, the RHEED current was turned down to 1 A and the

main chamber was sealed as if it was about to be vented. The small Oxygen inlet valve was closed and the large Oxygen inlet valve was opened. This inlet was closed once the pressure reached 400 Torr. The sample was annealed at this oxygen pressure for 1 hour before the system was cooled down to room temperature. The approximate number of shots needed to grow a specific film thickness was estimated using equation 4.2,

$$S_{\mathrm{x}} = \frac{S_{\mathrm{Previous}}}{T_{\mathrm{Previous}}} \times \frac{E_{\mathrm{Previous}}}{E_{\mathrm{New}}} \times T_{\mathrm{New}} \tag{4.2}$$

where S_{x} is the number of shots for a film of x nm, S_{Previous} is the number of shots used on a previous film, T_{Previous} is the thickness of that previous film, E_{Previous} is the total beam energy used during the previous film's growth, E_{New} is the total beam energy that will be used to grow the new film and T_{New} is the desired thickness of the new film. This equation assumes that the growth is linearly proportionate to the total beam energy. A picture of a PLD plume is shown in Figure 4.6.

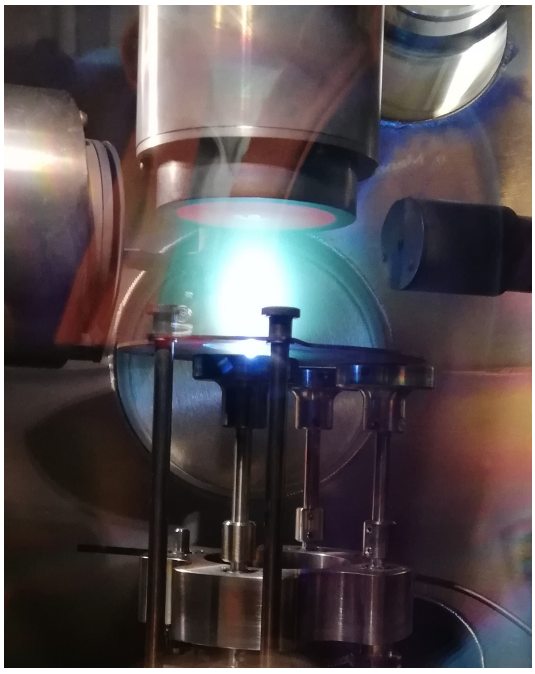

Figure 4.6: A PLD plume during sample growth.

4.4 Grown

The samples presented in this thesis were grown over multiple trips to Oak Ridge National Laboratory (ORNL) and over many years. As a result, different collaborators were present for different growths. For the $Tb_2Ti_2O_7$ samples

Sample number	01	07	16	18
Rare-earth of film	Yb	Dy	Yb	Tb
Out-of-plane direction	[111]	[001]	[001]	[001]
Thickness (nm)	28	500	500	500
Number of pulses	4400	26300	26315	26315
Energy (mJ)	23	53	53	53

Table 4.1: The growth and sample variables of 01:Yb28nm(111), 07:Dy500nm(001)19, 16:Yb500nm(001)19 and 18:Tb500nm(001)19.

Sample number	28	29	30	31	34	21	00	25
Rare-earth of film	Yb	Yb	Yb	Yb	Yb	Tb	Tb	Tb
Out-of-plane direction	[111]	$[1\bar{1}0]$	[100]	[111]	[111]	[100]	[110]	[111]
Thickness (nm)	68	66	68	28	13	62	63	64
Number of pulses	12000	12000	12000	4400	2000			
Energy (mJ)	18	18	18	18	18			

Table 4.2: The growth and sample variables of 28:Yb68nm(111), 29:Yb66nm($1\bar{1}0$), 30:Yb68nm(100), 31:Yb28nm(111) and 34:Yb13nm(111). The sample variables for the $Tb_2Ti_2O_7$ samples that are presented in this thesis are given, but not their growth variables.

presented in the $Tb_2Ti_2O_7$ chapter, Dr. Laura Bovo and Dr. Christopher Rouleau were present. All the samples presented in the $Yb_2Ti_2O_7$ chapter apart from sample 01:Yb28nm(111) were grown by Prof. Hidekazu Kurebayashi and Dr. Christopher Rouleau. The remaining samples presented in this thesis were grown by myself, Prof. Hidekazu Kurebayashi and Dr. Christopher Rouleau. Table 4.1 displays the details of the samples grown by myself, Prof. Hidekazu Kurebayashi and Dr. Christopher Rouleau. Table 4.2 displays the details of the other samples presented in this thesis. The sections for number of pulses and energy used to grow the $Tb_2Ti_2O_7$ samples in Table 4.2 have been left blank because this information could not be found.

There is a variety of samples that have been grown at ORNL that have not been presented in this thesis. Attempts were made in the last trip to ORNL to grow thin films of $Gd_2Ti_2O_7$ and $Nd_2Ir_2O_7$ on $Y_2Ti_2O_7$ substrates. Thin films of $Gd_2Ti_2O_7$ were grown, but reflectivity measurements suggested that the films had not grown properly. The $Nd_2Ir_2O_7$ film growth was also unsuccessful because the $Nd_2Ir_2O_7$ target was not dense enough and so it began to fall apart when it was shot by the laser. Different combinations of $Yb_2Ti_2O_7$, $Dy_2Ti_2O_7$ and $Tb_2Ti_2O_7$ bilayers were grown on $Y_2Ti_2O_7$ substrates. Multilayers of $Dy_2Ti_2O_7$ and $Y_2Ti_2O_7$ were also grown with the hope of investigating how the layers of $Dy_2Ti_2O_7$ responded to being strained on both sides by $Y_2Ti_2O_7$.

Chapter 5

$Yb_2Ti_2O_7$ Thin Films

5.1 Sample notation

All samples investigated will be referenced using the following nomenclature:

$$S : RET\text{nm}(hkl)YG$$

where S, RE, T, hkl and YG correspond to the sample number, the rare-earth ions inside of the film titanate, the film's thickness, the sample's out-of-plane crystallographic direction (direction perpendicular to its surface) and the year the film was grown respectively. The units of the film's thickness are nm, which remains unchanged in the sample nomenclature.

The substrate nomenclature is slightly different and is given below:

$$YTO(hkl)YG$$

where YTO corresponds to $Y_2Ti_2O_7$ (the only type of substrate that is used in this thesis), (hkl) is the substrate's out-of-plane crystallographic direction and YG is the year the substrate batch was used to grow thin film samples.

5.2 $Yb_2Ti_2O_7$ thin films

This chapter will report the experimental results of the first $Yb_2Ti_2O_7$ thin films grown on $Y_2Ti_2O_7$ substrates. Two series of $Yb_2Ti_2O_7$ thin films were investigated. The first series probes how epitaxial strain affects the films' specific heat, magnetometry and growth. By growing films that have different out-of-plane directions, epitaxial strain is applied along different crystal axes. The films in this series are referred to as 28:Yb68nm(111), 29:Yb66nm($1\bar{1}0$) and 30:Yb68nm(100). The second series investigates the thickness-dependence of

the films' specific heat, magnetometry and growth. The samples in this series are referred to as 28:Yb68nm(111), 31:Yb28nm(111) and 34:Yb13nm(111). For reasons that will become clear later in this chapter, 28:Yb68nm(111) will only be referred to in the thickness series and another sample, 01:Yb28nm(111), will be discussed separately.

5.3 Investigation of the epitaxial strain effects on $Yb_2Ti_2O_7$

5.3.1 X-ray procedure

The X-ray procedure for the $Yb_2Ti_2O_7$ thin films begins with an optics alignment. This involved a 10 mm length-limiting slit (limits horizontal beam divergence), a parallel beam slit (produces a vertically parallel beam), a D/teX detector (a 1D high resolution silicon strip detector) and a Hooked sample platform attachment. After the optics alignment was completed, the sample alignment could begin. The receiving and incident slits were set to 0.03 mm (minimum setting for maximum resolution) and the attenuation was set to automatic to avoid accidentally exposing the sensitive detector to a damaging amount of X-rays. The incident beam was first aligned to the sample surface in preparation for a reflectivity scan. This involved first aligning the Z parameter, which controls the height of the sample platform. The Z scan produces a step-like function, which starts off at a high intensity because nothing is blocking the X-ray source and the detector. This intensity then drops when the sample begins blocking the incident beam. The Z value was set to the step's middle point (middle of the intensity, not the Z value). The parameters ω and 2θ correspond to the angles that the X-ray source and the detector make with the sample. 2θ was set to a glancing angle of 0.5°and an ω scan was performed around 0°. After this ω was set to the peak value and $2\theta/\omega$ was set to zero. This normally leaves a non-zero value of ω, which is the the ω offset. This offset takes into account the sample tilt, which the equipment does not do automatically. A follow-up Z scan was carried out and again Z was set to the middle value of the step's drop in intensity. At this point, Z has been completely aligned.

The Y parameter shifts the sample platform perpendicularly to the X-ray beam and the Z direction. Y scans create an intensity curve in the shape of a trough. The Y parameter is aligned by setting its value to the minimum of this trough, which corresponds to the beam being in the centre of the sample. Next the 10 mm length-limiting slit was swapped for a 2 mm slit,

which improved the resolution. The incident slit was changed to 0.5 mm and the two receiving slits were changed to 0.3 mm, which increased the signal strength. The reflectivity was measured by scanning 2 θ/ω from 0.4 to 10°. Then a substrate peak from a specular reflection (reflections that have the same incident and exit angles) was used to fix the value of $2\theta/\omega$. The X parameter shifts the sample platform perpendicularly to both the Z and Y directions. The X scan's intensity resembles a wide step because the intensity drops rapidly once the X-ray beam moves off the sample at either end of the scan. The X value was set to the middle of this step to ensure the beam is on the sample. An off-specular reflection, reflections that have different incident and exit angles, was found (through powder diffraction experiments in the literature) to align the ϕ angle. To improve the resolution, the off-specular peak needs to have a non-zero χ value, where χ is the angle that carves out the transversal plane to ϕ. There are fewer reflections with a finite χ value and so a diverging beam can align more precisely to one of those peaks. The ϕ value was set to a high-angle off-specular reflection (while retaining any offset), which had $\chi = 0$. It is important that this reflection has $\chi = 0$ so that a RSM will display a vertical slice through the sample instead of an angled slice, which is more challenging to interpret. A sample alignment macro was run on the original specular peak, which causes the equipment to zero the ω offset that the sample tilt introduced for this particular ϕ. A RSM was then performed on the off-specular reflection.

5.4 X-ray diffraction measurements

X-Ray Diffraction (XRD) was used to find out two properties of each film. The first was the thickness of the films, which was determined from reflectivity analysis. The second property investigated was the films' epitaxial strain. RSMs were carried out to verify if the films were or were not fully strained.

The samples' reflectivity was measured up to a maximum of 10°, but their signal was normally below the detectable threshold well before 10°. Standard software supplied with the instrument was used to subtract the background intensity and fit a number of sample properties. These sample properties included the type of material, its density and roughness, the number of sample layers and their thicknesses. Table 5.1 displays the outputted reflectivity values of the all of the $Yb_2Ti_2O_7$ samples in both series. The density values outputted were used in calculating the films' masses, which was cause for concern when their reliability was called into question. The film masses were calculated using reported bulk densities and were compared with the measured ones.

Sample number	28	29	30	31	34
Sample orientation	[111]	[1$\bar{1}$0]	[100]	[111]	[111]
Layer 1 thickness (nm)	2.754(9)	3.00(13)	1.4(3)	1.542(17)	1.357(4)
Layer 2 thickness (nm)	62.91(13)	59.3(3)	64.9(3)	21.30(4)	8.777(4)
Layer 3 thickness (nm)	2.66(9)	4.1(3)	1.28(10)	5.3(5)	3.13(3)
Film Thickness (nm)	68.3(2)	66.4(4)	67.6(4)	28.1(5)	13.26(3)
Layer 1 density (gcm^{-3})	5.63(4)	7.56(6)	3.8(3)	6.12(3)	9.038(16)
Layer 2 density (gcm^{-3})	7.50(5)	7.40(4)	7.21(9)	7.76(4)	7.887(17)
Layer 3 density (gcm^{-3})	6.66(12)	7.18(4)	5.88(8)	5.67(5)	5.439(16)
Sample Mass (μg)	33(1)	33(1)	34(1)	32(1)	32(1)

Table 5.1: The reflectivity values of samples 28:Yb68nm(111), 29:Yb66nm(1$\bar{1}$0), 30:Yb68nm(100), 31:Yb28nm(111) and 34:Yb13nm(111), where three film layers have been fitted: layer 1 corresponds to the top-most film layer, layer 2 to the middle layer and layer 3 to the bottom-most layer.

The difference between the film masses was not significant enough to justify changing the results. The reflectivity results and fit are shown in Figure 5.1. Three film layers were plotted for each sample to account for any difference in the surface and interface regions.

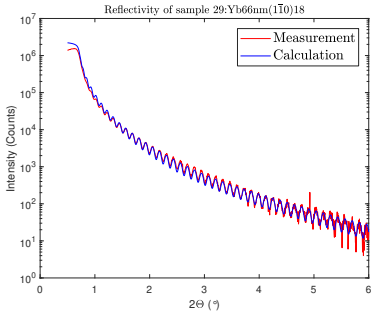

(a) Reflectivity results of sample 29:Yb66nm(1$\bar{1}$0).

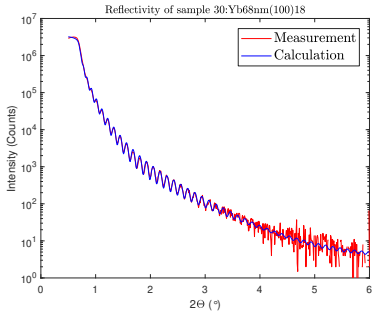

(b) Reflectivity results of sample 30:Yb68nm(100).

Figure 5.1: The reflectivity results of samples (a) 29:Yb66nm(1$\bar{1}$0) and (b) 30:Yb68nm(100).

The film and substrate out-of-plane lattice constants were determined from scans of specular reflections. Figure 5.2 displays the specular reflections of both 29:Yb66nm(1$\bar{1}$0) and 30:Yb68nm(100). The out-of-plane lattice constant was calculated using Bragg's law, which is given by equation 5.1:

$$n\lambda = 2d\sin\theta \tag{5.1}$$

where n is an integer, λ is the X-ray beam's wavelength, d is the distance between the lattice planes and θ is the angle between the incident X-ray beam and the sample's surface plane. Since $Y_2Ti_2O_7$ has a cubic structure, the out-of-plane lattice parameter should be equal to its in-plane lattice parameters,

assuming the substrate lattice's structure has not been warped by the film; warping is unlikely because the films are thin compared with the substrates. It is thought that the films have grown epitaxially, meaning the in-plane lattice parameter of the $Y_2Ti_2O_7$ substrate should match the $Yb_2Ti_2O_7$ thin films'. If the thin films are not fully strained, the in-plane lattice parameter can change as a function of distance from the substrate.

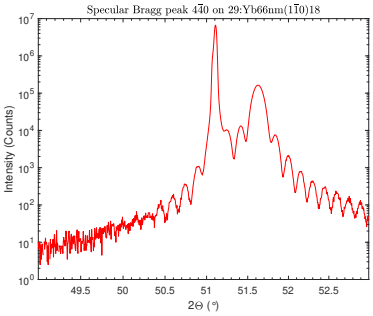

(a) 4$\bar{4}$0 specular reflection of sample 29:Yb66nm(1$\bar{1}$0).

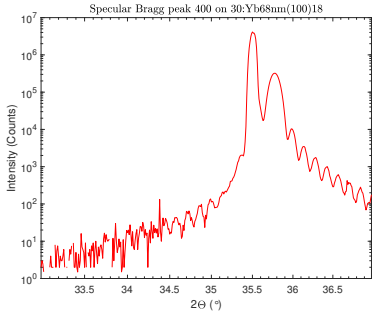

(b) 400 specular reflection of sample 30:Yb68nm(100).

Figure 5.2: (a) The specular reflections of samples 29:Yb66nm(1$\bar{1}$0) and (b) 30:Yb68nm(100).

A RSM was performed on each film to verify if they were strained. If the films had relaxed then their peak would appear in reciprocal space as a streak. Figure 5.3 displays the RSMs of samples 29:Yb66nm(1$\bar{1}$0) and 30:Yb68nm(100). These RSMs and all of the other RSMs which are presented in this thesis use a logarithmic colour scale that is based on the scan's number of counts (intensity).The brightest spot on each RSM should correspond to the substrate's peak because the substrates are significantly thicker than their films and so should have a stronger signal. For both samples the peaks appeared as spots instead of streaks. Thus, the films' and substrates' lattice constants remained constant throughout the samples. The substrate and film peaks are also positioned directly on top of each other, which means they share the same in-plane lattice constant. These features are consistent with fully strained films. The RSMs in Figure 5.3 are a factor of $\sqrt{2}$ off of the stated Miller index value for one of their axes. This is due to a different basis being used, which will be discussed further later in the chapter.

5.4.1 Magnetometry measurements

There are two magnetometry measurements that were performed on each $Yb_2Ti_2O_7$ sample using a Quantum Design MPMS 2 system. These measured the size of a sample's magnetic moment as a function of applied field or

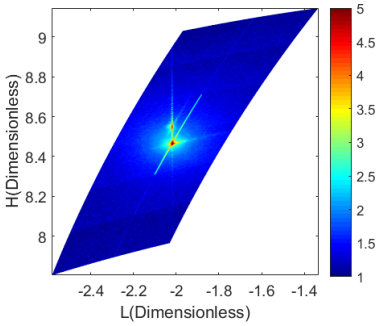

(a) RSM of 29:Yb66nm($1\bar{1}0$).

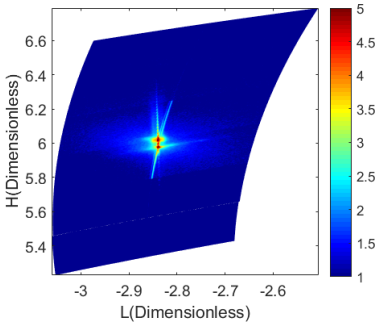

(b) RSM of 30:Yb68nm(100).

Figure 5.3: (a) RSMs around the 662 reflection on sample 29:Yb66nm($1\bar{1}0$) and (b) 30:Yb68nm(100).

temperature. The measurements will be referred to as M vs H and M vs T respectively, where M refers to the sample's magnetisation, H refers to the applied magnetic field and T refers to the sample temperature.

Before going further, it is important to explain a notation that is used for the M vs H and M vs T results. Figure 5.4 is a graphical representation of the sample shape and applied field geometry. The relative direction of the applied field has been chosen to be the sample plane parallel with the applied field, $[\bar{1}\bar{1}2]$.

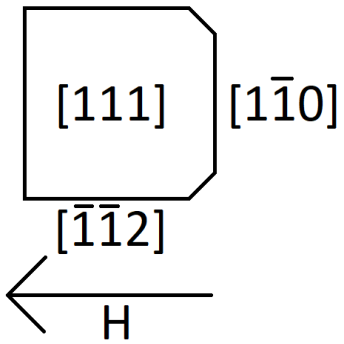

Figure 5.4: How the applied field's direction relates to the sample's physical shape (the sample's in-plane crystal directions have been labelled for reference). In this example, the applied field is directed along the sample's $[\bar{1}\bar{1}2]$ direction. The corners of the sample were cleaved off so that the sample orientation could be easily identified.

M vs H

The M vs H measurement entails increasing the applied magnetic field to 70000 Oe (7 tesla), reducing the applied field to -70000 Oe (-7 tesla) and then increasing the applied field to 0 Oe (0 tesla). Some points were removed from the raw data for display purposes and the substrate data was scaled to

match the corresponding sample mass. Originally, the magnetic moment of the scaled substrates was subtracted from the magnet moment of the samples, leaving only the films' contribution. This was carried out because only the magnetic properties of the films are of interest. The magnet moment of the films was converted into the films' magnetisation by multiplying by the mass per Yb ion and then dividing by the films' mass and Bohr magneton.

This type of analysis produced an unexpectedly high magnetisation in all of the films. The theoretical ground state of $Yb_2Ti_2O_7$ is calculated below:

$$\mu = g_{\mathrm{J}} m_{\mathrm{J}} \tag{5.2}$$

where g_{J} is given by:

$$g_{\mathrm{J}} = \frac{3}{2} - \frac{L(L+1) - S(S+1)}{2J(J+1)} \tag{5.3}$$

For $Yb_2Ti_2O_7$, $g_{\mathrm{J}} = 1.14$ and $J = L + S = 3 + 0.5 = 3.5$, which gives the theoretical ground state of $\mu = 4\ \mu_{\mathrm{B}}(\mathrm{Yb}^{3+}\ \mathrm{ion})^{-1}$. It has been reported that bulk $Yb_2Ti_2O_7$ has a magnetic moment of $\sim 3.25\ \mu_{\mathrm{B}}(\mathrm{Yb}^{3+}\ \mathrm{ion})^{-1}$ [25, 29]. The M vs H results of sample 29:Yb66nm($1\bar{1}0$) are displayed in Figure 5.5. In all of the films' M vs H graphs, there is a kink in the magnetic signal, which has been enclosed by a black circle. It is thought that these kinks may arise due to impurities in the substrate, which is strongly supported by M vs T results that are shown later. The dashed line represents the maximum measurable theoretical value of sample 29:Yb66nm($1\bar{1}0$) assuming there is perfect $\langle 111 \rangle$ anisotropy. The derivation of this can be seen in Appendix A. If the magnetisation at the kink was subtracted from the saturation magnetisation then the film saturation moment would lie close to this dashed line. However, this is most likely a coincidence because the bulk is reported to have x-y spins rather than Ising spins.

A different method of analysis was devised to better take into account the suspected impurities inside of the substrates. This method involved fitting equation 5.4 to the sample data.

$$M = \chi_{\mathrm{VV}} H + \tilde{\mu}\tilde{n}c_1 \tanh\left(\frac{c_2\tilde{\mu}H}{T}\right) \tag{5.4}$$

Where χ_{VV} is the Van Vleck (VV) susceptibilty (temperature-independent susceptibility arising from the second-order Zeeman effect), H is the applied field, $\tilde{\mu}$ is the magnetic moment of the paramagnetic ions, $\tilde{n}$ is the proportion of the sample that is made up of magnetic ions (impurities or impurities plus film ions), T is the sample temperature and c_1 and c_2 are both constants with the

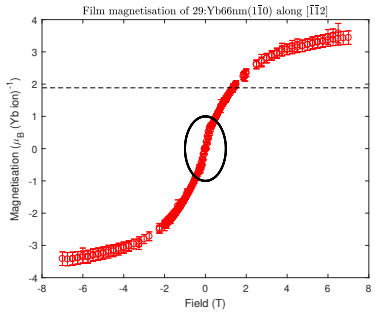

Figure 5.5: The film magnetisation of sample 29:Yb66nm(1$\bar{1}$0) with an applied field along its [$\bar{1}\bar{1}$2] crystal direction. The dashed line corresponds to the theoretical maximum measurable value and the black circle highlights a kink in the magnetic signal.

values 1.44×10^5 m$^{-3}\mu_B$ and 8.44×10^{-7} H m$^{-1}\mu_B$ respectively. The constants c_1 and c_2 represent $\mu_B n_0$ and $\mu_B \mu_0$ respectively, where n_0 is the number of titanium atoms per unit volume.

Equation 5.4 requires both the raw magnetic moment and the applied field to be in Am^{-1}. The conversion of emu to Am^{-1} is given by 1 emu = 1 erg/G = 10^{-3} Am^{-1} and the conversion of Oe to Am^{-1} is given by 1 Oe = 79.58 Am^{-1}. Equation 5.4 has two terms, which represent two different sources of magnetisation in the sample. The first term represents the VV contribution, which comes from both the film and the substrate. However, the film's contribution to the VV is negligible compared with the substrate's and so is ignored. The second term represents the effective spin 1/2 paramagnetic impurities in a substrate per Ti ion, or when applied to a sample it represents both the effective spin 1/2 paramagnetic impurities and the film's magnetic ions per Ti ion. The proportion of magnetic ions is calculated by assuming that all of the ions, impurities plus film ions, are spin 1/2 paramagnets. The film ions should be spin 1/2 paramagnets.

Table 5.2 presents the fitted variables of three substrates from different batches. The aim was to ascertain if the level of impurities varied significantly in the substrates. If the level was consistent, the magnetic moment from the substrate could be subtracted from each sample to give each films' contribution. It can be seen that this is not the case, and so a more subtle approach to the analysis was required.

Table 5.3 displays the fitted variables for each sample when a field is applied along each of samples' in-plane crystal directions. There is an extra variable in Table 5.3 compared with Table 5.2. This variable represents the films' magnetic moment and is calculated using equation 5.5, where μ_{Film} is the film magnetic moment, T_{Film} is the film thickness, $T_{\text{Substrate}}$ is the substrate thickness, $\tilde{n}$ is

Substrate batch year	15	18	19
$\chi_{VV}(10^{-5})$	1.3(3)	1.23(1)	1.08(1)
$\tilde{\mu}$ (μ_B)	$2(2) \times 10^1$	3.8(1)	10(2)
$\tilde{n}(10^{-5})$	0.1(2)	5.0(2)	0.5(1)

Table 5.2: The M vs H fitted parameters of three $Y_2Ti_2O_7$ substrates that belonged to different crystal rods.

Sample	28	28	29	29	30	30
Field direction	$[\bar{1}\bar{1}2]$	$[1\bar{1}0]$	$[\bar{1}\bar{1}2]$	[111]	Fit 1	Fit 2
$\chi_{VV}(10^{-5})$	0.93(1)	1.27(2)	2.00(6)	2.15(7)	2.16(6)	2.02(7)
$\tilde{\mu}$ ($\mu_B(Yb^{3+}$ ion$)^{-1}$)	4.8(2)	4.8(2)	2.6(1)	2.9(1)	2.6(1)	2.5(1)
$\tilde{n}((10^{-5})$ (Ti ion$)^{-1}$)	4.0(2)	4.1(2)	21(1)	18(1)	23(2)	24(2)
μ ($\mu_B(Yb^{3+}$ ion$)^{-1}$)	20(2)	20(2)	2.1(2)	2.7(3)	1.9(3)	1.7(2)
Sample	31	31	34	34	01	01
Field direction	$[\bar{1}\bar{1}2]$	$[1\bar{1}0]$	$[\bar{1}\bar{1}2]$	$[1\bar{1}0]$	$[\bar{1}\bar{1}2]$	$[1\bar{1}0]$
$\chi_{VV}(10^{-5})$	1.59(4)	1.26(2)				
$\tilde{\mu}$ ($\mu_B(Yb^{3+}$ ion$)^{-1}$)	2.5(1)	2.7(1)				
$\tilde{n}((10^{-5})$ (Ti ion$)^{-1}$)	11(1)	8.2(5)				
μ ($\mu_B(Yb^{3+}$ ion$)^{-1}$)	1.5(2)	2.3(3)				

Table 5.3: The fitted M vs H parameters of the $Yb_2Ti_2O_7$ samples. Samples 28:Yb68nm(111), 29:Yb66nm($1\bar{1}0$), 30:Yb68nm(100), 31:Yb28nm(111), 34:Yb13nm(111) and 01:Yb28nm(111) are referred to in the table as 28, 29, 30, 31, 34 and 01 respectively. See the main text for why some sections were left empty.

the proportion of paramagnetic ions per Ti ion (film ions + impurities) and μ_{Fit} is the fitted sample magnetic moment. Some columns have been left blank due to the fitting failing.

$$\mu_{Film} = \left(\frac{\left(\frac{T_{Film}}{T_{Substrate}} \right)}{\tilde{n}} \right) \times \mu_{Fit} \tag{5.5}$$

Figure 5.6 displays the fitted data of samples 29:Yb66nm($1\bar{1}0$) and 30:Yb68nm(100) with magnetic fields applied along each in-plane direction. The fits appear to match the data well. The calculated film magnetic moment of sample 29:Yb66nm($1\bar{1}0$) along the crystal direction $[\bar{1}\bar{1}2]$ is 2.1(2) $\mu_B(Yb^{3+}$ ion$)^{-1}$ and 2.7(3) $\mu_B(Yb^{3+}$ ion$)^{-1}$ along the [111] direction. Both directions for sample 30:Yb68nm(100) should have the same moment because of its symmetry. The two values obtained are 1.9(3) $\mu_B(Yb^{3+}$ ion$)^{-1}$ and 1.7(2) $\mu_B(Yb^{3+}$ ion$)^{-1}$. In all cases, the values obtained along each direction fall short of the bulk value ≈ 3.25 μ_B. A possible explanation for this is the films have different anisotropy to the bulk. It is also possible that the values obtained are inflated from ferromagnetic impurities, which the fit does not take into account.

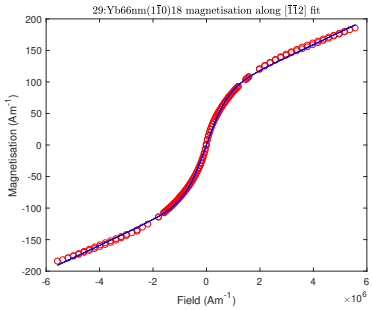

(a) M vs H of sample 29:Yb66nm(1$\bar{1}$0) with an applied magnetic field along its [$\bar{1}\bar{1}$2] direction.

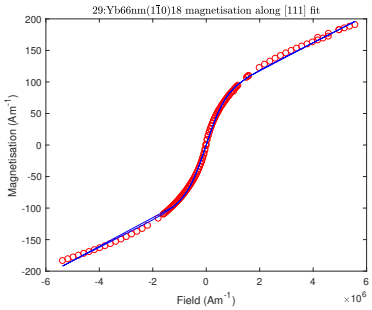

(b) M vs H of sample 29:Yb66nm(1$\bar{1}$0) with an applied magnetic field along its [111] direction.

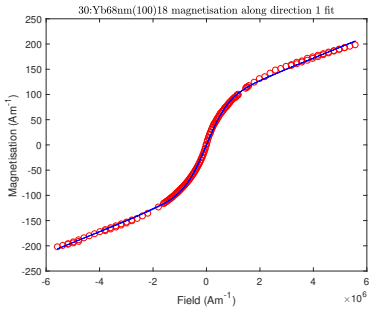

(c) M vs H of sample 30:Yb68nm(100) with an applied magnetic field along its first direction.

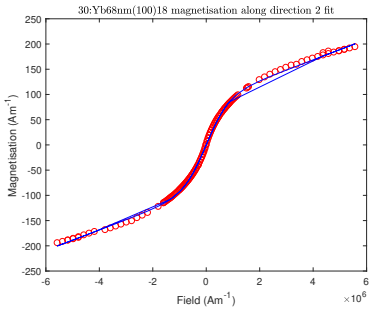

(d) M vs H of sample 30:Yb68nm(100) with an applied magnetic field along its second direction.

Figure 5.6: The fitted M vs H results of samples 29:Yb66nm(1$\bar{1}$0) and 30:Yb68nm(100). The magnetic field was applied along the samples' in-plane crystal directions.

M vs T

There are two different M vs T measurements that were carried out: ZFC and FC. The ZFC measurements involved cooling the sample from 300 K to 1.8 K without an applied field. A field of 0.1 tesla was then applied and the sample was heated back to 300 K. Data for this type of measurement is only recorded when the sample is being heated. The FC measurements are similar to the ZFC measurements, but differ in that an applied field is present during both heating and cooling phases. An applied field of 0.1 tesla was used for all FC measurements. Prior to beginning the ZFC measurements, an M vs H measurement was taken from -0.1 tesla to 0.1 tesla. This measurement is important because any unexpected ferromagnetic signals could result in the sample having a non-zero remanence. All of the samples measured throughout this thesis had a negligible remanence and so it was not subtracted off.

Figure 5.7 presents the sample's and scaled substrate's magnetic moment vs temperature, after some points were removed for display purposes. There

are two features in both M vs T graphs, which are consistent with impurities in the samples. These features are a high temperature magnetic moment and a splitting of FC and ZFC measurements. A high temperature moment is characteristic of ferromagnetic impurities because at higher temperatures a strong exchange interaction is required to maintain magnetisation. The splitting between FC and ZFC measurements is also consistent with ferromagnetic impurities because ferromagnetic materials have hysteresis and so their magnetic moments are dependent on their environment's history. Both of these features can be seen in the scaled substrate data, which implies that the cause of the unexpectedly large magnetic signals in the M vs H graphs comes from impurities in the substrates instead of in the films. It is possible that there are impurities in the film too, but there is not a way of deducing this without a pure substrate.

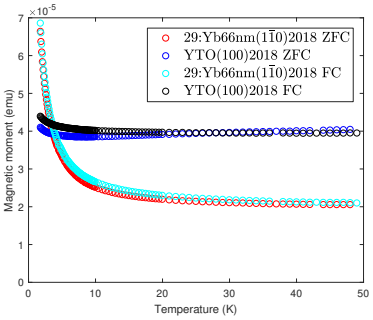

(a) FC and ZFC measurements of sample 29:Yb66nm(1$\bar{1}$0) and its corresponding scaled substrate.

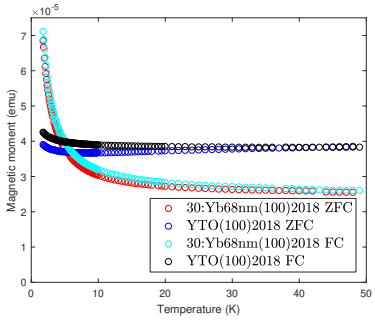

(b) FC and ZFC measurements of sample 30:Yb68nm(100) and its corresponding scaled substrate.

Figure 5.7: The M vs T measurements for samples 29:Yb66nm(1$\bar{1}$0) and 30:Yb68nm(100) with their correspondingly scaled substrates.

5.4.2 Specific heat measurements

The specific heat analysis of the $Yb_2Ti_2O_7$ thin films proved to be challenging, so multiple methods were attempted.

First attempt of analysis

The raw sample heat capacity data was processed through a number of steps. To begin with, the data was converted from its outputted units, μJK^{-1} to JK^{-1}. The samples were weighed and in each analysis the measured substrate's heat capacity was scaled to match the sample's weight. Using reflectivity measurements, the thickness of the $Yb_2Ti_2O_7$ films and their densities were

acquired. This data was used alongside micrometer measurements of the sample's in-plane dimensions to calculate the mass of the thin films. The Yb molar mass was calculated using the atomic units of $Yb_2Ti_2O_7$. The substrate data was shifted such that a particular point was equal to a point in the sample data. The justification for this scaling is talked about below. The sample heat capacity can be broken down into different sources of heat capacity. This is expressed in equation 5.6 below:

$$C_{\text{Sample}} = (C_{\text{Phononic}_{\text{Substrate}}}) + \left(C_{\text{Magnetic}_{\text{Film}}} + C_{\text{Phononic}_{\text{Film}}}\right) \tag{5.6}$$

where C_{Sample} is the sample heat capacity, $C_{\text{Phononic}_{\text{Substrate}}}$ is the substrate's phononic heat capacity, $C_{\text{Magnetic}_{\text{Film}}}$ is the film's magnetic heat capacity and $C_{\text{Phononic}_{\text{Film}}}$ is the film's phononic heat capacity. The shifted substrate was subtracted from the sample data in order to remove both phononic contributions to the heat capacity. The film's magnetic heat capacity was divided by its measured mass to acquire the film's magnetic specific heat. This was then divided by the sample temperature and multiplied by the Yb molar mass to give the film's magnetic specific heat in JK^{-1} (Yb ion)$^{-1}$. The film's entropy was calculated by summing rectangles under the film's magnetic specific heat divided by the temperature curve.

As mentioned above, the initial attempt at the analysis of the $Yb_2Ti_2O_7$ thin films involved scaling the substrate's heat capacity by a value such that it overlapped with the sample heat capacity. This method of analysis was attempted first due to its success in the analysis of the $Tb_2Ti_2O_7$ thin films. This method utilises the low temperature limit of the Debye model, which predicts the phononic heat capacity to be $\propto T^3$. The low temperature limit of the Debye model is shown in equation 5.7 below:

$$C = \frac{12Nk_{\text{B}}\pi^4}{5}\left(\frac{T}{\Theta_{\text{D}}}\right)^3 \tag{5.7}$$

where N is the number of atoms, T is the temperature and Θ_{D} is the Debye temperature. The Debye temperature is a variable that was created to absorb all of the material-specific contributions to the phononic heat capacity. The properties absorbed in the Debye temperature are the material's elastic coefficients and its volume per atom. In practice, there is some variance in the temperature-dependence of a material's phononic heat capacity at low temperatures. However, the temperature-dependence of two materials with an almost identical structure should be virtually the same at the low temperature limit. The decision to shift the substrate's heat capacity was justified through the assumption that the temperature-dependence of the substrate's phononic

heat capacity was the same as the sample's (film and substrate) temperature-dependence. This justification was also used in the analysis of the $Tb_2Ti_2O_7$ thin films.

This scaling method ensures that there is a point after the subtraction that equals zero. This is useful because the crystal field energy levels of $Yb_2Ti_2O_7$ are separated by such a large margin that the only contribution to the sample's heat capacity beyond the ground state magnetic contribution is the phononic heat capacity. Thus, after the subtraction, the heat capacity should equal approximately zero beyond the scaled point.

Measurements of bulk $Yb_2Ti_2O_7$'s heat capacity, by Arpino [29], has shown that beyond approximately 10 K the $Yb_2Ti_2O_7$ heat capacity matched the heat capacity of $Lu_2Ti_2O_7$. The heat capacity of $Y_2Ti_2O_7$ and $Lu_2Ti_2O_7$ should be similar since they are both non-magnetic materials with the same structure. As a result, the substrate heat capacity was scaled such that a point ~ 10 K was equal to the sample heat capacity. Initially, the substrate heat capacity was scaled to different points depending on the film. This approach to the scaling was discarded because the results it produced were not the expected results and a less arbitrary approach was desired. This desire led to a standardised point to which the substrate heat capacity could be shifted. The point chosen was between 10 K and 11 K because it was close to where the $Lu_2Ti_2O_7$ matched the bulk $Yb_2Ti_2O_7$ heat capacity and this value gave the expected entropy for two of the films. The shifted substrate and the following results for samples 29:Yb66nm($1\bar{1}0$) and 30:Yb68nm(100) are shown in Figure 5.8. Figure 5.8a displays the heat capacity of the samples with their corresponding substrate heat capacities. Figure 5.8b displays the magnetic heat capacity of the films. This plot was created by subtracting the substrate data in Figure 5.8a from their corresponding sample data set. Figure 5.8c displays the magnetic specific heat divided by the temperature of the films. This plot is obtained by dividing the film data in Figure 5.8b by the temperature and by the film's number of Yb moles. Figure 5.8d displays the magnetic entropy of the films. This plot was obtained by summing rectangular areas under the plots in Figure 5.8c. The dashed line in Figure 5.8d corresponds the expected value of $R\ln(2)$. Both samples 29:Yb66nm($1\bar{1}0$) and 30:Yb68nm(100) give approximately the expected entropy. This entropy corresponds to two available microstates for each spin (up and down), implying that these samples do not obey the ice rules.

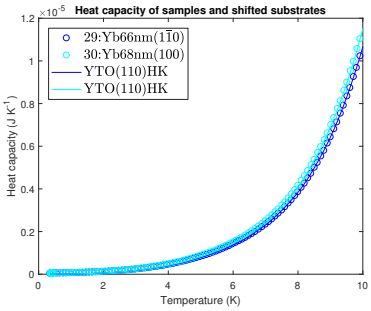

(a) The heat capacities of samples 29:Yb66nm(1$\bar{1}$0) and 30:Yb68nm(100) and their correspondingly shifted substrate heat capacities. The sample heat capacity is represented by the circles and the shifted substrate heat capacities are represented by the lines.

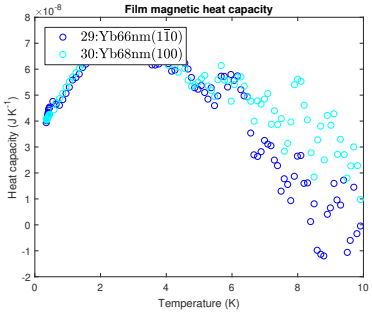

(b) The film magnetic heat capacities of samples 29:Yb66nm(1$\bar{1}$0) and 30:Yb68nm(100).

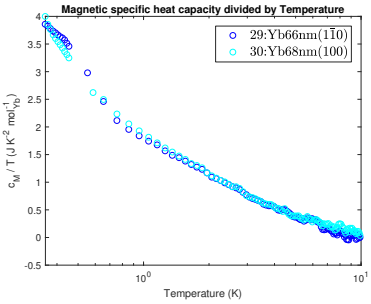

(c) The magnetic film specific heat divided by the temperature of samples 29:Yb66nm(1$\bar{1}$0) and 30:Yb68nm(100).

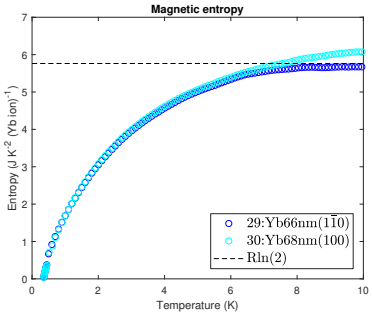

(d) The magnetic film entropies of samples 29:Yb66nm(1$\bar{1}$0) and 30:Yb68nm(100).

Figure 5.8: The first attempt at the heat capacity analysis of samples 29:Yb66nm(1$\bar{1}$0) and 30:Yb68nm(100). The colours dark blue and light blue correspond to the samples 29:Yb66nm(1$\bar{1}$0) and 30:Yb68nm(100) respectively.

Second attempt of analysis

The second attempt at the sample's heat capacity analysis focused on processing the data in the most transparent way possible. This was a priority because the scaling point in the last method proved to be very impactful on the final results. This was problematic because the selection of the scaling point was somewhat arbitrary, so a method for analysis which would avoided ambiguous choices was sought. The resulting method chose to ignore the samples' and substrates' expected difference in the phononic heat capacity. This change in analysis was justified by assuming the difference in the temperature-dependence of the phononic heat capacity to be negligibly small because the vast majority of the samples' mass was in the substrate. The final point is particularly relevant

Sample number	Sample Mass(mg)	Film Mass (μg)
28	33(1)	8.2(3)
29	33(1)	8.0(3)
30	34(1)	8.0(3)
31	32(1)	3.3(1)
34	32(1)	1.57(4)

Table 5.4: The sample masses and corresponding film masses of 28:Yb68nm(111), 29:Yb66nm(1$\bar{1}$0), 30:Yb68nm(100), 31:Yb28nm(111) and 34:Yb13nm(111).

because the magnitude of heat capacity is directly proportional to mass. For example, if the sample's mass was doubled then its heat capacity would also double.

The second method involved all of the previous steps in the heat capacity's analysis except the shifting of the scaled substrate data. From the perspective of the first method, this change would have meant that after the scaled substrate subtraction the remaining heat capacity would be comprised of the film's magnetic heat capacity and its phononic heat capacity. However, due to the new assumptions, the film's phononic heat capacity could be ignored. The sample masses and the film masses are displayed in Table 5.4. Another justification for not accounting for the film phononic heat capacity is that the contribution of the mass of the film to the total mass of the sample is smaller than the uncertainty of the total sample mass.

The specific heat divided by the temperature is plotted against the temperature for samples 29:Yb66nm(1$\bar{1}$0) and 30:Yb68nm(100) in Figure 5.9. Figure 5.9a and 5.9b display samples 29:Yb66nm(1$\bar{1}$0) and 30:Yb68nm(100) respectively. Two substrates from different batches were also plotted: YTO(110)15 and YTO(100)18. The substrate YTO(110)15 was used in the first analysis and has not been splined in this analysis to minimise the amount of processes performed on the data. The substrate YTO(100)18 comes from the same batch as the measured films. Before the substrate data could be subtracted from the sample data, it first had to be splined. The spline function was used to interpolate between the substrate heat capacity values and output values that corresponded to the sample temperature. Spline interpolation requires that each consecutive pair of points must be joined together by a cubic function that matches the slope of the previous and subsequent pair, which ensures that the splined function is continuous. The graphs in Figure 5.9 show the results from 2 perspectives. On the left hand side (blue) the data has been plotted in terms of Yb ions and on the right hand side (red) the data has been plotted in terms of Ti ions. The data for both perspectives has been

overlapped for easier viewing and to show that the only difference between the different perspectives is a scaling factor. The number of Yb ions in each film was used to calculate to Yb perspective for their correspondingly scaled substrates. This does not have any physical meaning because there are no Yb ions in the $Y_2Ti_2O_7$ substrates. The number of Yb ions was used as a scaling factor for the substrate data sets so that they could accurately be compared with the sample data. The Ti perspective used the same number of Ti ions for both the sample and substrate scaling. This was because the sample mass was used to calculate the number of Ti moles: the masses of the films were smaller than the uncertainty in the samples' masses. Unlike the Yb perspective, the Ti perspective has physical significance for both sample and substrate.

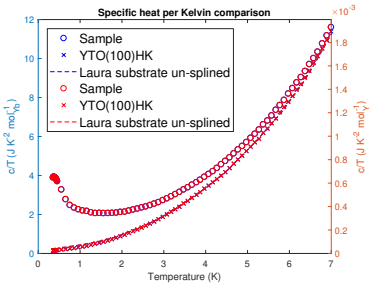

(a) The specific heat divided by the temperature of sample 29:Yb66nm($1\bar{1}0$) and its scaled substrates YTO(100)18 and YTO(110)15.

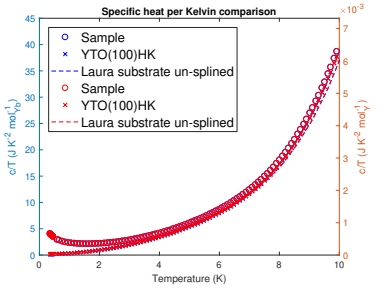

(b) The specific heat divided by the temperature of sample 30:Yb68nm(100) and its scaled substrates YTO(100)18 and YTO(110)15.

Figure 5.9: The specific heat divided by the temperature for the samples 29:Yb66nm($1\bar{1}0$) and 30:Yb68nm(100) along with their appropriately scaled substrates. The films of 29:Yb66nm($1\bar{1}0$) and 30:Yb68nm(100) are shown in (a) and (b) respectively. The left hand side (blue) y-axis corresponds to data that is given in per Yb ion. The right hand side (red) y-axis corresponds to data that is given in per Ti ion. The sample and substrates YTO(100)18 and YTO(110)15 are represented by circle, cross and dashed line markers respectively. The two sets of data have been deliberately overlapped so that each curve can be read on either y-axis.

The films' magnetic entropy was calculated slightly differently to the original method. Instead of first acquiring the film's magnetic specific heat divided by the temperature, the entropy was calculated for both the sample and the scaled substrate. The method used for calculating the entropy was the same method as that outlined previously. The entropy of the scaled substrate was subtracted from the sample's entropy giving the film's magnetic entropy. Entropy is an extensive property, so the subtraction of the substrate's contribution to the sample's entropy could have occurred at any point in this analysis. This method

was used to simplify the analysis and reduce any doubt of the validity of the result.

The main issue with this method is that, if the substrate is not shifted to match some part of the sample data, the resulting entropy can be unrealistic. This can be seen in Figure 5.10. Figure 5.10a displays the films' magnetic entropy per Yb ion for samples 29:Yb66nm($1\bar{1}0$) and 30:Yb68nm(100). The entropy data for sample 29:Yb66nm($1\bar{1}0$) has been truncated at the temperature where its total entropy began to decrease; a decreasing entropy with an increasing temperature is unphysical. Figure 5.10b provides a clearer view of the magnetic entropy of sample 28:Yb68nm(111) and its magnetic specific heat divided by the temperature. A black line has been plotted to intersect the entropy at the point where the entropy begins to decrease. Beyond the black line, the magnetic entropy has been set to be constant to its maximum value. As the temperature increases, the absolute uncertainty in the sample and substrate subtraction increases. This occurs because the uncertainty of a parameter scales with that parameter's increasing value. For instance, if two large similarly sized values with reasonably sized uncertainties are subtracted from each other then the original uncertainties of the large values may be comparable in size with the difference between the two values. Thus, the absolute uncertainty in the film's magnetic entropy at higher temperatures becomes so large that the data must be truncated to preserve its accuracy. In the case of Figure 5.10b, the truncation has been made when the entropy first began to decrease. Visually, Figure 5.10b displays a very clear relationship between the magnetic entropy and the magnetic specific heat divided by the temperature because the entropy flattens when the substrate and film values meet.

Another problem with this analysis is shown in Figure 5.10a where the entropy of sample 30:Yb68nm(100) does not plateau. This issue has arisen due to the substrate's magnetic specific heat divided by the temperature never intercepting the sample's. In the original method the substrate's magnetic specific heat divided by the temperature would have been shifted to guarantee that there was a point of interception. The original method also saw that samples 29:Yb66nm($1\bar{1}0$) and 30:Yb68nm(100) had similar maximum entropies. The trajectory of the two samples at low temperatures seems to be similar up to approximately 4 K. This implies that their magnetic entropy is similar, but due to their differences at higher temperatures it is likely that not all of their phonon contributions, which are more significant at higher temperatures, have been subtracted.

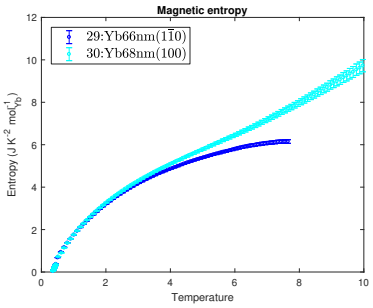

(a) The film magnetic entropy of samples 29:Yb66nm(1$\bar{1}$0) and 30:Yb68nm(100) either have been truncated or they never plateau; they are represented with dark blue circles and cyan circles respectively.

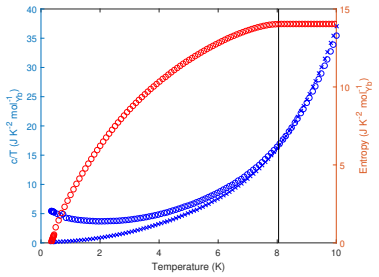

(b) The film's truncated magnetic entropy of sample 28:Yb68nm(111) is represented by the red circle markers. The black line indicates the point at which the film's magnetic entropy begins to decrease and beyond this line the data has been artificially flattened. Additionally, the sample's and substrate's specific heat divided by the temperature has been plotted to highlight their relationship with the entropy.

Figure 5.10: The issues that arose from the second attempt's method of analysis: negative entropy or entropy that never plateaus.

5.5 Investigation of thickness-dependence of the [111] out-of-plane $Yb_2Ti_2O_7$ films

An investigation into the thickness-dependence of films with the [111] out-of-plane crystallographic direction was carried out. Originally, the thickest films with different out-of-plane crystallographic directions were measured. The [111] direction displayed unexpected entropy and magnetic saturation values, which drew attention to this specific orientation. A thickness series of this film orientation was investigated to better understand the cause for its entropy and magnetic saturation values. The method described in the epitaxial strain series is the same for each corresponding section.

5.5.1 X-ray diffraction measurements

As mentioned previously, the objective of using XRD was to acquire the samples' thickness and determine if the films have been grown epitaxially. The thickness of samples 28:Yb68nm(111), 31:Yb28nm(111) and 34:Yb13nm(111) were obtained through the reflectivity measurements shown in Figure 5.11. These results are displayed in Table 5.1. To determine the lattice constant, specular scans were carried out around the 222 reflection for each sample. The

results are presented in Figure 5.12. Bragg's law was used to calculate the substrate and film lattice constants of the samples. The substrate and film lattice constants of sample 28:Yb68nm(111) were 10.076(6) Å and 9.93(5) Å respectively. The substrate lattice constant of sample 31:Yb28nm(111) was 10.10(3) Å, and for sample 34:Yb13nm(111) was 10.098(3) Å. For both samples 31:Yb28nm(111) and 34:Yb13nm(111), the film peaks intersected with their substrate peaks, which made acquiring their values and uncertainties more challenging. By averaging the distance between fringe peaks and troughs, the film lattice constants of 31:Yb28nm(111) and 34:Yb13nm(111) were determined to be 10.0(2) Å and 10(1) Å respectively. These results can be compared with the reported bulk values of $Y_2Ti_2O_7$ and $Yb_2Ti_2O_7$, which are given by 10.09 Å[37] and 10.1171(1) Å[25] respectively (NIMS crystal database gives 10.083 Åand 10.14 Å respectively and these were used in practice [38]). The lattice constants of the samples' substrates have not changed significantly from the bulk values. The film lattice constant of sample 28:Yb68nm(111) has noticeably shrunk. Due to the large uncertainties in the film lattice constants of 31:Yb28nm(111) and 34:Yb13nm(111), it is not clear if they have shrunk or remained similar to the bulk.

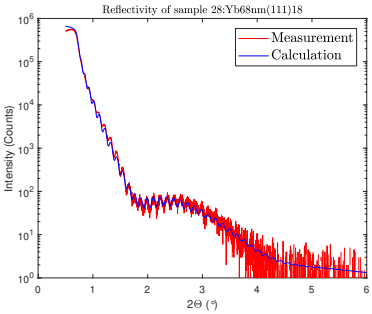

(a) Reflectivity of sample 28:Yb68nm(111).

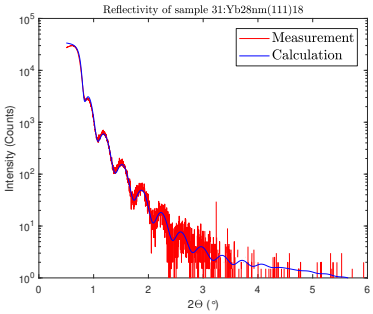

(b) Reflectivity of sample 31:Yb28nm(111).

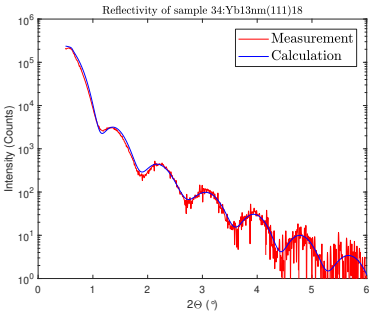

(c) Reflectivity of sample 34:Yb13nm(111).

Figure 5.11: The reflectivities of samples 28:Yb68nm(111), 31:Yb28nm(111) and 34:Yb13nm(111).

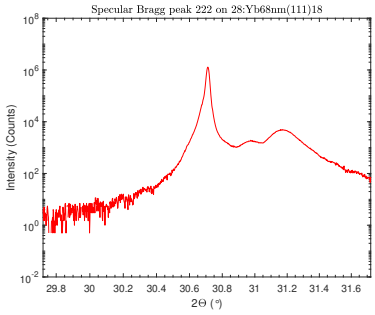

(a) Specular reflection of sample 28:Yb68nm(111).

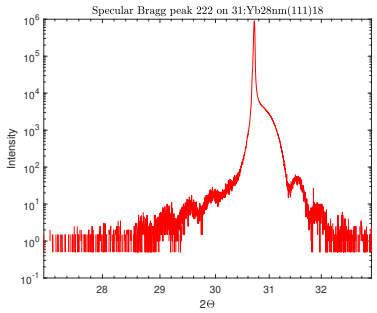

(b) Specular reflection of sample 31:Yb28nm(111).

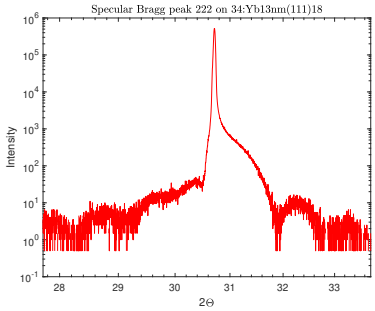

(c) Specular reflection of sample 34:Yb13nm(111).

Figure 5.12: The 222 specular reflection of samples 28:Yb68nm(111), 31:Yb28nm(111) and 34:Yb13nm(111).

Figure 5.13 displays RSMs around the 662 reflection for samples 28:Yb68nm(111), 31:Yb28nm(111) and 34:Yb13nm(111). In all cases there appears to be only one defined peak, which must be the substrate peak. In samples 28:Yb68nm(111) and 31:Yb28nm(111) there appears to be a region of slightly higher intensity just above the substrate peak. This region most likely represents the film and is consistent with a relaxed film. Figure 5.13c lacks this extra feature, but this is most likely because the film of 34:Yb13nm(111) is significantly thinner than the others and so its signal is below the detectable threshold.

All of the RSMs in this chapter are presented with axes that do not reflect the values stated in the text. This is due to a difference of basis. In the case of the [111] series, the basis shown reflects the in-plane crystal directions of the film. This is made more clear by the equations below:

$$\begin{bmatrix} 6 \\ 6 \\ 2 \end{bmatrix} = L \begin{bmatrix} -1 \\ -1 \\ 2 \end{bmatrix} + H \begin{bmatrix} 1 \\ 1 \\ 1 \end{bmatrix}$$

This gives $L \to -\frac{4}{3}$ and $H \to \frac{14}{3}$. The basis used in the RSM script assumed in-plane crystal directions equivalent to [001], [010] or [100] and so the film basis needed to be normalised to give the values displayed in the RSMs. This is shown below:

$$q = \begin{bmatrix} -\frac{4}{3} \\ \frac{14}{3} \end{bmatrix} \cdot \begin{bmatrix} \sqrt{6} \\ \sqrt{3} \end{bmatrix} = \begin{bmatrix} -4\sqrt{\frac{2}{3}} \\ \frac{14}{\sqrt{3}} \end{bmatrix}$$

The RSMs have not been modified for the [111] series because the original basis vectors are dependent on each other across multiple directions. This makes converting from one basis to another more challenging because there will be multiple solutions due to how intertwined the vectors are. As a result, the RSMs have been left in their original basis, but the origin of these values has been shown.

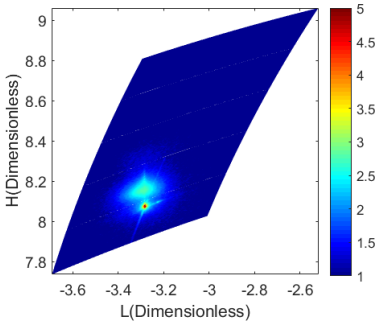

(a) RSM of 28:Yb68nm(111).

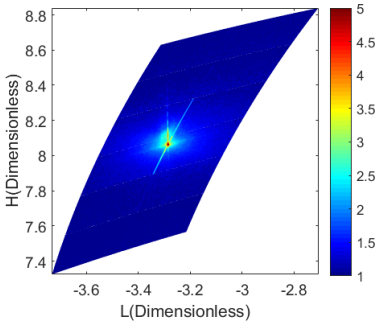

(b) RSM of 31:Yb28nm(111).

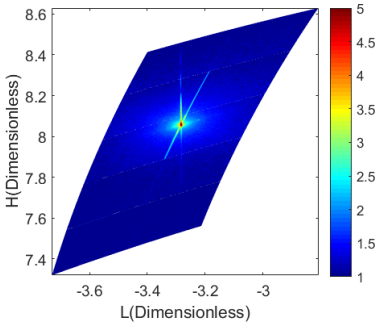

(c) RSM of 34:Yb13nm(111).

Figure 5.13: A RSM around the 662 reflection for the samples 28:Yb68nm(111), 31:Yb28nm(111) and 34:Yb13nm(111).

5.5.2 Magnetometry measurements

The method used to analyse and measure the magnetometry of the films 28:Yb68nm(111), 31:Yb28nm(111) and 34:Yb13nm(111) was the same as the method used for the films 29:Yb66nm($1\bar{1}0$) and 30:Yb68nm(100).

M vs H

Like the epitaxial series, both in-plane directions of the [111] samples were measured. Initially, the results were analysed via a substrate subtraction (explained earlier in the chapter) to obtain the film contribution. This resulted in unphysical results and so the fitting method was adopted. The results from the fitting are shown in Table 5.3.

Figure 5.13 displays the fitted data of samples 28:Yb68nm(111), 31:Yb28nm(111) and 34:Yb13nm(111) with applied fields along the in-plane directions. The magnetic moments obtained for sample 28:Yb68nm(111) along the directions [$\bar{1}\bar{1}2$] and [$1\bar{1}0$] were 4.8(2) μ_B(Yb^{3+} ion)$^{-1}$ and 4.8(2) μ_B(Yb^{3+} ion)$^{-1}$ respectively. Sample 31:Yb28nm(111) had a moment of 2.5(1) μ_B(Yb^{3+} ion)$^{-1}$ along [$\bar{1}\bar{1}2$] and 2.7(1) μ_B(Yb^{3+} ion)$^{-1}$ along [$1\bar{1}0$]. In the case of 34:Yb13nm(111), the fit produced uncertainties that were over 50 % of at least one of the fitting parameters and so the fit was considered to have failed; its section in Table 5.3 was left blank. The magnetic moments obtained are consistent between the [$\bar{1}\bar{1}2$] and [$1\bar{1}0$] direction, but vary between films. The magnetic moments that were successfully fit differ from the bulk value, ~ 3.25 μ_B(Yb^{3+} ion)$^{-1}$. One possible explanation for these findings could be that the interface of the films, which are not fully strained, could contribute an irregular signal because of their irregular structures. This could explain the different results between the films and bulk.

M vs T

The raw M vs T measurements for the samples 28:Yb68nm(111), 31:Yb28nm(111) and 34:Yb13nm(111) and their correspondingly scaled substrates are displayed in Figure 5.14. The most notable features are a high temperature moment and a FC and ZFC splitting for all samples and substrate. These are both features that are consistent with ferromagnetic impurities. The one exception to this is the sample data of 31:Yb28nm(111), which only has a high temperature moment. The splitting in the substrate FC and ZFC data would be expected to be replicated in the sample data, making this exception unusual.

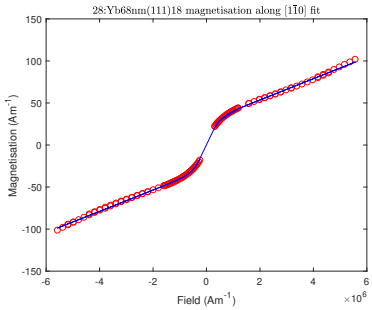

(a) M vs H of sample 28:Yb68nm(111) with an applied field along its [1$\bar{1}$0] direction.

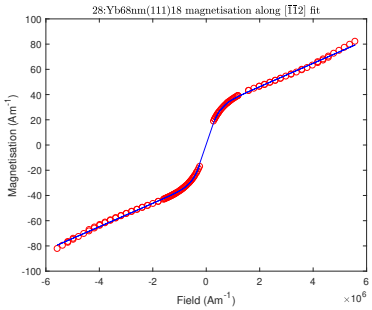

(b) M vs H of sample 28:Yb68nm(111) with an applied field along its [$\bar{1}\bar{1}$2] direction.

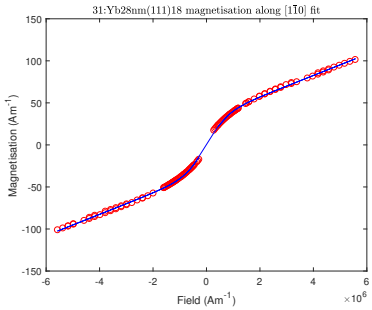

(c) M vs H of sample 31:Yb28nm(111) with an applied field along its [1$\bar{1}$0] direction.

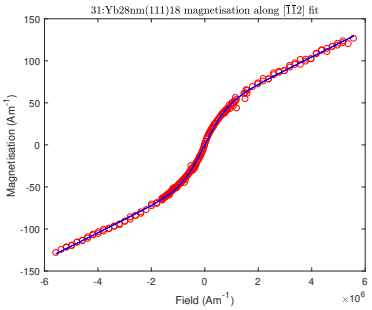

(d) M vs H of sample 31:Yb28nm(111) with an applied field along its [$\bar{1}\bar{1}$2] direction.

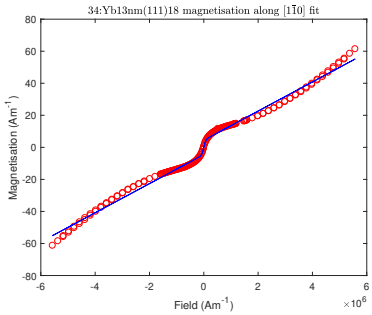

(e) M vs H of sample 34:Yb13nm(111) with an applied field along its [1$\bar{1}$0] direction.

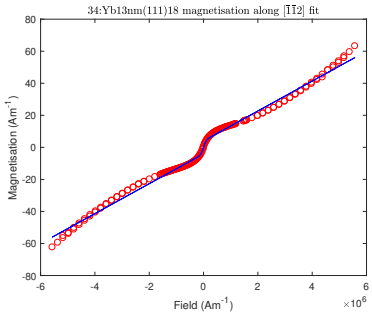

(f) M vs H of sample 34:Yb13nm(111) with an applied field along its [$\bar{1}\bar{1}$2] direction.

Figure 5.13: The fitted M vs H results of samples 28:Yb68nm(111), 31:Yb28nm(111) and 34:Yb13nm(111).

5.5.3 Specific heat measurements

Attempt 1

The different stages of the heat capacity analysis of samples 28:Yb68nm(111), 31:Yb28nm(111) and 34:Yb13nm(111) are displayed in Figure 5.15. The cir-

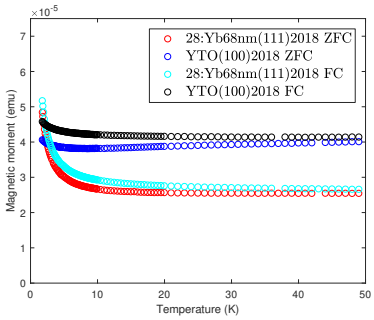

(a) M vs T of sample 28:Yb68nm(111) and its correspondingly scaled substrate.

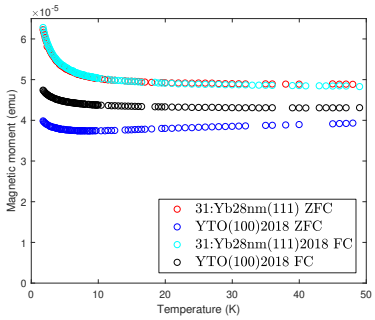

(b) M vs T of sample 31:Yb28nm(111) and its correspondingly scaled substrate.

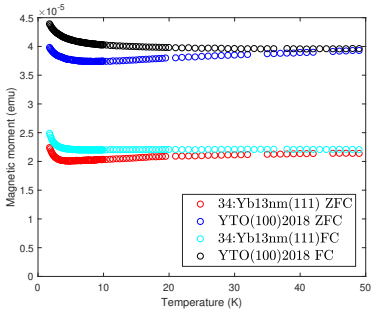

(c) M vs T of sample 34:Yb13nm(111) and its correspondingly scaled substrate.

Figure 5.14: M vs T (FC and ZFC) measurements of samples 28:Yb68nm(111), 31:Yb28nm(111) and 34:Yb13nm(111) and their correspondingly scaled substrates.

cle markers and lines represent the sample data and the scaled substrate data respectively. The results have been colour-coded such that red, magenta and black represent the samples 28:Yb68nm(111), 31:Yb28nm(111) and 34:Yb13nm(111) respectively. Figure 5.15a presents the heat capacity of the samples and their correspondingly scaled substrate. Figure 5.15b presents the film's magnetic heat capacity, which was obtained after subtracting the scaled substrate heat capacity from the sample heat capacity. Figure 5.15c displays the magnetic specific heat capacity divided by the temperature. The area under each curve in Figure 5.15c is equivalent to the samples' entropy, which is plotted in Figure 5.15d. Notable features throughout this analysis first appear in Figure 5.15b. Based purely on heat capacity magnitude, it would seem that the heat capacity of the films increases with increasing film thickness, which is expected. What is strange is that the film heat capacities of samples 31:Yb28nm(111) and 34:Yb13nm(111) are closer together than expected. This is assuming that the only difference between the films is their

thickness. The negative heat capacity of sample 34:Yb13nm(111) at higher temperatures can be explained by the absolute uncertainty in each measurement, which increases with the temperature (at high temperatures the magnetic heat capacity is very small and it is estimated by subtracting two increasingly large numbers). Figure 5.15d reveals that the reason why the magnetic heat capacity of the film 31:Yb28nm(111) was so close to 28:Yb68nm(111) was because it has a significantly larger magnetic entropy. All the films with a [111] out-of-plane crystallographic direction display a larger than normal magnetic entropy. The bulk entropy of $Yb_2Ti_2O_7$ is $R\ln(2)$. The expected values for the films' magnetic entropies to saturate at are either the Pauling entropy if spin ice rules apply or the film's bulk value. These are shown on Figure 5.15d by the bottom two dashed lines. The saturation value for the magnetic entropy of sample 34:Yb13nm(111) lies between the dashed lines representing $R\ln(3)$ and $R\ln(5)$. The saturation value for the magnetic entropy of sample 28:Yb68nm(111) lies between the dashed lines representing $R\ln(5)$ and $R\ln(6)$. The saturation value for sample 31:Yb28nm(111) is around the dashed line representing $R\ln(21)$. These entropy values are larger than expected and may be caused by the films relaxing. If their spins' anisotropy is weakened then they can point in more directions and thus have more microstates, which is directly related to entropy.

Attempt 2

The analysis in this section follows the same methodology as the second attempt analysis of the epitaxial series. The most notable difference being the lack of a substrate shift. Figure 5.16 displays the specific heat divided by the temperature for the samples 28:Yb68nm(111), 31:Yb28nm(111) and 34:Yb13nm(111) and their scaled substrates YTO(100)18 and YTO(110)15. There are two y-axes, which present the specific heat divided by the temperature in terms of (Yb ion)$^{-1}$ or (Ti ion)$^{-1}$. The data and the axes have been colour-coded to match so that it is clear which axes to use. To minimise cluttering, the graphs' axes have been scaled such that the data in both formats overlap. This shows that the only difference between the two ways of viewing the data is a scaling factor. The advantage of displaying the data in this way is that both the substrate and sample data can be read from an axis that has physical meaning. For example, the substrate data can be read from either axis, but since it does not contain any Yb ions this reading is only useful from an abstract perspective. Both sample and substrate can be read from the Ti axis, but given that the Ti^{+4} ions are non-magnetic it would be more logical to read the sample data from the Yb axis.

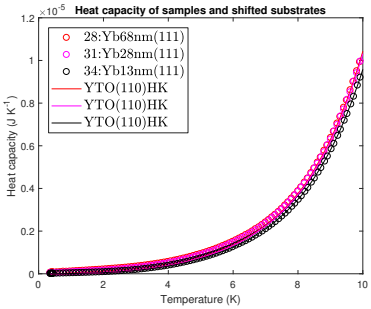

(a) The heat capacity results for the [111] samples (28:Yb68nm(111), 31:Yb28nm(111) and 34:Yb13nm(111)) and their correspondingly scaled and shifted substrates.

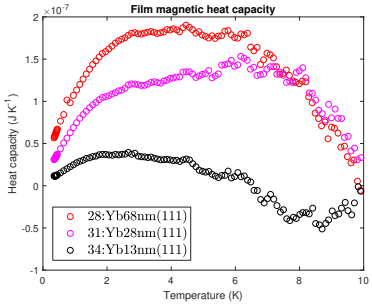

(b) The magnetic film heat capacities.

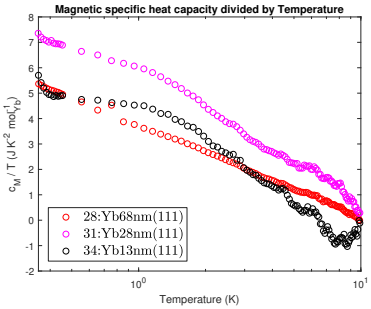

(c) The films' magnetic specific heat divided by the temperature.

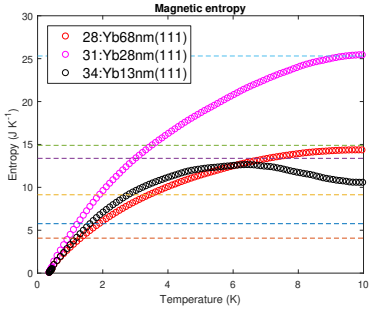

(d) The films' magnetic entropy. The red, blue, orange, black, green and blue dashed lines correspond to entropies of $\left(\frac{R}{2}\right)\ln\left(\frac{3}{2}\right)$, $R\ln(2)$, $R\ln(3)$, $R\ln(5)$, $R\ln(6)$ and $R\ln(21)$ respectively.

Figure 5.15: The different stages in the heat capacity analysis for the samples 28:Yb68nm(111), 31:Yb28nm(111) and 34:Yb13nm(111). The colours red, magenta and black represent the samples 28:Yb68nm(111), 31:Yb28nm(111) and 34:Yb13nm(111) respectively. In (a) the sample heat capacities are represented by the circles and the shifted substrate heat capacities are represented by the lines.

The original reason for trying this new method of analysis was to more transparently confirm if the entropies in the first analysis were correct. It can be seen that there is not a significant difference between the YTO(100)18 and YTO(110)15 substrate heat capacity responses. The magnetic film entropies in Figure 5.17 correspond to the area under the sample curve minus the area under the scaled substrate curve. At a glance, the film entropy area for sample 28:Yb68nm(111) could be approximated to be a triangle with a height of 6 and a width of 4. This gives an approximate entropy of 12.5 $\mathrm{JK}^{-1}(\mathrm{Yb\ ion})^{-1}$. The film entropy of sample 31:Yb28nm(111) could be approximated by a triangle

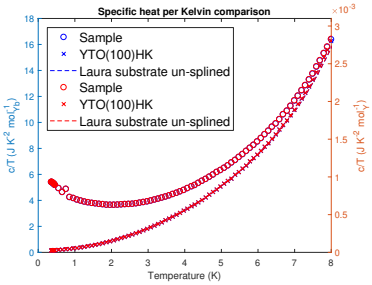

(a) The specific heat divided by the temperature results for sample 28:Yb68nm(111) and the correspondingly scaled substrates YTO(100)18 and YTO(110)15.

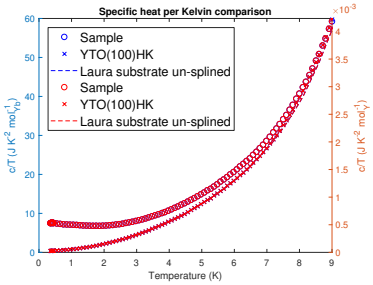

(b) The specific heat divided by the temperature results for sample 31:Yb28nm(111) and the correspondingly scaled substrates YTO(100)18 and YTO(110)15.

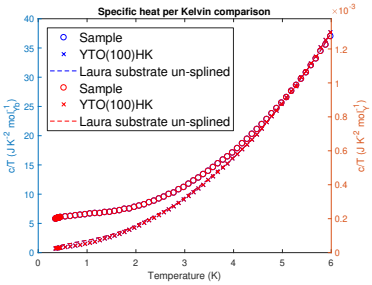

(c) The specific heat divided by the temperature results for sample 34:Yb13nm(111) and the correspondingly scaled substrates YTO(100)18 and YTO(110)15.

Figure 5.16: The specific heat divided by the temperature of samples 28:Yb68nm(111), 31:Yb28nm(111) and 34:Yb13nm(111) and their correspondingly scaled substrates YTO(100)18 and YTO(110)15. The left hand side (blue) y-axis corresponds to data that is given in per Yb ion. The right hand side (red) y-axis corresponds to data that is given in per Ti ion. The samples YTO(100)18 and YTO(110)15 are represented by circle, cross and dashed line markers respectively.

of height 8 and a width of 3. This would give an entropy of approximately 12 $JK^{-1}(\text{Yb ion})^{-1}$. The film entropy of sample 34:Yb13nm(111) could be approximated by a triangle of height 6 and a width of 3. This would give an entropy of approximately 9 $JK^{-1}(\text{Yb ion})^{-1}$.

The entropies in Figure 5.17 have been truncated at the point where the entropy begins to decrease with increasing temperature. This is unphysical and will be due to a slight mismatch between the sample and substrate phononic heat capacities. It is for these reasons that the entropies were truncated at different temperatures. It is possible to have a slight mismatch between the film and substrate phononic heat capacities such that the entropy is

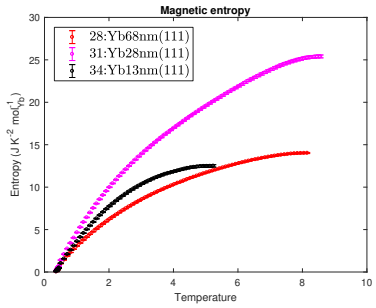

Figure 5.17: The truncated magnetic film entropy of samples 28:Yb68nm(111), 31:Yb28nm(111) and 34:Yb13nm(111).

increased. However, due to phononic heat capacity scaling approximately with T^3, a significant mismatch would quickly become obvious in the entropy. The saturation entropies of samples 28:Yb68nm(111), 31:Yb28nm(111) and 34:Yb13nm(111) are 14.0235 $JK^{-1}(Yb\ ion)^{-1}$, 25.4035 $JK^{-1}(Yb\ ion)^{-1}$ and 12.5071 $JK^{-1}(Yb\ ion)^{-1}$ respectively. These results are approximately what was predicted from Figure 5.16. These values are also similar to the values obtained in the first attempt, meaning it is likely that these entropies are real.

One of the main issues with the first attempt of analysis came from the unexpectedly large entropy values. Bulk $Yb_2Ti_2O_7$ measurements have an entropy of $R\ln(2) \approx 5.76\ JK^{-1}(Yb\ ion)^{-1}$ and so it was expected that the films would have an entropy close to this value. The entropy values obtained for the films with the [111] out-of-plane direction were significantly larger than this and prompted this second method to analysis. This more direct method of analysis has succeeded in improving the confidence in the large entropies obtained, which were originally doubted.

5.6 Batch 2019

The magnetometry measurements on the samples 28:Yb68nm(111), 29:Yb66nm($1\bar{1}0$), 30:Yb68nm(100), 31:Yb28nm(111) and 34:Yb13nm(111) imply that there are impurities in the substrate, which may have compromised the results. The epitaxial series displayed an entropy that was consistent with a ground state doublet and that of bulk $Yb_2Ti_2O_7$. The first attempt at analysing the M vs H measurements gave magnetic saturation values that were unusually large with features that suggested the presence of another magnetic signal. The second attempt at analysing the M vs H measurements gave results that were consistent with magnetic impurities. The M vs T results displayed a high temperature moment along with a ZFC and FC splitting, features that suggest ferromagnetic impurities are present in the samples. Both of these

features were also seen in the substrates, which implies that the substrates are the source of the impurities in the samples. The specific heat measurements from the thickness series produced unusually high entropies. The substrates used in the thickness and epitiaxial series were all cut from the same single crystal. This would suggest that the unusually high entropies seen in the thickness series are not due to impurities in the sample, but are a feature of the [111] out-of-plane crystallographic orientation of the films. It is for this reason that a $Yb_2Ti_2O_7$ film was grown on a substrate from a different batch with a [111] out-of-plane crystallographic direction. This sample will be referred to as 01:Yb28nm(111). At the time of growing this film, only the [111] heat capacity and magnetometry data had been analysed so it was not known that the previous [111] films had relaxed. It was hoped that 01:Yb28nm(111) would not display any signs of impurities in its magnetometry results while also showing the large magnetic entropy, which was seen in other [111] films.

5.6.1 X-ray diffraction and reflectivity

The reflectivity, a specular scan around the 222 reflection and a RSM around the 662 reflection are displayed in Figure 5.18. Unlike the previous films, a single film layer was fitted to the reflectivity of sample 01:Yb28nm(111) . This was because the fit matched the data well with only one layer. Additional layers could have been added, which would have visually improved the fit; but only because there would have been more parameters to fit. The thickness and density of this film layer were 28.345(12) nm and 6.810(5) g cm^{-3} respectively. The lattice constant of the substrate was calculated using Bragg's law to be 10.09(2) Å. The film peak overlapped with the substrate peak and so the average mid point between fringe peaks and troughs was measured. From this the $Yb_2Ti_2O_7$ lattice constant was calculated to be 10.0(2) Å. The RSM of 01:Yb28nm(111) reveals only one clearly defined peak, which should correspond to the substrate. The lack of a clearly defined film peak implies that the film is not fully strained. Potentially, some of the intensity surrounding the substrate peak could be from the relaxed film.

5.6.2 Magnetometry

The two different methods of analysing the M vs H results were carried out. The initial method, involving a substrate subtraction, gave unphysical results like the previous [111] films. As a result, only the fitted results are displayed. It was hoped that the M vs T results would show a lack of splitting between the

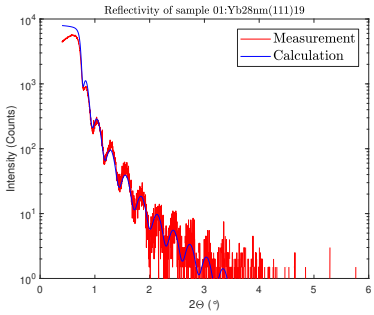

(a) Reflectivity of sample 01:Yb28nm(111).

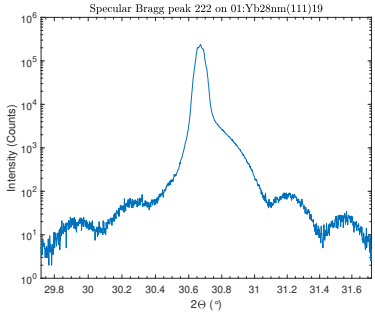

(b) Specular reflection of sample 01:Yb28nm(111).

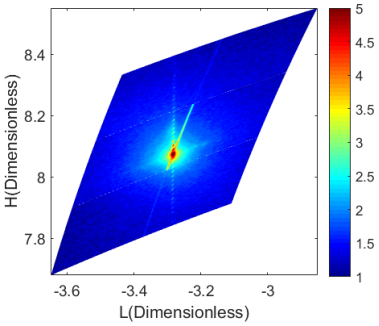

(c) RSM of sample 01:Yb28nm(111).

Figure 5.18: The reflectivity, the 222 specular reflection and a RSM around the 662 reflection of sample 01:Yb28nm(111).

ZFC and FC measurements and that there would not be a high temperature moment. These results would imply a lack of impurities inside of the sample.

M vs H

The fitted M vs H results of sample 01:Yb28nm(111) were left blank in Table 5.3 because in each of its fits there was an uncertainty that was over half of its corresponding value. Uncertainties this large imply that the fit is struggling to follow the data. The attempts to fit the model to the data are displayed in Figure 5.19. Both M vs H results for samples 34:Yb13nm(111) and 01:Yb28nm(111) display a curling at the ends of their signals, which may have contributed to the fits failing. This could indicate the presence of an additional magnetic source in these two samples.

M vs T

Figure 5.20 displays the raw M vs T data of sample 01:Yb28nm(111) and its scaled substrate for both FC and ZFC measurements. Both a high temperature moment and a splitting between FC and ZFC results is shown from the sample

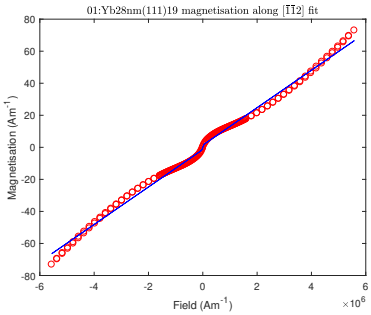

(a) Fitted M vs H results of sample 01:Yb28nm(111) with an applied field along its [$\bar{1}\bar{1}$2] direction.

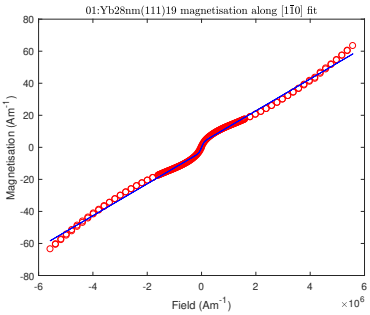

(b) Fitted M vs H results of sample 01:Yb28nm(111) with an applied field along its [1$\bar{1}$0] direction.

Figure 5.19: The fitted M vs H results of sample 01:Yb28nm(111).

and substrate data. This suggests that there are impurities in the substrate and sample's substrate.

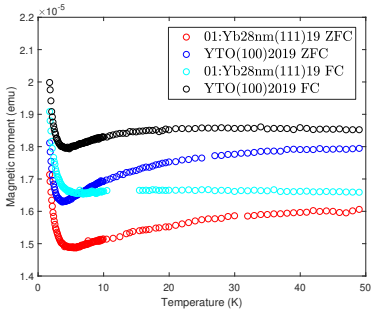

Figure 5.20: The M vs T (FC and ZFC) results of sample 01:Yb28nm(111).

5.6.3 Specific heat measurements

Figure 5.21a displays the raw heat capacity of sample 01:Yb28nm(111) and a correspondingly scaled substrate. Figure 5.21b presents the film entropy of sample 01:Yb28nm(111). The film magnetic entropy was obtained by using the second attempt's method (no shift of the substrate heat capacity). Both Figure 5.21a and 5.21b are displayed up to 3 kelvin because beyond 2 kelvin the sample and scaled substrate signals become too similar in magnitude. This results in the difference between the substrate and sample signals having too large of an absolute error. This is not a problem because the film's magnetic entropy appears to have been fully accessed by around 2 kelvin. The reported value for the film's bulk entropy is $R\ln(2)$ JK^{-1}(Yb ion)$^{-1}$. The measured film entropy plateaus at the Pauling entropy, which is close enough to the bulk entropy that the film's entropy could still be $R\ln(2)$.

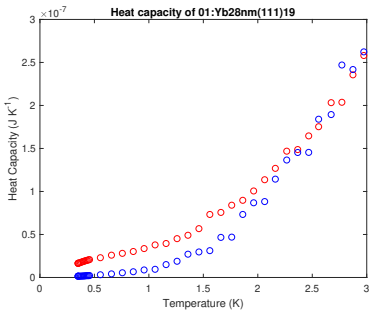

(a) Raw heat capacity of sample 01:Yb28nm(111) (red circles) and its correspondingly scaled substrate (blue circles).

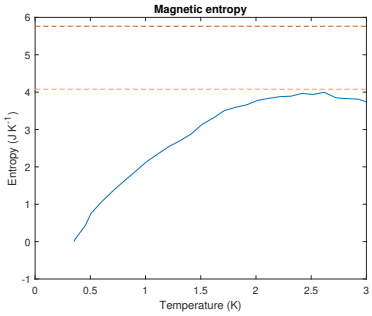

(b) Magnetic film entropy of sample 01:Yb28nm(111).

Figure 5.21: The raw heat capacity and film entropy of sample 01:Yb28nm(111). The red and orange dashed lines in (b) correspond to $R\ln(2)$ and $R\ln(2) - \left(\frac{R}{2}\right)\ln\left(\frac{3}{2}\right)$ respectively.

5.7 Summary

This summary can be broken down into three sections. First the epitaxial series produced X-ray results that are consistent with epitaxially grown thin films. The specific heat for these films matched the bulk $Yb_2Ti_2O_7$ entropy. The magnetometry revealed that these films have magnetic impurities in the substrate. These impurities are most likely ferromagnetic because the low temperature entropy does not appear to be inflated, which is consistent with ferromagnets in their ground state. The [111] thickness series produced films that do not appear to be fully strained. The entropy of these films is significantly larger than bulk $Yb_2Ti_2O_7$. The magnetometry implies that these films also have ferromagnetic impurities in their substrates. The X-ray results of 01:Yb28nm(111) revealed that its film had not grow epitaxially. The entropy of 01:Yb28nm(111) was close to the Pauling value, but this should be interpreted with caution. Its magnetometry showed that there are significant ferromagnetic impurities in this sample and the substrates of this batch. The impurities present in the samples are suspected to have come from the initial components of the $Y_2Ti_2O_7$ substrate. It is thought that the purest grade of Y_2O_3 may not have been used. In the future the purity of the substrates should be tested at all stages.

The decision was made to invest more time into the [111] series, but unfortunately the work did still not reach a firm conclusion. The additional [111] film, which was grown using a substrate from another batch, was grown prior to successful RSM measurements on any of the [111] samples. At that time, the unusual entropy of the [111] series had been measured, which prompted the

growth of a [111] film. Another attempt was made to go back to Oak Ridge National Lab to grow different films, but this was canceled due to Covid. Had time allowed, a thickness series on either the [100] or [$1\bar{1}0$] direction would have been carried out.

Chapter 6

Thick Films

6.1 Introduction

This chapter presents the results from heat capacity, magnetometry and X-ray experiments, which were carried out on a series of different titanate thin films, grown on $Y_2Ti_2O_7$ substrates. The thin films investigated are $Dy_2Ti_2O_7$, $Yb_2Ti_2O_7$ and $Tb_2Ti_2O_7$, with an out-of-plane crystal direction of [001] and a nominal thickness of 500 nm; this was estimated from the number of PLD laser pulses it took to grow the films. Using the same sample referencing nomenclature that was described in the $Yb_2Ti_2O_7$ chapter, the samples will be referred to as 07:Dy500nm(001)19, 16:Yb500nm(001)19 and 18:Tb500nm(001)19. These are the thickest films that have been grown on $Y_2Ti_2O_7$ substrates using these materials. The epitaxial strain in thin films increases with film thickness – so how these thick films respond to this increased strain will be of interest.

6.1.1 Differences in analysis between thick films and the $Yb_2Ti_2O_7$ chapter

The difference in thickness between films presented in this chapter and the other results' chapters is significant enough to justify some modifications or extensions to their analysis. In the previous $Yb_2Ti_2O_7$ chapter, XRD was performed with two objectives in mind: to determine the thickness of the film and to verify if the film was fully strained. The film thickness was previously obtained through a reflectivity fit, which derived its estimate from oscillations in the reflectivity results. The frequency of oscillations is proportional to the film thickness. An accurate estimate of the thick films using this method is not possible because the reflectivity oscillations are so frequent that they are indistinguishable from the background noise. An alternative method for determining the film thickness uses the specular reflection's oscillation width,

but this suffers from the same issue as the reflectivity. As a result, the analysis of these films uses their nominal thickness of 500 nm and their reported bulk densities on the NIMS crystal database. The RSMs that are presented in this chapter have been divided by $\sqrt{2}$ along the x-axis. This gives the correct Miller indices for the RSMs. The methodology outlined in *First attempt of analysis* (Chapter 5) was used in the heat capacity analysis of the thick films. However, instead of choosing to shift the substrate heat capacity to a fixed point, it was shifted to avoid a negative entropy. This should not be present in any analysis as it is unphysical. The advantage of shifting the substrate heat capacity to a fixed point was that the change between samples in a series could be followed without differences in the analysis playing a role. Since this chapter does not present a series of films, there is no advantage to fixing the scaling point. The M vs H magnetometry results were analysed and were fitted using the methodology discussed in Chapter 5. Equation 6.1 was used in the fitting.

$$M = \chi_{\mathrm{VV}} H + \tilde{\mu}\tilde{n}c_1 \tanh\left(\frac{c_2\tilde{\mu}H}{T}\right) \tag{6.1}$$

Where χ_{VV} is the Van Vleck (VV) susceptibilty, H is the applied field, $\tilde{\mu}$ is the magnetic moment, $\tilde{n}$ is the proportion of the sample that is made up of magnetic ions (impurities or impurities plus film ions), T is the sample temperature and both c_1 and c_2 are constants, 1.44×10^5 and 8.44×10^{-7} respectively. The derivation of equation 6.1 is given in Appendix B.

The analysis of the M vs T data in Chapter 5 was cut short due to the significant number of impurities in the substrate, which prevented the film susceptibility from being accurately determined. Due to the thicker films having more mass and different rare-earth ions, which have a larger magnetic moment, the proportionate effect from the impurities in the substrate is comparatively weaker. The susceptibility was calculated using equation 6.2.

$$\chi = \frac{\left(\frac{\mu\tilde{m}\mu_0}{m_{\mathrm{Film}}\tilde{v}} - \mu_0 M_{\mathrm{VV}}\right)}{B} \tag{6.2}$$

Where μ is the raw magnetic moment, $\tilde{m}$ is the mass per ion, m_{Film} is the film mass, $\tilde{v}$ is the volume per ion, M_{VV} is the Van Vleck magnetisation and B is the applied field. The Van Vleck magnetisation was determined via the M vs H fit. The inverse susceptibility was then plotted and fitted using equation 6.3.

$$\frac{1}{\chi} = (a \times T) + b \tag{6.3}$$

Where T is the sample temperature, a and b are fitting parameters given by $\frac{1}{C}$ and $\frac{-\theta_{CW}}{C}$ respectively. Both bulk and previous thin films of $Dy_2Ti_2O_7$ exhibited a Curie crossover. For this reason, the analysis of the thick $Dy_2Ti_2O_7$ film will include $\frac{\chi T}{C}$ plotted against the temperature.

6.2 $Dy_2Ti_2O_7$

6.2.1 XRD

Figure 6.1 (a) and (b) display the 400 specular reflection and the 662 RSM respectively. The specular reflection was used with Bragg's law to calculate the lattice constants of the substrate and film, $Y_2Ti_2O_7$ and $Dy_2Ti_2O_7$: 10.10(2) Å and 10.15(2) Å respectively. Their corresponding bulk values are 10.083 Å and 10.136 Å, which are within each value's experimental uncertainty. This implies that the substrate retains its cubic structure. This was expected because the bulk substrate and film lattice constants are very similar, and the substrate is significantly larger than the film. The experimental results of both the film and substrate are within uncertainty of each other (roughly 2.5 errorbars) and so may have the same value. In Figure 6.1b both the film and substrate peaks have the same in-plane value, which is consistent with a fully-strained film. The substrate peak has a higher H value than the film peak. Together these results suggest that the film either expands along or retains its bulk out-of-plane lattice constant and is compressed along its in-plane directions.

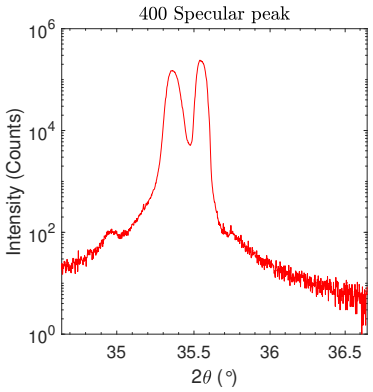

(a) 400 specular scan.

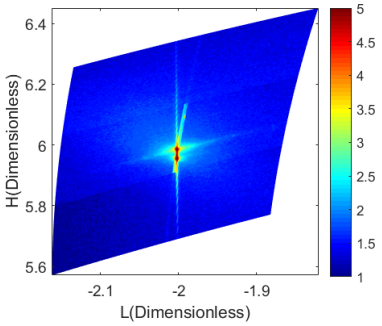

(b) 662 RSM.

Figure 6.1: The 400 specular reflection and a RSM around the 662 reflection for sample 07:Dy500nm(001)19.

6.2.2 Magnetometry

Figure 6.2 displays the fitted M vs H and raw FC and ZFC M vs T results of sample 07:Dy500nm(001)19. The values obtained were $\chi_{VV} = 3.8(2) \times 10^{-6}\ Am^{-1}$, $\tilde{\mu} = 9.4(1)\ \mu_B$ and $\tilde{n} = 7.6(1) \times 10^{-5}$. The magnetic moment is within uncertainty (2.5 errorbars) of the reported bulk magnetic moment, 9.590(6) $\mu_B(Dy^{3+}\ \text{ion})^{-1}$ [25]. Chapter 5 showed that substrate impurities in sample 01:Yb28nm(111) compromised the susceptibility of FC and ZFC measurements by introducing a splitting effect. This effect is significantly reduced in sample 07:Dy500nm(001)19, despite using a substrate from the same batch. This comes down to 07:Dy500nm(001)19 having a larger total film magnetic moment, which arises from a thicker film and different rare-earth ions that have larger moments.

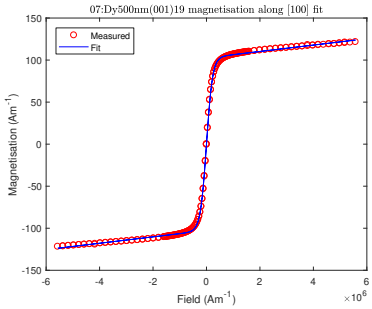

(a) Fitted M vs H data.

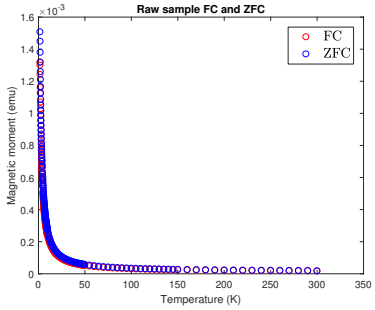

(b) Raw M vs T (FC and ZFC).

Figure 6.2: The fitted M vs H and raw M vs T (FC and ZFC) results of sample 07:Dy500nm(001)19.

Both the FC and ZFC inverse susceptibilities are plotted and fitted against temperature in Figure 6.3 (a) and (b). The values extracted from the FC results were 3.54(1) kelvin, 0.36(3) kelvin and 10.85(2) for the Curie constant, the Curie-Wiess temperature and the g_{eff} respectively. The ZFC Curie constant, Curie-Wiess temperature and g_{eff} were 4.03(2) kelvin, 0.38(4) kelvin and 11.57(3) respectively. The reported $Dy_2Ti_2O_7$ film's Curie constant and Curie-Weiss temperature were 4.25(5) kelvin and 1.1(1) kelvin respectively [4]. There is a small difference between the FC and ZFC Curie constants and Curie-Wiess temperatures, with the ZFC values being slightly closer to the reported film values. The susceptibility multiplied by the temperature and divided by the Curie constant is plotted in Figure 6.3 (c) and (d). The insets provide a zoomed out view of the plot. Figure 6.3 (a) and (b) have shown that the inverse susceptibility is linearly-dependent on temperature and so the non-linear behaviour in Figure 6.3 (c) and (d) arises from a change in the Curie

constant. The FC and ZFC Curie crossover is smaller than the reported bulk and thin films, which changed by $\approx 1.4C$ and $\approx 1.2C$ respectively.

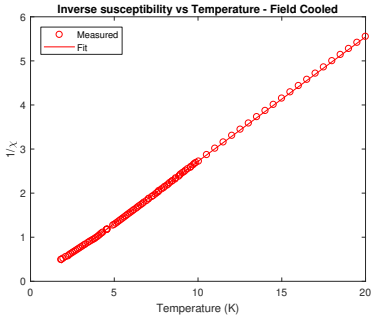

(a) FC inverse susceptibility vs temperature.

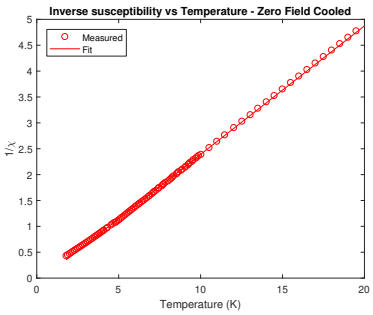

(b) ZFC inverse susceptibility vs temperature.

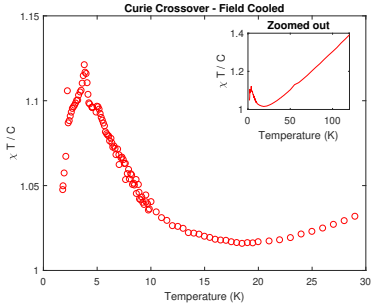

(c) FC Curie crossover.

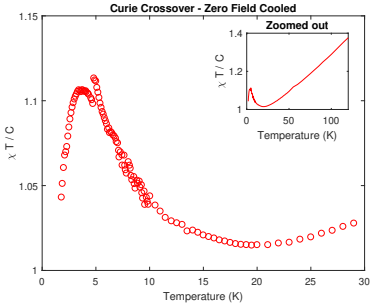

(d) ZFC Curie crossover.

Figure 6.3: The inverse susceptibility vs temperature and the $\chi T/C$ vs Temperature of sample 07:Dy500nm(001)19 for both FC and ZFC procedures.

6.2.3 Heat capacity

Figure 6.4 presents the heat capacity of sample 07:Dy500nm(001)19 and its stages of analysis. These stages are: the sample heat capacity plotted with the scaled substrate (a), the film heat capacity (b), the film specific heat divided by the temperature (c) and finally the film's magnetic entropy (d). The substrate heat capacity was scaled to its point at 7.3291 K. The three dashed lines plotted in (d) represent the Pauling entropy (red), square-ice entropy (green) and $R\ln(2)$ (blue). The entropy plateaus around the square-ice entropy, which is predicted by Jaubert *et al.* along with a surface-ordering transition [23]. This remains only a possible explanation for the film's entropy, but it is clear that more entropy than the Pauling entropy is accessed.

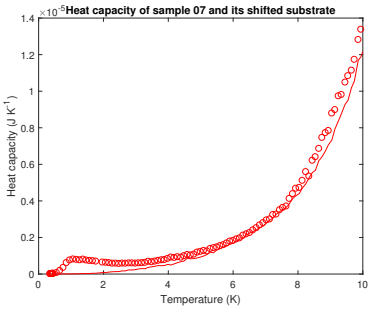

(a) The sample's heat capacity and its scaled substrate heat capacity.

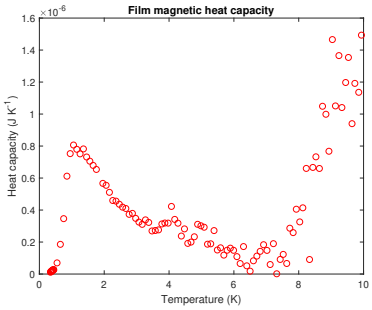

(b) The film's magnetic heat capacity.

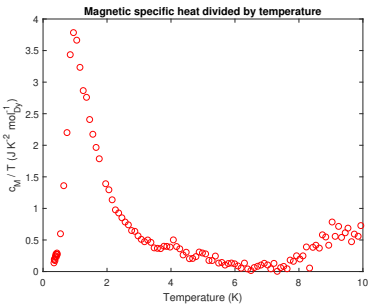

(c) The film's magnetic specific heat divided by the temperature.

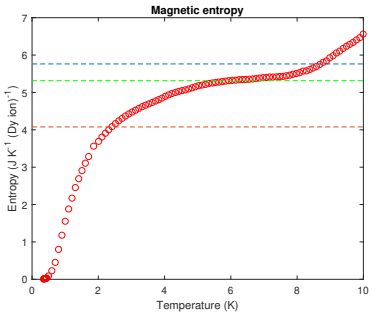

(d) The film's magnetic entropy.

Figure 6.4: The different stages in the heat capacity analysis for sample 07:Dy500nm(001)19. The red circles and the red line in (a) correspond to the sample data and its scaled substrate heat capacity respectively. The red, green and blue dashed lines in (d) correspond to $R\ln(2) - \left(\frac{R}{2}\right)\ln\left(\frac{3}{2}\right)$, $\frac{1}{4}\left(\frac{3}{4}\ln\left(\frac{4}{3}\right)\right)$ and $R\ln(2)$ respectively.

6.3 $Yb_2Ti_2O_7$

6.3.1 XRD

The specular scan of the 400 reflection and the 662 RSM of sample 16:Yb500nm(001)19 are displayed in Figure 6.5. The 400 specular reflection has two film peaks instead of the expected one. The lattice constants were obtained: 10.073(6) Å for the $Y_2Ti_2O_7$ peak, 10.02(2) Å and 9.99(2) Å for both of the $Yb_2Ti_2O_7$ peaks. The bulk values are 10.083 Å and 10.14 Å respectively. The FWHMs of both $Yb_2Ti_2O_7$ peaks are unclear due to intensity contributions from neighbouring peaks, which obscure half of each peak. As a result, only half of the FWHM was calculated. This was used to approximate the FWHM because the peaks should be symmetrical. In other results sections, the FWHMs have been used as a measure of uncertainty in conjunction with the rule of 2.5 error bars to verify if the results are truly

separate from each other. This rule actually only applies to random uncertainties, which the FWHM is not. Therefore, it is not appropriate to use this rule when there are conflicting results to distinguish the number of phases. The RSM produces results that are consistent with a fully strained film because the x-axis values for both the $Yb_2Ti_2O_7$ and $Y_2Ti_2O_7$ peaks are the same. The lowest H value peak represents the $Y_2Ti_2O_7$ substrate. The unique aspect of this sample is its two fully strained phases of $Yb_2Ti_2O_7$. The structural difference between these two phases is along the direction of growth. The departure from a single crystal film was a possible outcome, but how this film has departed from a single crystal state is surprising because the expected path was through the relaxation of the film. If the film had relaxed along the y-axis then the RSM would display a vertical streak; instead there are two defined points. The majority of the rare-earth titanates' unit cells are made up of oxygen. An explanation for these different phases of $Yb_2Ti_2O_7$ is that they have different proportions of oxygen, which cause their lattice constants to be different sizes. Both film phases' crystal structures have been compressed along their in-plane directions and compressed by differing amounts along their out-of-plane direction.

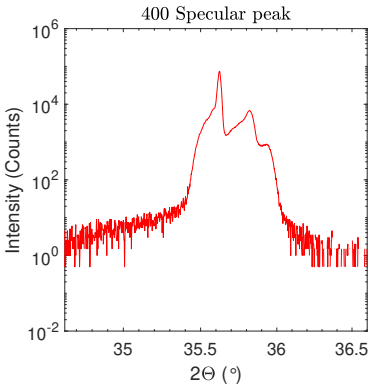

(a) 400 Specular scan.

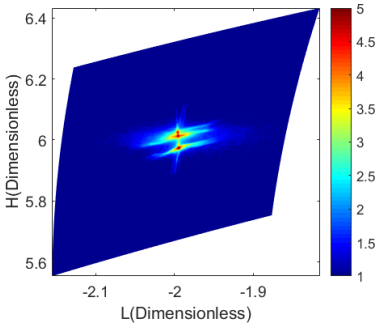

(b) 662 RSM.

Figure 6.5: The 400 specular reflection and a RSM around the 662 refection of sample 16:Yb500nm(001)19.

6.3.2 Magnetometry

Figure 6.6 displays the fitted M vs H results (a), the raw FC and ZFC results (b), the FC inverse susceptibility vs temperature (c) and the ZFC inverse susceptibility vs temperature (d) of sample 16:Yb500nm(001)19. The values outputted from the M vs H fitting: $\chi_{VV} = 4.7(2) \times 10^{-6}\ Am^{-1}$, $\tilde{\mu} = 2.18(4)\ \mu_B(Yb^{3+}\ \text{ion})^{-1}$ and $\tilde{n} = 1.51(5) \times 10^{-4}$. A systematic study on the stoichiometry of bulk $Yb_2Ti_2O_7$ by Arpino *et al.* [29] reports that its effective

magnetic moment is approximately 3.171(8) $\mu_B(Yb^{3+}\text{ ion})^{-1}$. The bulk values given by [25] are $\theta_{CW} = 0.59(1)$ kelvin and $\mu = 3.335(4)$ μ_B. The difference between the film and these bulk moments is thought to arise from its double phase and anisotropy, though the affect of the former is not clear. The film's magnetic moment is close to, 2.309 μ_B, the theoretical maximum measurable magnetic moment of $Yb_2Ti_2O_7$ assuming it has Ising spins along its local [111] direction. This implies the film has strong anisotropy. The calculation for this is shown in Appendix A. However, it is likely that this is a coincidence because bulk $Yb_2Ti_2O_7$ has x-y spins instead of Ising spins.

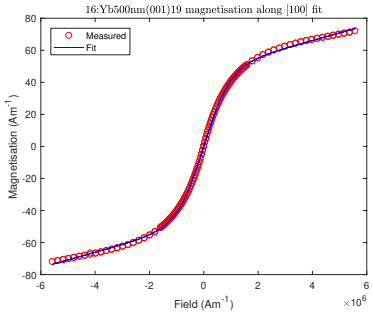

(a) Fitted M vs H data.

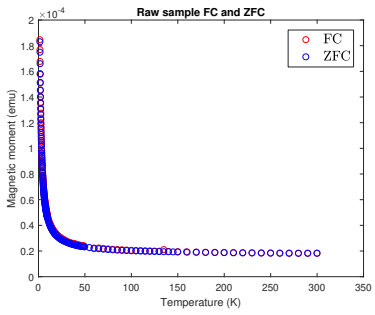

(b) Raw M vs T (FC and ZFC).

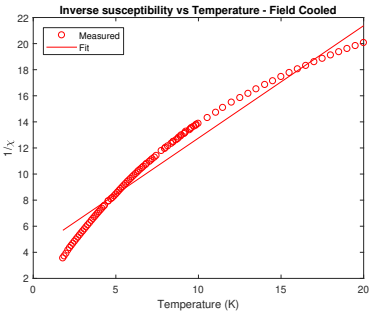

(c) FC inverse susceptibility vs temperature.

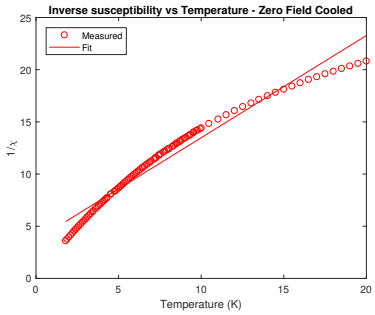

(d) ZFC inverse susceptibility vs temperature.

Figure 6.6: The M vs H, raw M vs T (FC and ZFC) and both FC and ZFC inverse susceptibility vs temperature of sample 16:Yb500nm(001)19.

The raw M vs T results show only a small splitting and a similar sized moment at high temperature to sample 07:Dy500nm(001)19. The Van Vleck extracted from the M vs H was used to fit the inverse susceptibility in the range of 1.8 kelvin to 20 kelvin for both the FC and ZFC results. The values from the FC results are $C = 1.16(5)$ kelvin, $\theta_{CW} = -4.8(5)$ kelvin and $g_{eff} = 6.2(1)$. The values obtained from the ZFC results are $C = 1.02(4)$ kelvin, $\theta_{CW} = -3.8(4)$ kelvin and $g_{eff} = 5.8(1)$. It is clear from the graphs that the inverse susceptibility is not linearly-dependent on temperature. The Van Vleck was varied in an attempt to achieve a linear temperature-dependence, but this

was not successful. As a result, the values obtained from the M vs T fits are not reliable.

6.3.3 Heat capacity

Figure 6.7 (a), (b), (c) and (d) display the sample (07:Dy500nm(001)19) and its scaled substrate heat capacity, the film's magnetic heat capacity, the film's magnetic specific heat divided by the temperature and the film's magnetic entropy respectively. The substrate heat capacity was scaled to ~ 24 K. Figure 6.8 displays the film entropy when the scaling point was shifted to ~ 18 K. At no point does the low temperature entropy drop for either of the scalings. In both cases the entropy accessed is above the Pauling entropy, but it is below the expected $R\ln(2)$ of the bulk.

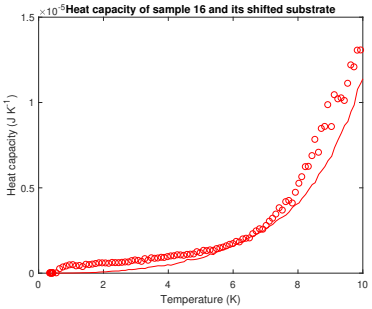

(a) The sample's heat capacity and its substrate heat capacity, which was scaled to a point at ≈ 24 K.

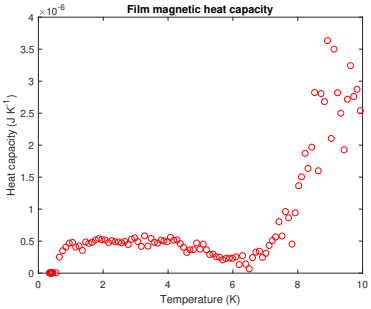

(b) The film's magnetic heat capacity.

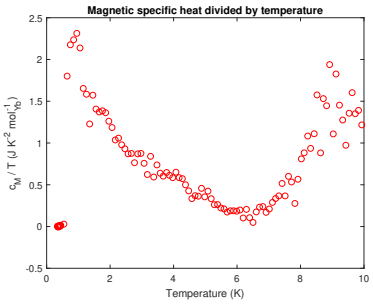

(c) The film's magnetic specific heat divided by the sample temperature.

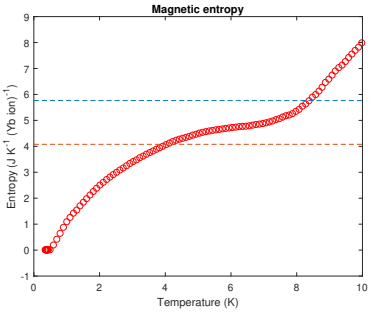

(d) The film's magnetic entropy.

Figure 6.7: The different stages of analysis for the heat capacity results of sample 16:Yb500nm(001)19 (with a scaling point at ~ 24 K). The red circles and the red line in (a) correspond to the sample data and its scaled substrate heat capacity respectively. The red and blue dashed lines in (d) correspond to $R\ln(2) - \left(\frac{R}{2}\right)\ln\left(\frac{3}{2}\right)$ and $R\ln(2)$ respectively.

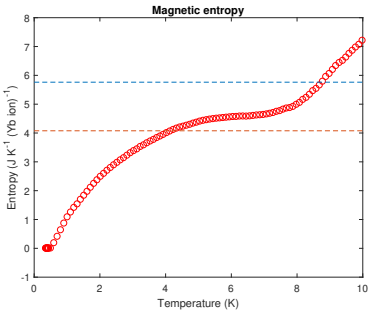

Figure 6.8: An alternative film magnetic entropy for sample 16:Yb500nm(001)19. This entropy was achieved by scaling the substrate heat capacity to a point at ≈ 18 K. The red and blue dashed lines in (d) correspond to $R\ln(2) - \left(\frac{R}{2}\right)\ln\left(\frac{3}{2}\right)$ and $R\ln(2)$ respectively.

6.4 $Tb_2Ti_2O_7$

6.4.1 XRD

Figure 6.9 displays both the 400 specular reflection and the 662 RSM of sample 18:Tb500nm(001)19. The lattice constants of its $Y_2Ti_2O_7$ substrate and $Tb_2Ti_2O_7$ film are 10.076(7) Å and 10.19(3) Å respectively. When comparing their bulk values, 10.083 Å and 10.115 Å respectively, the reported value for the substrate is within the sample's uncertainty, but the bulk $Tb_2Ti_2O_7$ lattice constant is not within its uncertainty (roughly 2.5 errorbars). The RSM around the 662 reflection also has three peaks, but it differs from sample 16:Yb500nm(001)19 in a number of ways. The most striking difference is that both the bottom and top peak relax, which is indicated by their streaks. The middle peak, representing the $Y_2Ti_2O_7$ substrate, does not have any streaks, which suggests it consists of a single phase. A locus drawn as a black dashed line over the RSM represents cubic systems; both in-plane and out-of-plane lattice constants are the same size. Along this dashed line there are red and cyan solid lines, which represent a range of reported off-stoichometric $Y_2Ti_2O_7$ and $Tb_2Ti_2O_7$ values respectively. The cyan asterisk marks where it is suspected that the $Tb_2Ti_2O_7$ film began growing epitaxially. From this point it is expected that the film began relaxing towards the cubic line, represented by the cyan dashed line. For comparison, the bulk values provided by the NIMS crystal database are displayed by the cyan and red pluses for $Tb_2Ti_2O_7$ and $Y_2Ti_2O_7$ respectively. From this it appears that the film begins growing fully strained, but the increased epitaxial strain on the film as it grows thicker causes its in-plane lattice constants to relax (expand) towards the cubic line.

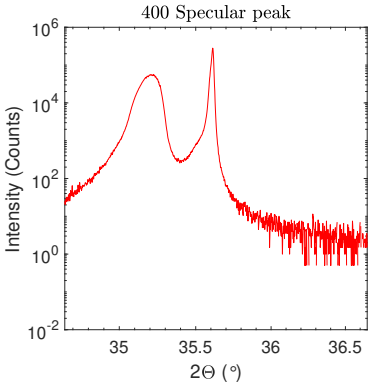

(a) 400 specular scan.

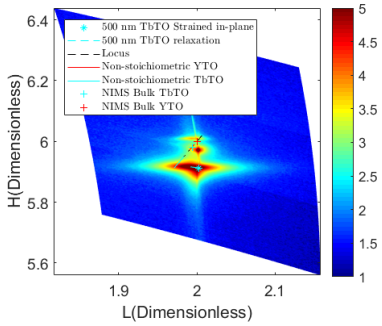

(b) 662 RSM.

Figure 6.9: The 400 specular reflection and a RSM around the 662 reflection of sample 18:Tb500nm(001)19. A locus representing cubic systems has been plotted in (b) with parts of it coloured to represent where $Y_2Ti_2O_7$ (red) and $Tb_2Ti_2O_7$ (light blue) could lie.

6.4.2 Magnetometry

The M vs H, the raw M vs T FC and ZFC, the FC inverse susceptibility vs temperature and the ZFC inverse susceptibility vs temperature of sample 18:Tb500nm(001)19 are displayed in Figure 6.10. The fitted M vs H values are $\chi_{VV} = 1.60(2) \times 10^{-5}$ A m^{-1}, $\tilde{\mu} = 3.77(5)$ μ_B and $\tilde{n} = 1.65(3) \times 10^{-4}$. The reported bulk values for the Curie-Weiss temperature and magnetic moment are ≈ -19 kelvin and 9.6 μ_B(Tb^{3+} ion)$^{-1}$ [39]. There is a significant difference between the film and bulk magnetic moments.

The raw M vs T FC and ZFC results do not appear to have significant splitting. It has been reported that the bulk inverse susceptibility is linearly-dependent at high temperatures, but begins to depart from the Curie law at ~ 70 kelvin [39]. A linear fit was attempted from 150 kelvin to 250 kelvin. The values obtained from the FC fit are $C = 15.1(7)$ kelvin, $\theta_{CW} = -2.0(1) \times 10^2$ kelvin and $g_{eff} = 22.3(5)$. The values obtained from the ZFC fit are $C = 15.3(7)$ kelvin, $\theta_{CW} = -2.1(1) \times 10^2$ kelvin and $g_{eff} = 22.5(5)$. These values are not reliable because the films do not display a linear temperature-dependence. The Van Vleck obtained using the M vs H results was used in the fitting, but due to a poor fit the Van Vleck was varied in an attempt to make the results linear with temperature, but to no avail.

6.4.3 Heat capacity

Figure 6.11 (a) presents the sample heat capacity and the scaled substrate heat capacity, which was scaled to the sample point at ≈ 9.9 K. Figure 6.11 (b), (c) and (d) present the film's magnetic heat capacity, the film's magnetic specific

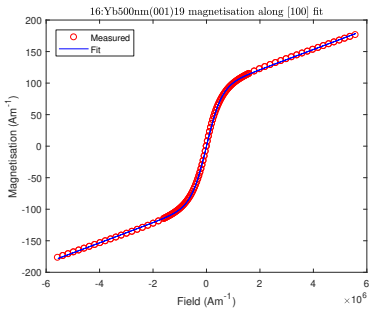

(a) Fitted M vs H data.

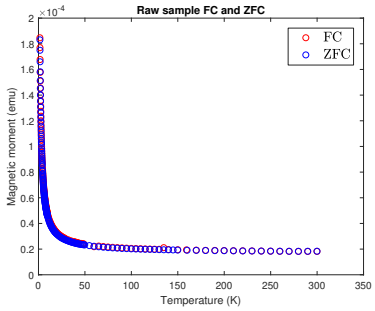

(b) Raw M vs T (FC and ZFC).

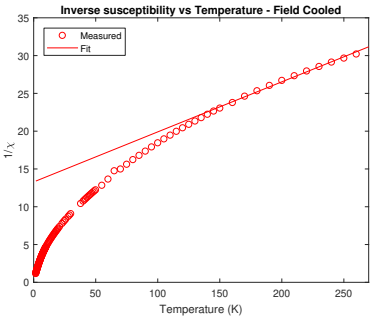

(c) FC inverse susceptibility vs temperature.

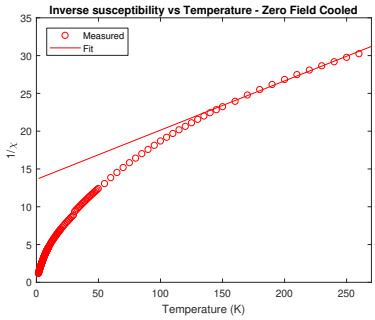

(d) ZFC inverse susceptibility vs temperature.

Figure 6.10: The fitted M vs H, raw M vs T (FC and ZFC) and both the FC and ZFC inverse susceptibility vs Temperature of sample 18:Tb500nm(001)19.

heat divided by the temperature and the film's magnetic entropy respectively. The reported bulk entropy of $Tb_2Ti_2O_7$ is larger than its two counterparts at $R\ln(4)$ J K^{-1} (Tb^{3+} ion)$^{-1}$. This additional entropy comes from a nearby excited state. The complete realisation of this entropy was not successful in the film as its entropy lies between the orange and blue dashed lines (Figure 6.11 (d)), which represent the entropies $R\ln(3)$ J K^{-1} (Tb^{3+} ion)$^{-1}$ and $R\ln(2)$ J K^{-1} (Tb^{3+} ion)$^{-1}$ respectively. A possible explanation for why the film entropy is smaller than its bulk entropy is that the measuring window is too small, such that it does not access higher temperatures where more of the first excited state's entropy could be accessed. Due to absolute uncertainties increasing in size as the temperature increases, the values above $\approx 6-7$ kelvin are not reliable.

6.5 Summary

To summarise, sample 07:Dy500nm(001)19 appears to have a fully strained film. When compared with bulk $Dy_2Ti_2O_7$, the film's lattice constants are compressed along its in-plane directions and are retained or expanded along

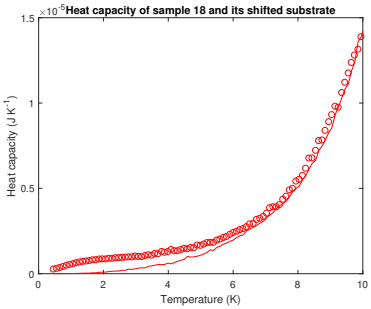

(a) The sample's heat capacity and its scaled substrate heat capacity.

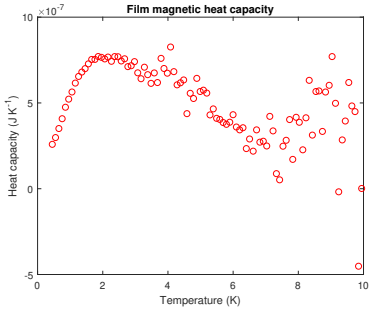

(b) The film's magnetic heat capacity.

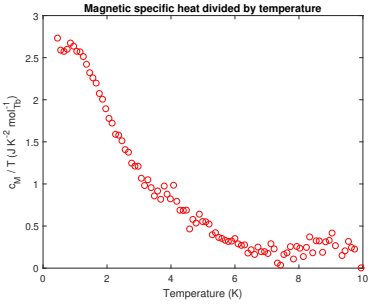

(c) The film's magnetic specific heat divided by the temperature.

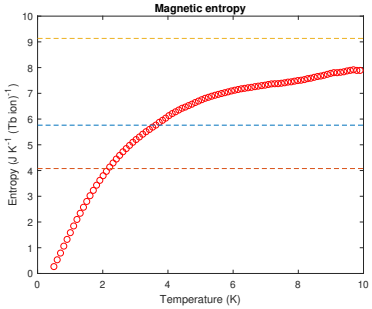

(d) The film's magnetic entropy.

Figure 6.11: The different stages in the heat capacity analysis for sample 18:Tb500nm(001)19. The red, blue and orange dashed lines in (d) correspond to $R\ln(2) - \left(\frac{R}{2}\right)\ln\left(\frac{3}{2}\right)$, $R\ln(2)$ and $R\ln(3)$ respectively.

its out-of-plane direction. Its magnetic moment is similar to that of the bulk. The residual magnetic entropy that is found in the bulk is partially recovered making this thick film different from the bulk and the previous thinner $Dy_2Ti_2O_7$ films, which were able to recover all of the residual entropy. Additionally, the recovered entropy seems to match the square-ice's entropy, which is consistent with theoretical predictions of a surface-ordering transition. The film of sample 16:Yb500nm(001)19 appears to have two different fully strained phases, which have lattice constants that are compressed along both their in-plane and out-of-plane directions. Its fitted magnetic moment is less than bulk $Yb_2Ti_2O_7$ and is close to the value expected from $\langle 111 \rangle$ Ising spins, though this has been interpreted as a coincidence rather than a sign of Ising-like spins. Its magnetic entropy is less than the $R\ln(2)$ J K^{-1} mol$^{-1}_{Yb}$ seen in the bulk, but more than the Pauling entropy. Unlike the other two samples, sample 18:Tb500nm(001)19 is not fully strained. Its RSM streak implies that the film's in-plane lattice constant matched the substrate's originally (so a compressed lattice constant), but as it grew its lattice constants expanded towards the

cubic line, corresponding roughly to its out-of-plane lattice constant. Both its magnetic moment and entropy are significantly lower than their bulk values.

Of the three investigated films only $Dy_2Ti_2O_7$ was able to form a single crystal film that was fully strained. In the future, the limit of how thick these $Dy_2Ti_2O_7$ films could be grown before relaxing or creating additional phases could be tested. Another future experiment could involve probing the films' electric conductivity. This may be able to shed some light onto how films have different lattice constants to their bulk. Oxygen ions make up the majority of the volume in these rare-earth titanate unit cells and so a reasonable assumption is that films with a smaller lattice constant than their bulk value may have a lower proportion of oxygen. It has been shown that oxygen vacancies can have an impact on a material's electrical conductivity [40] and so a quantitative value might be able to be determined. As a follow-up to this, the samples could be heated in an attempt to oxidise them. The heat capacity, magnetometry and crystal structure could then be remeasured to observe the impact of the oxidation.

Chapter 7

$Tb_2Ti_2O_7$ Thin Films

The frustrated magnet $Tb_2Ti_2O_7$ is an insulator with a cubic space group of $Fd\bar{3}m$ [34]. In the bulk, $Tb_2Ti_2O_7$ has a Curie-Weiss temperature of ≈ -14 K [35]. Despite this bulk, $Tb_2Ti_2O_7$ fails to magnetically-order down to $T = 50$ millikelvin and instead becomes a QSL. Despite being a QSL, it displays characteristic anisotropies of a spin ice when a magnetic field is applied [2]. It is still unknown whether the ice rules are obeyed by bulk $Tb_2Ti_2O_7$ and whether there are any other factors controlling it [12]. $Tb_2Ti_2O_7$ is an interesting material because of the mystery surrounding its magnetic properties.

This chapter focuses on heat capacity measurements, which were performed on three $Tb_2Ti_2O_7$ thin films. Each film had a different out-of-plane crystallographic orientation: [111], [100] and [110]. Prior to these measurements, it was confirmed that all of these films were fully strained. Four different single-ion models were fitted to each films' magnetic specific heat divided by the temperature, the most successful being the four singlet state model. There has been some controversy surrounding the nature of the ground state of bulk $Tb_2Ti_2O_7$, with arguments for either a ground state doublet or a split doublet. The results presented are impactful on this debate because they imply that the $Tb_2Ti_2O_7$ thin film's ground state is a doublet. A hyperfine correction for the single-ion model was also tested, but the results implied that the hyperfine contribution was negligible.

7.1 Introduction

7.1.1 $Tb_2Ti_2O_7$

This chapter focuses on thin films of the frustrated magnet $Tb_2Ti_2O_7$, which is an insulator with a cubic space group of $Fd\bar{3}m$ [34]. It has a Curie-Weiss temperature of ≈ -14 K [35]. Despite this, $Tb_2Ti_2O_7$ fails to magnetically-

order down to $T = 50$ millikelvin and instead becomes a QSL. Despite being a QSL $Tb_2Ti_2O_7$ displays characteristic anisotropies of a spin ice when a magnetic field is applied [2].

7.2 Method

7.2.1 Experimental procedure

To acquire the magnetic specific heat of the $Tb_2Ti_2O_7$ thin films, the heat capacity of the addenda (sample platform and the applied grease) and sample plus addenda were measured. The addenda measurement was always taken first so that its contribution to the total heat capacity could be subtracted when the sample was being measured. This subtraction was automatically performed by the PPMS's standard software. The software uses polynomial interpolation to acquire addenda values that match each sample temperature measurement. The addenda measurement procedure involved applying grease to a puck's sample platform, which was then inserted into the PPMS's probe. A sequence was written for the PPMS, which took measurements from approximately 50 K to 0.35 K. The temperature step size was set to decrease as the temperature decreased. After completing the addenda measurement, the sample was fixed to the puck's sample platform using the grease that was used in the addenda measurement. The addenda's temperature steps were repeated during the sample measurement. The sample's heat capacity was imported into Matlab for further analysis.

7.2.2 Properties of the films

The data outputted by the PPMS was reduced by eliminating data points where the equipment remeasured the heat capacity, which occurred when the temperature was unstable. Each temperature was measured three times by the PPMS, and so the average of each temperature was taken. The sample heat capacity includes the film and substrate heat capacities. However, only the magnetic heat capacity of the $Tb_2Ti_2O_7$ thin films was of interest. This required the subtraction of the substrate and the film's phonon contribution from the total heat capacity. The different samples used will be referred to as 25:Tb64nm(111)15, 21:Tb62nm(100)15 and 00:Tb63nm(110)15. The explanation of this notation is given in section *Sample notation* of Chapter 5. Sample 00:Tb63nm(110)15 was originally called 'Test' instead of a number, but to be consistent with the nomenclature used in this thesis it was renamed to sample

00. The film thickness of samples 25:Tb64nm(111)15, 21:Tb62nm(100)15 and 00:Tb63nm(110)15 is 63.95(4) nm, 62.39(4) nm and 62.69(3) nm respectively. The value in the brackets represents the error in the last significant figure of each thin films' thickness. The length and width of each sample is approximately 4 mm by 4 mm. Previous studies have shown that the average density of the films are similar to the bulk value [12]. The nominal film mass for each film was calculated by multiplying their volume by the reported density of bulk $Tb_2Ti_2O_7$ [41]. The nominal film mass for samples 25:Tb64nm(111)15, 21:Tb62nm(100)15 and 00:Tb63nm(110)15 was 6.91 μg, 6.74 μg and 6.77 μg respectively. The nominal mass of each film was smaller than the precision of the scales that were used to measure the samples, meaning the substrate mass can be taken as the total sample mass because the film contribution to the measured mass is negligible. The heat capacity of a $Y_2Ti_2O_7$ substrate was measured by a past group member. This data was multiplied by the ratio of the sample mass and the mass of the $Y_2Ti_2O_7$ substrate, which had been previously measured. The substrate heat capacity contribution of each sample was calculated in this way.

7.2.3 Background thermodynamics

Using basic thermodynamics, an expression for the heat capacity has been derived below:

$$dU = TdS + B_0 dm$$

$$G = U - mB_0 - TS$$

$$dG = dU - mdB_0 - B_0 dm - TdS - SdT$$

$$dG = \cancel{TdS} + \cancel{B_0 dm} - mdB_0 - \cancel{B_0 dm} - \cancel{TdS} - SdT$$

$$dG = -mdB_0 - SdT$$

$$\frac{\partial G}{\partial T} = -S$$

$$\frac{\partial^2 G}{\partial T^2} = -\frac{\partial S}{\partial T} = -\frac{C}{T}$$

$$C = T\frac{\partial S}{\partial T} = -T\frac{\partial^2 G}{\partial T^2} \tag{7.1}$$

The Gibbs free energy is given by:

$$G = -T \times \log(\mathrm{Q})$$

where Q is the partition function.

7.2.4 Phononic heat capacity subtraction

Initial attempt

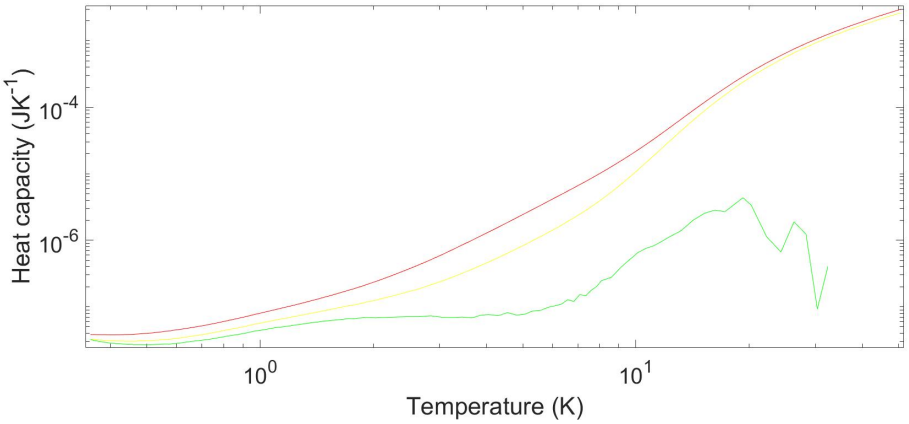

Figure 7.1: The different stages of heat capacity analysis for 25:Tb64nm(111)15. The total heat capacity, the sample heat capacity and the film's magnetic specific heat are represented by the red, yellow and green lines respectively.

The most challenging part of the analysis was the subtraction of the phonon contribution to the heat capacity; multiple attempts and methods were tested. Figure 7.1 shows the first attempt at analysing the heat capacity. The red line represents the total heat capacity measured before any subtractions were made. The yellow line represents the heat capacity after the addenda heat capacity was subtracted, leaving only the sample's heat capacity. The green line represents the heat capacity after the substrate and phononic contributions to the heat capacity were subtracted off the sample's heat capacity, leaving only its magnetic film heat capacity. Something to note is that at higher temperatures, $\approx$ 10 K, the films' heat capacities become increasingly less smooth, which is displayed in Figure 7.1. This features in all of the heat capacity results because as the temperature increases the heat capacity increases, which increases the absolute error from the subtraction of the unwanted heat capacities. The significant size difference between the film and substrate causes the subtraction's absolute error to drown out the film's signal at high temperatures.

Figure 7.2 displays the differences in results before and after the phonon subtraction as well as how they compare with a single-ion model. The red line represents the specific heat of the film divided by the temperature. The specific heat of the film was acquired by subtracting the substrate heat capacity and dividing by the film mass. The yellow line represents the magnetic specific heat of the film, which was acquired by subtracting the phonon heat capacity from the film heat capacity. This subtraction involved multiplying the substrate

heat capacity by a constant such that the magnetic specific heat became more symmetrical about zero (at high temperatures), which was thought would signal the complete subtraction of the phonon contribution. The reasoning for this was that after the phonon contribution had been subtracted only noise would remain at higher temperatures, which should be symmetrical about zero. The constant used for each film orientation ranged from 1 to 1.1. The green line represents a single-ion model that was plotted against the magnetic specific heat divided by the temperature.

Using the equations 7.1 and 7.2, a single-ion model was constructed:

$$Q = 1 + \exp(-A/T) + \exp(-B/T) + \exp(-C/T) \tag{7.2}$$

where A, B and C represent the energies of different energy states. For the first attempt, the single-ion model was not used in a fitting function and instead the energy values A, B and C were manually inputted. The model was refined by repeatedly choosing values for A, B and C such that the model progressively looked more like the data up to $\approx$ 10 K.

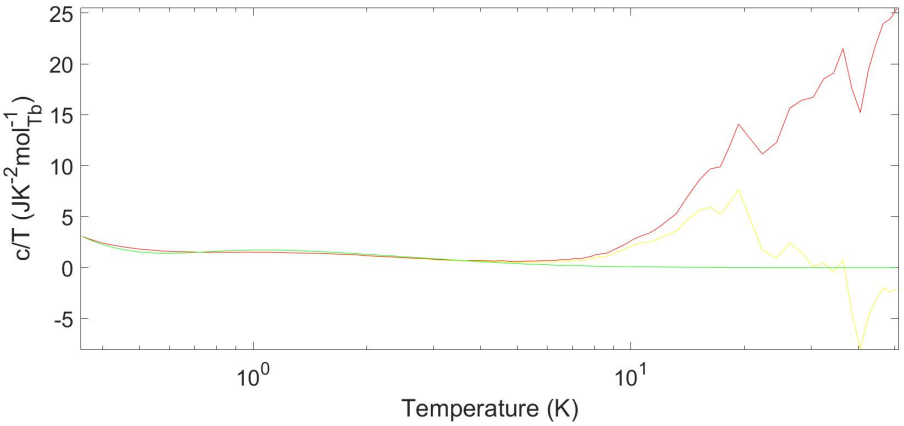

Figure 7.2: The different stages of the specific heat analysis of sample 25:Tb64nm(111)15. The film's specific heat divided by the temperature, the film's magnetic specific heat divided by the temperature and the manually-fitted single-ion model are represented by the red, yellow and green lines respectively.

Results compared with reported results

The method outlined for the phonon subtraction was used for all three film orientations. There were concerns over the reliability of the results and the method which was used to subtract the phonon heat capacity. As the temperature increased, the magnetic specific heat on all plots rose dramatically at higher temperatures, which is a sign that the phononic heat capacity had not

been subtracted completely. This is because the phononic heat capacity has a T^3 dependence at low temperatures according to Debye. Another problem encountered was that it became difficult to assess if a change in energy of an energy level improved the model. This ambiguity could have been avoided if a fitting function had been used to fit the model to the data. The heat capacity measurements of sample 00:Tb63nm(110)15 had already been reported on [12]. The analysed data for 00:Tb63nm(110)15 was compared with the reported results to determine if the method of phonon subtraction was correct. Figure 7.3 displays the film magnetic specific heat divided by the temperature of sample 00:Tb63nm(110)15 plotted against the temperature. The red line represents the film's specific heat divided by the temperature. The yellow line represents the film's magnetic specific heat divided by the temperature. The green line represents the model that was used to analyse the other film orientations. This model used the reported energy levels 8.8 kelvin, 3.7 kelvin and 0.25 kelvin for A, B and C respectively. Figure 7.4 shows the reported results [12]. It is clear that the method, which was used to analyse the raw heat capacity data, differs from the one used to acquire the reported results. The most likely difference comes from the method used to subtract the phonon contribution. In terms of the model, there does not appear to be any difference between the derived model and the reported model. Due to the noticeable difference between the two sets of data, it was determined that the phonon subtraction needed to be revisited and that a fitting function would be required.

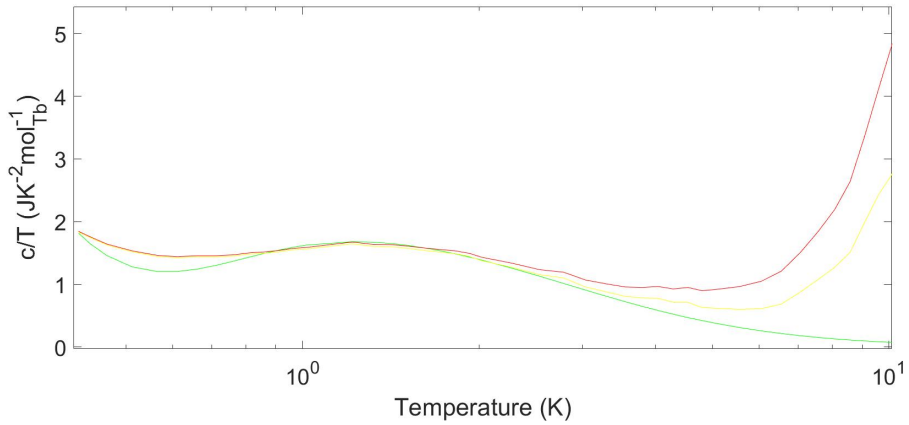

Figure 7.3: The different stages in the specific heat analysis of sample 00:Tb63nm(110)15 and the reported single-ion model. The film's specific heat divided by the temperature, the film's magnetic specific heat divided by the temperature and the reported single-ion model are represented by the red, yellow and green lines respectively. The single-ion model has energy levels of 8.8 kelvin, 3.7 kelvin and 0.25 kelvin.

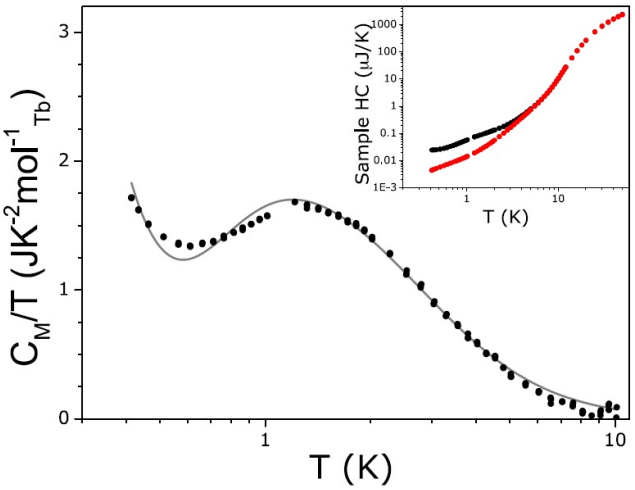

Figure 7.4: The reported magnetic specific heat divided by the temperature and model of sample 00:Tb63nm(110)15. The magnetic specific heat and a four singlet single-ion model are represented by the black dots and line respectively. The insert shows the heat capacity of the sample (black) and the substrate (red) plotted against the temperature. This figure has been reproduced from [12].

Phonon subtraction revisited

The second method for subtracting the phonon heat capacity used the low temperature limit of the Debye model, which is given in equation 7.3.

$$C = \frac{12Nk_{\mathrm{B}}\pi^4}{5}\left(\frac{T}{\Theta_{\mathrm{D}}}\right)^3 \tag{7.3}$$

A description of the Debye model can be found inside Chapter 2. According to Debye, at low temperatures the heat capacity of a material has a $\approx T^3$ dependence. Since $Tb_2Ti_2O_7$ and $Y_2Ti_2O_7$ have a very similar structure, it was assumed that the temperature-dependence of both materials was virtually identical. The difference between the $Tb_2Ti_2O_7$ and $Y_2Ti_2O_7$ Debye temperatures was accounted for by shifting the substrate heat capacity with respect to temperature in order to account for a slightly different Debye temperature. The shifted substrate heat capacity was made as close as possible to the sample heat capacity, which is shown in Figure 7.5. This shift effectively combines the substrate heat capacity and the film phonon heat capacity such that they only correspond to a single Debye temperature, as if the sample was made from one material.

The film's magnetic heat capacity was acquired by subtracting the shifted substrate heat capacity from the sample heat capacity. This was then divided by the film mass to give the film's magnetic specific heat. This was followed up by dividing by the temperature. This is the conventional form to express

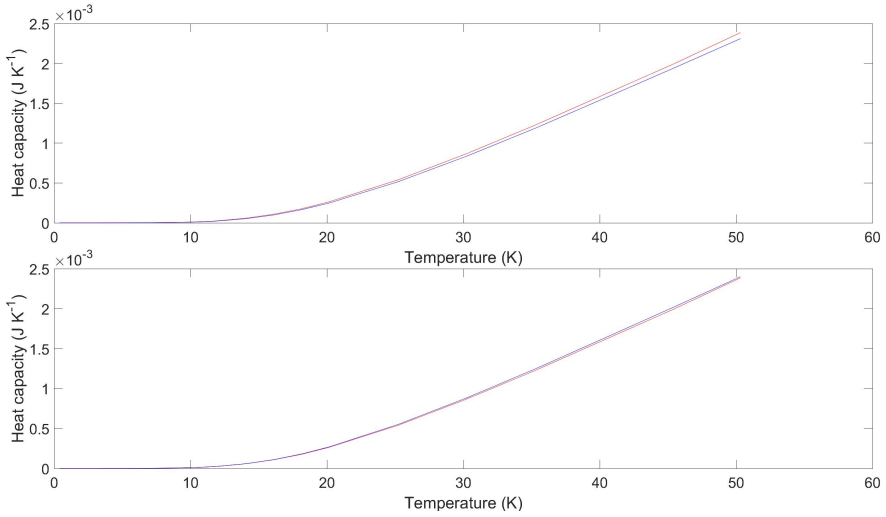

Figure 7.5: The before and after of the heat capacity substrate shift, which accounts for the phonon heat capacity. The red line represents the sample heat capacity and the blue line represents the the substrate heat capacity before it has been shifted (top) and after its shift (bottom).

specific heat data because the area under the curve corresponds to the entropy. The units were modified from kg to per mole of Tb by multiplying by the molar mass of Tb in $Tb_2Ti_2O_7$.

7.2.5 Single-ion model fitting

Using equation 7.1, four different single-ion models were fit to the data using the Matlab function lsqcurvefit. The model was changed by altering the optimise-able variables in the Gibbs free energy. The four models tested were: four singlet states, a ground state and excited state singlet with an excited doublet state, a ground state doublet with two excited singlet states, and a ground state and an excited state doublet. The changes to the Gibbs free energy are shown below respectively. A graphical representation of the energy levels is shown in Figure 7.6.

$$G = -T \times \log(1 + \exp(-\mathrm{A/T}) + \exp(-\mathrm{B/T}) + \exp(-\mathrm{C/T}))$$

$$G = -T \times \log(1 + \exp(-\mathrm{A/T}) + \exp(-\mathrm{B/T}) + \exp(-\mathrm{B/T}))$$

$$G = -T \times \log(2 + \exp(-\mathrm{A/T}) + \exp(-\mathrm{B/T}))$$

$$G = -T \times \log(2 + \exp(-\mathrm{A/T}) + \exp(-\mathrm{A/T}))$$

There were multiple sets of values that the lsqcurvefit function outputted. These sets of values were chosen by the function based on the initial guesses. The set of values that best described the data was selected based on how

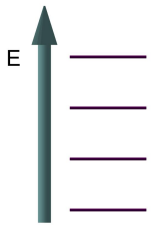

(a) Energy levels corresponding to four singlets.

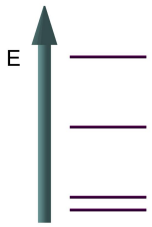

(b) Energy levels corresponding to a ground state doublet with two excited singlets.

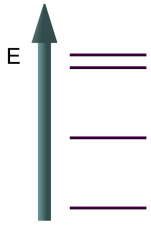

(c) Energy levels corresponding to an excited doublet with two singlets.

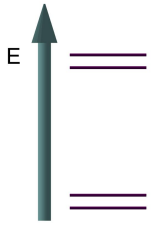

(d) Energy levels corresponding to a ground state doublet and excited doublet.

Figure 7.6: The different configurations of energy levels which were fit using the single-ion model.

small the sum of squared errors of prediction (SSE) were and if the fit's shape resembled the data. The number of variables fit was experimented with, for instance lsqcurvefit was set to optimise only the energies A, B and C in the Gibbs free energy equations when the films' nominal masses were used. Each film mass was incredibly small so knowing the exact mass was unlikely and the film masses were calculated using the assumption that the whole of the substrate's surface was covered, but this may not be the case. It is for these reasons that the film mass was used as a fitting parameter for most of the fits. Two methods were used to optimise the film mass. The first method involved varying the film mass outside the lsqcurvefit function by using a for loop. In most cases the film mass was varied by $\pm$ 20 % of the nominal film mass with steps of 1 % of the nominal mass. The set of energies that the lsqcurvefit function outputted were chosen based on which film mass minimised the SSE the most.

The other method involved inserting a variable into the function that the lsqcurvefit function optimised. This variable represented the ratio between the optimised mass and the nominal mass. A parametric test, which involves plotting the lsqcurvefit residuals against temperature, was used to assess if systematic errors were present in the final result. If the residuals randomly varied about zero then no systematic error was introduced during the analysis.

7.3 Results/Discussion

7.3.1 Nominal film mass

The $Tb_2Ti_2O_7$ thin films were first analysed using their nominal masses. Figure 7.7 displays the film magnetic specific heat divided by the temperature. The circle markers and lines correspond to the data points and the fitted four singlet single-ion models respectively. The results have been colour-coded so that black, purple and red correspond to samples 25:Tb64nm(111)15, 21:Tb62nm(100)15 and 00:Tb63nm(110)15 respectively. The results for each film orientation appear similar because the models overshoot their respective data set at roughly the same point. The Schottky peak in the 00:Tb63nm(110)15 model stops prematurely compared with the other films because the other film orientations were measured to a lower temperature. As the temperature increases, the goodness of fit seems to diminish for the 25:Tb64nm(111)15 and 00:Tb63nm(110)15 films, which is somewhat expected because as the temperature increases so does the absolute error in the phonon subtraction. The 21:Tb62nm(100)15 goodness of fit does not seem to suffer as much at high temperature. This implies that a small amount of the phonon contribution to the heat capacity may still be present in the other films. Due to how similar the films' low temperature data is, the remaining phonon contribution was thought to be negligible in this analysis.

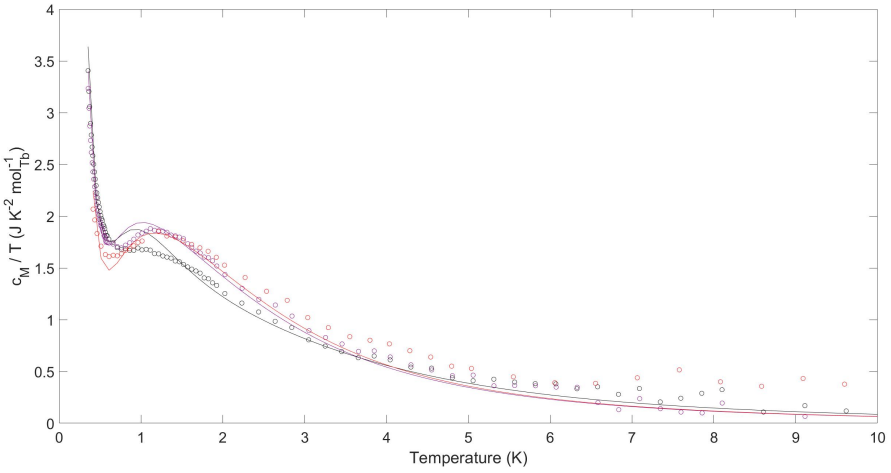

Figure 7.7: The films' magnetic specific heat divided by the temperature along with fitted four singlet single-ion models. The nominal films' masses were used in calculating the magnetic specific heat. The line and circle markers correspond to the fitted single-ion model and the measured data respectively. The results are colour-coded such that black, purple and red correspond to the samples 25:Tb64nm(111)15, 21:Tb62nm(100)15 and 00:Tb63nm(110)15 respectively.

7.3.2 Optimised film mass

Below Figure 7.8 shows the data of the three films 25:Tb64nm(111)15, 21:Tb62nm(100)15 and 00:Tb63nm(110)15. The colours and symbols have the same meaning in Figure 7.8 as they do in Figure 7.7. An optimised film mass was used in the analysis of each film's data. This optimisation involved adjusting the films' mass outside of the fit and then using that modified mass inside of the fit as a constant. A four singlets single-ion model was fit to each film. The optimised film masses were a factor of 1, 1.06 and 0.97 from the nominal film masses of 25:Tb64nm(111)15, 21:Tb62nm(100)15 and 00:Tb63nm(110)15 respectively. Since the difference between the optimised film mass and the nominal film mass is so small, Figure 7.8 appears similar to Figure 7.7. The reduced film mass of 00:Tb63nm(110)15 appears to have shifted the data slightly higher and the increased film mass of 21:Tb62nm(100)15 has shifted the data slightly lower. This difference in film mass does not seem to have had a significant impact because the four singlet single-ion model remains the best model.

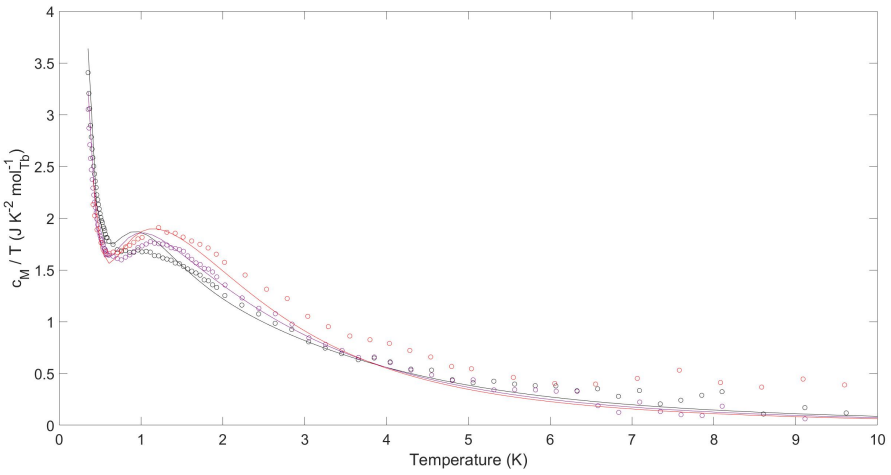

Figure 7.8: The films' magnetic specific heat divided by the temperature, along with fitted four singlet single-ion models. The film mass was not a fitted parameter and was optimised outside the fitting function. The line and circle markers correspond to the fitted single-ion model and the measured data respectively. The results are colour-coded such that black, purple and red correspond to the samples 25:Tb64nm(111)15, 21:Tb62nm(100)15 and 00:Tb63nm(110)15 respectively.

7.3.3 Least squares film mass

Figure 7.9 displays the film magnetic specific heat divided by the temperature of the three films 25:Tb64nm(111)15, 21:Tb62nm(100)15 and 00:Tb63nm(110)15.

The colours and symbols have the same meaning in Figure 7.9 as they do in Figure 7.8. In this analysis, the film mass has been used as a fitting parameter in the lsqcurvefit function. The four singlets single-ion model was the most successful model that was fitted to each film. When comparing the films from the different methods, there does not appear to be much difference from Figures 7.9, 7.7 and 7.8. This is expected because the optimum model for all of the data sets has been the same.

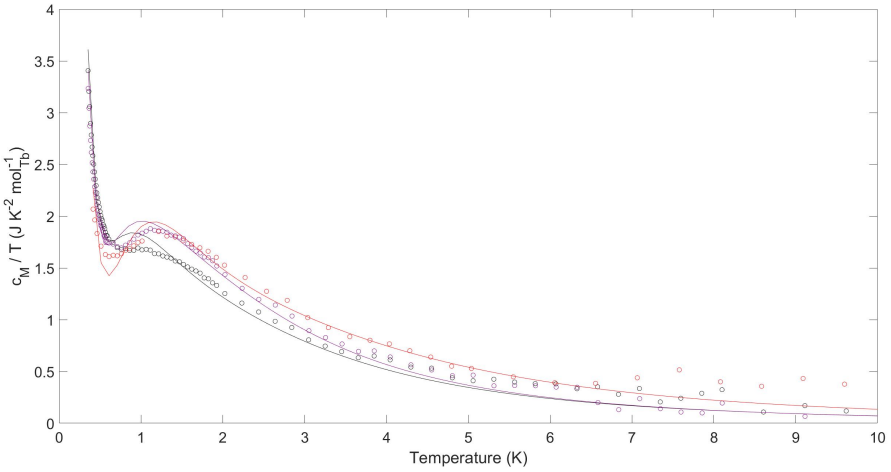

Figure 7.9: The films' magnetic specific heat divided by the temperature along with fitted four singlet single-ion models. The films' masses were treated as a fitting parameter. The line and circle markers correspond to the fitted single-ion model and the measured data respectively. The results are colour-coded such that black, purple and red correspond to the samples 25:Tb64nm(111)15, 21:Tb62nm(100)15 and 00:Tb63nm(110)15 respectively.

Despite the similarity between the different sets of results, more confidence is placed in this method of optimising the film mass than in the previous methods. As a result, the analysis of these results will be more thorough. Figures 7.10, 7.11 and 7.12 display the different data sets shown in Figure 7.9 separately. The top graph of these figures is a plot of the film magnetic specific heat divided by the temperature plotted against the temperature. The red line corresponds to the four singlets single-ion model, which was fitted to the data points (blue circles). The bottom graph of each figure is a parametric test, which compares the model's residuals against the sample temperature. The blue circles and red lines correspond to the residuals of the top graph and a residual of zero. A parametric test's purpose is to reveal any systematic deviations between the data and the fitted single-ion model. These systematic deviations are revealed if the residuals are not randomly distributed about zero. The residuals in each figure show that there are systematic errors below $\approx$ 2 K and that the shape of the residuals remains consistent for each film.

The residuals appear more extreme in Figure 7.10, but this is due to a smaller scale on the y-axis. Above 2 K the residuals seem to behave randomly, which implies that the the phonon subtraction was successful.

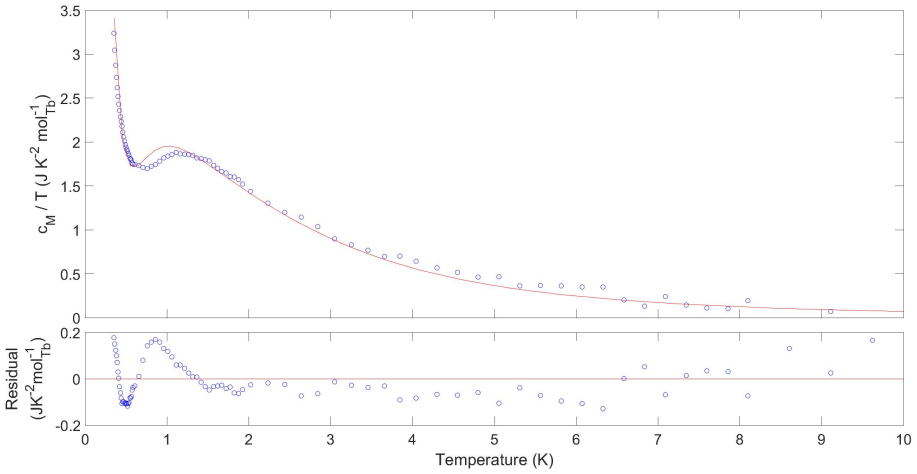

Figure 7.10: (Top) The magnetic specific heat divided by the temperature of 21:Tb62nm(100)15. The red line represents a four singlet single-ion model that was fitted to the data. (Bottom) The residuals associated with the above plot were plotted along with a red line that represents a residual of zero. This model was the best fit for the 21:Tb62nm(100)15 thin film.

The fitted energy levels and film mass fractions are displayed in Table 7.1. The optimum energy levels for each film are incredibly similar. The film masses of 25:Tb64nm(111)15 and 21:Tb62nm(100)15 have been slightly shifted away from the nominal mass, but the difference in size between the optimum film mass and the nominal film mass is not concerning. This is because a difference in mass could be used to account for potential errors in the films' surface area, for instance. Also, the optimum film masses of 25:Tb64nm(111)15 and 21:Tb62nm(100)15 are within error of their nominal film mass. The most concerning value inside Table 7.1 is the film mass of 00:Tb63nm(110)15; it is difficult to construct a reasonable argument to explain why a fifth of a thin film has gone missing. What adds to the confusion is that the optimised film mass fraction that was obtained from varying the film mass outside of the lsqcurvefit function was 0.97, which is reasonable.

Due to the anomaly in the film mass of 00:Tb63nm(110)15, it was deemed necessary to look at the next best model. It was hoped that a model of a ground state singlet, an excited doublet and an excited singlet would give a more realistic optimum film mass. Figure 7.13 displays this model fitted to the 00:Tb63nm(110)15 data. The colours and symbols of Figure 7.13 have the same meaning as in Figure 7.12. When the top graphs of Figures 7.12 and 7.13 are compared, it is clear that Figure 7.12 has a significantly better fit.

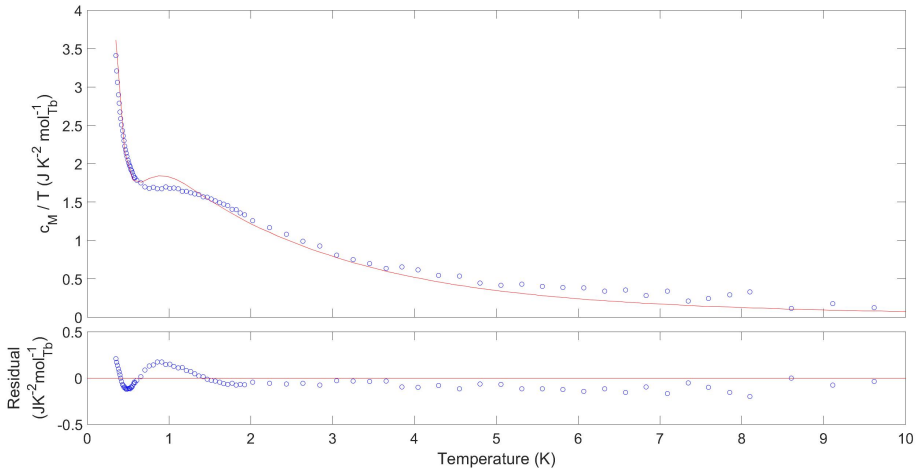

Figure 7.11: (Top) The magnetic specific heat divided by the temperature of 25:Tb64nm(111)15. The red line represents a four singlet single-ion model that was fitted to the data. (Bottom) The residuals associated with the above plot were plotted along with a red line that represents a residual of zero. This model was the best fit for the 25:Tb64nm(111)15 thin film.

	25:Tb64nm(111)15	21:Tb62nm(100)15	00:Tb63nm(110)15
E_1 (K)	0.31(1)	0.284(8)	0.25(1)
E_2 (K)	3.3(1)	3.35(7)	3.8(2)
E_3 (K)	9(1)	8.3(7)	12(2)
mass / nominal mass	1.06(7)	0.97(4)	0.79(6)

Table 7.1: The fitted energy levels and film masses for each sample when using a 4 singlet single-ion model.

Above $\approx$ 2 K the residuals imply that there are systematic errors. Given that this error is at higher temperatures, it implies that the source of this error comes from the phonon heat capacity subtraction. Below $\approx$ 2 K, the same-shaped systematic error that is seen in Figure 7.12 was reproduced in a more pronounced way. This could represent the limitations of the single-ion model since this systematic error appears across different models. The associated energies and film mass fraction from the fit in Figure 7.13 are 4.6(3), 4.6(3), 0.34(3) and 1.2(1) respectively. This optimised film mass has roughly the same size difference as the four singlet model except that its difference results in a larger film instead of a smaller film. This dramatic increase in the film mass is difficult to justify. Given that the excited doublet model does not seem to improve the film mass, the more favourable model is of four singlets because it reduces the SSE more.

These results suggest that there is only a minor effect on the first few energy levels when the out-of-plane crystallographic orientation of the $Tb_2Ti_2O_7$ thin films is changed. This is surprising because a previous study has revealed

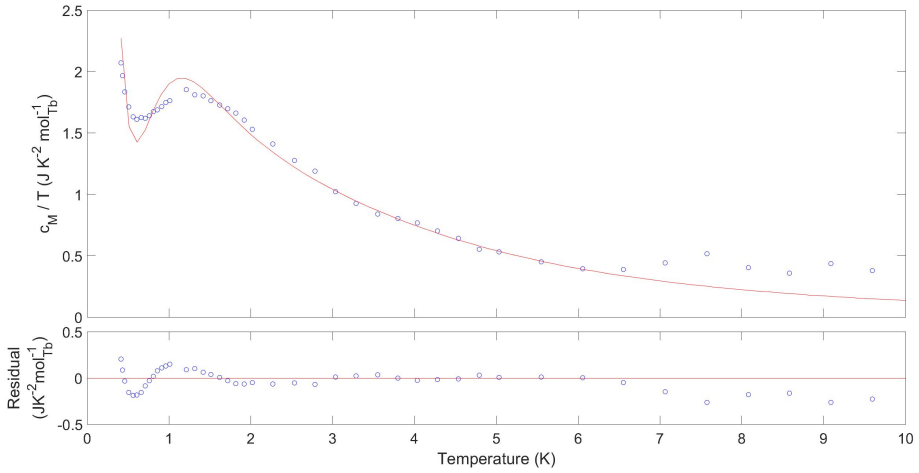

Figure 7.12: (Top) The magnetic specific heat divided by the temperature of 00:Tb63nm(110)15. The red line represents a four singlet single-ion model that was fitted to the data. (Bottom) The residuals associated with the above plot were plotted along with a red line that represents a residual of zero. This model was the best fit for the 00:Tb63nm(110)15 thin film.

that the epitaxial strain causes the bulk $Tb_2Ti_2O_7$ unit cell to elongate along the film's out-of-plane direction and compress along its in-plane directions. This study also showed that this strain significantly changes the bulk heat capacity, and so one would expect that the heat capacity would be affected by the direction of this strain [12]. However, the results imply the opposite. One possible explanation for this may be found by considering how a tetrahedron is created when a sphere is approximated using only four equidistant points. From this it can be assumed that tetrahedrons have an approximate spherical symmetry despite there being a significant difference between a sphere and a tetrahedron. The approximate spherical symmetry of the corner-sharing tetrahedra in $Tb_2Ti_2O_7$ may therefore explain why its heat capacity is affected only slightly by the applied strain's direction.

Regarding the energy level structure, there is agreement in the literature that bulk $Tb_2Ti_2O_7$ has an excited doublet at $\approx$ 18 K [34, 35]. The energy structure of bulk $Tb_2Ti_2O_7$ has been seen in neutron scattering measurements, which showed two energy bands [35]. It is believed that the $Tb_2Ti_2O_7$ thin films have maintained this dual band structure because the energy levels for each film are similar. The best single-ion model for each film was of four singlets. This model dominated in part because two energy bands is mathematically well approximated by four delta functions. Due to this, the physical implications of the model need to be treated with caution. It is nevertheless reasonable given the similarities between the films to assume that the films differ from bulk $Tb_2Ti_2O_7$ only by a small perturbation so that the four-state picture remains

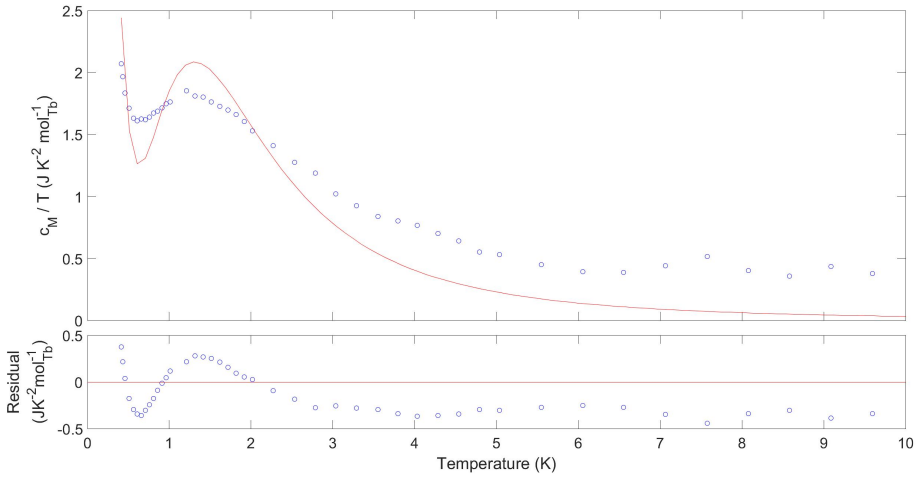

Figure 7.13: (Top) The magnetic specific heat divided by the temperature of 00:Tb63nm(110)15. The red line represents a single-ion model of a ground state singlet, an excited singlet and an excited doublet, which was fitted to the data. (Bottom) The residuals associated with the above plot were plotted along with a red line that represents a residual of zero.

a good initial model. It is possible that the film's strain could have caused the excited doublet to split but more experiments are required to confirm this. The higher energy band varies from ≈ 3.5 to 10 K.

There has been some controversy surrounding the nature of bulk $Tb_2Ti_2O_7$'s ground state. Theoretical considerations suggest the bulk ground state to be either a doublet or a singlet with an excited singlet at an energy of $\delta = 1.8$ K [34, 35]. The work presented in this thesis is impactful on this discussion because the lowest excited energy level for each film is ≈ 0.28 K, which is much lower than the proposed $\delta = 1.8$ K energy gap from Chapuis, implying that the $Tb_2Ti_2O_7$ thin films have a ground state doublet. The width of the energy bands depends not only on the crystal field energy levels, but also on the effective exchange energy, which is given by $J_{\text{eff}} = J_{\text{nn}} + D_{\text{nn}}$ where J_{nn} is the nearest-neighbour exchange and D_{nn} is the nearest-neighbour dipolar exchange. This means that $\delta, |J_{\text{eff}}| \lesssim 0.28$ K. It is unusual for the effective exchange energy to be this low; this could mean the exchange and dipole interaction are partially cancelling out, suggesting that $J_{\text{nn}} < 0$. Using $\mu_{\text{eff}} = 5.4\ \mu_{\text{B}}$, the dipolar exchange was calculated to be $D_{\text{nn}} = 1.15$ K [12]. Using $J_{\text{eff}} = \pm 0.28$ K, a range for the nearest-neighbour exchange was calculated to be -0.97 K $< \text{J}_{\text{nn}} < -0.41$ K. An exchange energy of this magnitude and sign places the $Tb_2Ti_2O_7$ thin films very close to the phase transition between spin ice and antiferromagnetic-order (all-in, all-out). The phase diagram for magnetic pyrochlores is shown in Figure 7.14. This diagram displays the type

of magnetic-ordering that is expected from Ising pyrochlore magnets, given different ratios of magnetic interactions. The phase transition from spin ice to antiferromagnetism occurs at $\frac{J_{\rm nn}}{D_{\rm nn}} \approx -0.91$ [42], meaning spin ice behaviour wins out over an antiferromagnetic exchange provided the dipolar interaction is large enough. The thin films ratio is given by: $-1.4 < \frac{J_{\rm nn}}{D_{\rm nn}} < -0.6$.

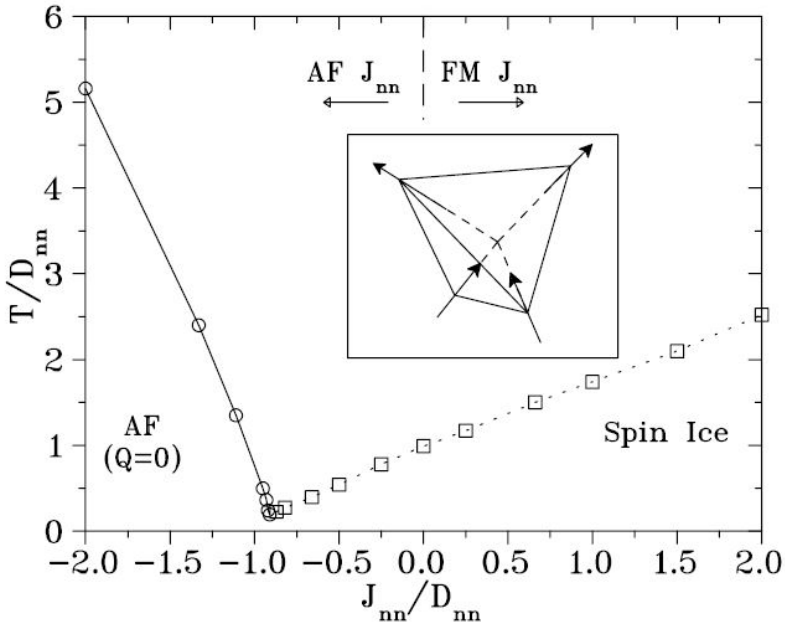

Figure 7.14: The phase diagram for a magnetic pyrochlore with both J_{nn}, nearest-neighbour exchange and long-range dipolar interactions. D_{nn} is the nearest-neighbour dipolar interaction. This figure has been reproduced from [42].

7.3.4 Hyperfine splitting

In the case of $Tb_2Ti_2O_7$, hyperfine specific heat could arise from the nuclear spins of Tb^{3+} ions coupling to their surrounding electrons' spins, which are coupled to other Tb^{3+} ions' electrons. This coupling causes the single-ion states to split. A study on $Tb(OH)_3$ has stated that there is a significant contribution to the specific heat from hyperfine splitting [43]. Both $Tb(OH)_3$ and $Tb_2Ti_2O_7$ are able to be modelled as Ising systems due to their extreme anisotropy. Additionally, the $Tb_2Ti_2O_7$ thin films may have a split Kramer's doublet, which is also seen in $Tb(OH)_3$. Due to the similarities between these two systems, it was thought that an investigation to ascertain if the hyperfine contribution was significant in these films was necessary. Equation 7.4 displays

	25:Tb64nm(111)15	21:Tb62nm(100)15	00:Tb63nm(110)15
E_1 (K)	0.3(1)	0.28(7)	0.3(5)
E_2 (K)	3.3(2)	3.4(1)	3.8(4)
E_3 (K)	9(1)	8.3(7)	12(2)
mass / nominal mass	1.06(7)	0.97(5)	0.79(6)
Hyperfine energy (K)	0.0000	0.0000	0.0000

Table 7.2: A four singlet single-ion model's fitted energy levels and film masses for each thin film if the fitted hyperfine contribution is set to zero. The errors for the hyperfine energy are abnormally large and so have not been stated.

	25:Tb64nm(111)15	21:Tb62nm(100)15	00:Tb63nm(110)15
E_1 (K)	0.0000	0.0000	0.0001
E_2 (K)	3.0969	3.1925	3.7081
E_3 (K)	8.8563	8.1831	11.4077
mass / nominal mass	1.06(7)	0.97(5)	0.79(7)
Hyperfine energy (K)	0.13(7)	0.12(5)	0.1(3)

Table 7.3: A four singlet single-ion model's fitted energy levels and film masses for each thin film if the fitted hyperfine contribution is finite. The energy levels for each thin film are shown to converge to a ground state doublet. The errors for the singlet energy levels are abnormally large and so have not been stated.

the new partition function that was used to account for a hyperfine contribution:

$$\begin{aligned} Q = (1 + \exp(-A/T) + \exp(-B/T) + \exp(-C/T))\times \\ (1 + \exp(-e/T) + \exp(-2e/T) + \exp(-3e/T)) \end{aligned} \tag{7.4}$$

where e represents the degree of splitting between the states which are created from the hyperfine interaction. Using this new partition function, single-ion models were fitted to the data using the lsqcurvefit function. Interestingly enough, the lsqcurvefit function outputted two reasonable solutions for each film. Table 7.2 and 7.3 show the values of the films for each solution. The values of Table 7.2 imply that the hyperfine contribution is negligible and the optimum energies of the four singlets are essentially the same as the energies generated when the hyperfine contribution was not being considered. The values of Table 7.3 imply that the hyperfine contribution is not negligible and that the ground state is a doublet.

Strangely, for each solution the errors on certain parameters are huge, which implies that changing these parameters has very little effect on the fit. In the case of the hyperfine contribution being negligible, the errors for the hyperfine energy are massive and, in the case of the hyperfine contribution being significant, the errors for the singlet energies are massive. These massive errors could be due to the fitting function prioritising either a ground state doublet or

the hyperfine contribution instead of a mixture of the two. This is seen in Figure 7.15 where both energy schemes are given for 25:Tb64nm(111)15 depending on if the hyperfine contribution is zero or finite. This fitting problem could potentially be resolved if the measuring window was extended to lower temperatures because the film's strain may have shifted the hyperfine contribution out of the current measuring window. Given the ambiguity of this situation, the most reasonable course of action is to acknowledge the solution with the smallest SSE. According to the SSE, the best fit implies that the hyperfine contribution is negligible. Again, it is important to stress that this result may change if the measuring window is extended further to lower temperatures.

7.4 Conclusion

This report carried on the work by Bovo *et al.* who had previously reported on the film's magnetic specific heat of sample 00:Tb63nm(110)15 [12]. Specifically, this report investigated the effects of epitaxial strain along different crystallographic directions of $Tb_2Ti_2O_7$ thin films. This included recreating the analysis performed on 00:Tb63nm(110)15, which produced results that were very similar to Bovo's despite the film mass being worryingly small. From the literature, it was unclear which single-ion model was the most appropriate and so four models were tested using various methods of application. The most successful approach used the least squares fitting of the four singlet model because this was the best at matching the data and reducing its SSE. The reason why so many single-ion models were tested was because there has been a debate over the structure of the energy levels of bulk $Tb_2Ti_2O_7$, namely whether or not it has a ground state doublet or two singlet states [34, 35]. The results presented in this report are impactful on this debate because they suggest that $Tb_2Ti_2O_7$ thin films have a ground state doublet. This is due to the film's having a lower energy band width of ≈ 0.28 K, which is significantly smaller than the predicted 1.8 K energy gap between the ground state singlet and excited singlet in the bulk. This this the most important conclusion that can be drawn from this chapter's results and is easiest to see in Table 7.1. From the width of the ground state band, it can be reasoned that the $Tb_2Ti_2O_7$ thin films lie very close to the phase boundary of spin ice and antiferromagnetism. The hyperfine contribution was also investigated, which resulted in the conclusion of it being negligible. However, this result may change if the measuring window is extended to lower temperatures.

It has been reported that bulk $Tb_2Ti_2O_7$ has a large thermal Hall effect [44]. A future experiment in collaboration with Dr. Tom Fennell has been

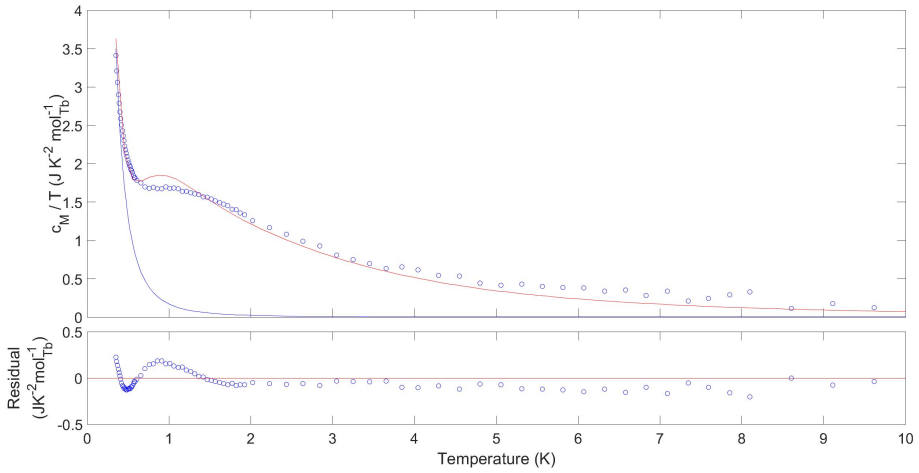

(a) Modelled with a hyperfine contribution. The red line represents the fitted single-ion model and the blue line highlights the contribution of the model's hyperfine component.

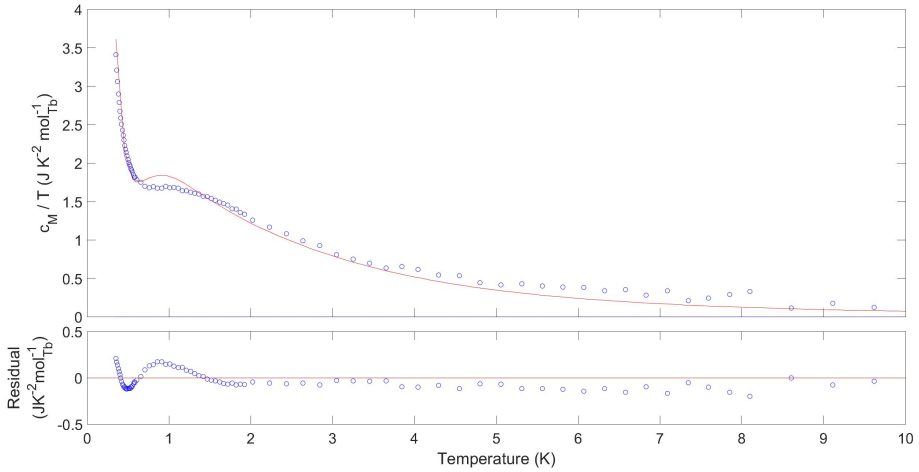

(b) Modelled without a hyperfine contribution.

Figure 7.15: The magnetic specific heat divided by the temperature for sample 25:Tb64nm(111)15 with a single-ion model (red line) that has (a) a non-zero hyperfine contribution or (b) a zeroed hyperfine contribution. The bottom segment of each figure displays the residuals associated with the above model, with the red line representing a residual of zero.

discussed, which will attempt to explain or reproduce the reported results in a more insightful way. This experiment will involve a novel technique and will compare the films with bulk $Tb_2Ti_2O_7$ crystals, with and without disorder.

Chapter 8

Neutron Scattering

As a preface to this chapter, its results were collected after this thesis had been written, but it was decided to add the chapter anyway because it represents a key milestone in the analysis of spin ice thin films; it is the first time neutron scattering has been successfully performed on this type of film.

8.1 Neutron scattering process

Neutron scattering differs from XRD because neutrons interact with the nuclei of the sample instead of the electric cloud from its atoms. There are two types of neutron scattering: nuclear and magnetic. Nuclear scattering occurs when the incident neutrons are scattered off the sample's nuclei. The cross-section for scattering events varies with the number of nucleons or protons (Z number). Surprisingly, due to resonance with nuclear energy levels, there is not a smooth relationship between Z number and cross section. This is due to two types of scattering: resonance and potential. Magnetic scattering is more complicated than nuclear scattering. It occurs when the incident neutrons interact with the electron spin and orbital angular momentum of the sample. The measured magnetic scattering intensity represents the magnetic component that is perpendicular to the scattering vector. The aim of magnetic scattering is to improve our understanding of the sample's magnetic structure. Both nuclear and magnetic scattering can be measured separately or simultaneously depending on the sample and the peak in question.

8.2 ISIS spallation source

At ISIS, neutron beams are created by firing a pulsed beam of high energy protons into a tungsten target. Neutrons are driven out of the tungsten nuclei,

through the spallation process. This beam is slowed down to useful energies by an array of of hydrogenous moderators. Facilities that produce neutron beams this way are referred to as spallation sources.

8.3 WISH

Beamlines at ISIS are optimised to explore different properties of materials. WISH, the beamline used, has been designed to excel at measuring closely packed Bragg peaks that may exist at long d-spacing (equivalent to using a large wavelength in XRD). It is most commonly used for powder diffraction experiments on samples that are magnetic or have large unit cells, but it can also accommodate single crystals. Using a system of choppers, a bandwidth can be selected to prevent frame-overlap, when neutron pulses merge. A single frame bandwidth is set to cover 8 Å out of a d-spacing range of 0.7 - 17 Å. Through the combination of 5 piezoelectric slits, the divergence of its collimated beam can be reduced down to 0.2°. The detector is comprised of an array of ^{3}He gas tubes that are 1 m long and are positioned 2.2 m from the sample point. This array spans an angle of 10 to 360° along a cylindrical locos. The incident neutron beam hits the sample through the remaining 10° gap. WISH can accommodate sample environment kits such as a dilution refrigerator and it has its own dedicated vertical 14 tesla magnetic field.

8.4 Analysis

The neutrons are scattered off the film and are absorbed by a detector, shaped like a band that surrounds the sample in 10° to 360° minus a gap for the incident neutron beam. The neutron beam itself consists of neutrons with all time-of-flights. Each detector element is able to absorb all of these energies. This differs from XRD where the X-ray beam is monochromatic and so a particular reflection can only be found at a particular angle. Instead, a number of reflections can be found at a given angle due to the variance in the time-of-flight. This becomes clear when looking at the Bragg condition, equation 8.1. The time-of-flight of neutrons corresponds to the energy of the neutrons and so there is a spectrum of λ values. This allows multiple d-spacings to be accessed simultaneously. The data analysis involves choosing a mask, which covers a particular area of the detector associated with the reflection of interest. The output of this is a d-spacing spectrum, which is then integrated over the area of interest.

$$n\lambda = 2d\sin(\theta) \tag{8.1}$$

8.5 Results

The blocking temperature, the temperature when spin dynamics are frozen out, of sample 07:Dy500nm(001)19 is shown to lie between 0.3 kelvin and 0.4 kelvin in Figure 8.1. The experiment involved cooling down to 0.4 kelvin with no applied field. Three measurements were taken at 0.4 kelvin: the first was without an applied field, the second with a 0.1 tesla applied field, and the third was without an applied field. The temperature was then lowered and the same series of measurements were carried out. Figure 8.1 was colour-coded green, blue and red, which corresponds to the order of measurements at each temperature respectively. After the blocking temperature has been reached and the applied field has been removed, the magnetisation will not drop to its original value because it has been frozen out of its equilibrium state. It is clear that the red point matches the green point for 0.4 kelvin, but not for 0.3 kelvin. This feature implies that the blocking temperature has been reached and so must lie between 0.3 kelvin and 0.4 kelvin.

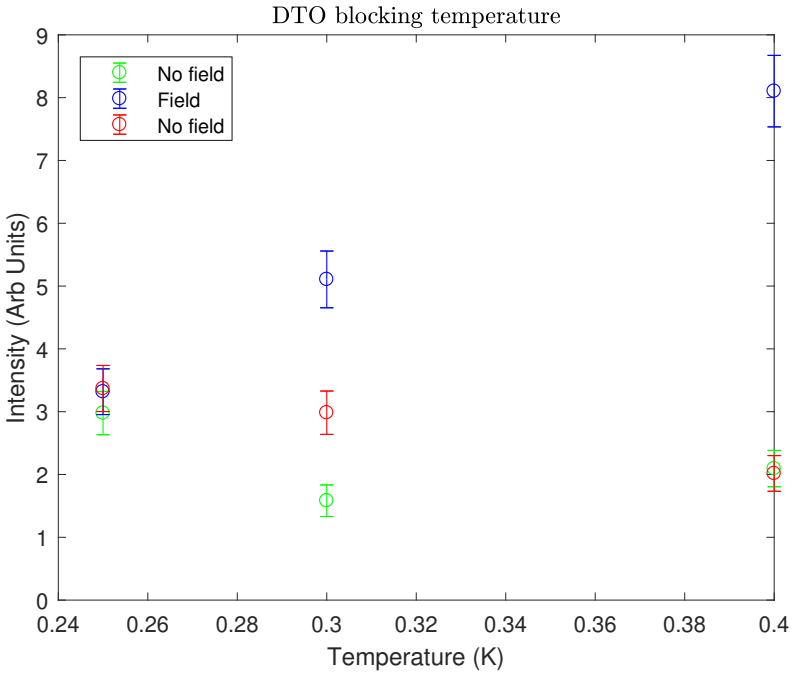

Figure 8.1: The neutron scattering intensity vs H for sample 07:Dy500nm(001)19. The blocking temperature lies somewhere between 0.3 kelvin and 0.4 kelvin because the red point at 0.3 kelvin does not lie on top of the green point at 0.3 kelvin.

Figure 8.2 displays the [002] magnetic Bragg peaks of sample 07:Dy500nm(001)19. The standard reflection conditions for the space group $Fd\bar{3}m$ are given in equations 8.2, 8.3, 8.4 and 8.5. These reflection conditions refer to the allowed nuclear Bragg peaks. The [002] reflection does not correspond to allowed nuclear Bragg peaks, but does exhibit a magnetic peak here. This feature is particularly important because neutrons can measure both magnetic and nuclear properties and so separating these sources of intensity is problematic. The 002 peak allows the measurement of only its magnetic properties because the nuclear component is forbidden. For this reason, particular attention was paid to this reflection and so it was measured at two temperatures, 30 millikelvin and 0.5 kelvin. These measurements involved progressively measuring and increasing the field up to 1.2 tesla and 1.0 tesla respectively, followed by a decrease in the field back down to 0 tesla; both measurements verify that there is a magnetic peak. The notable feature is the ferromagnetic-like hysterisis shown in Figure 8.2a. This is consistent with the surface-ordering phase discussed by Jaubert *et al.* [23].

$$hkl : h + k = 2n \text{ and } h + l, k + l = 2n \tag{8.2}$$

$$0kl : k + l = 4n \text{ and } k, l = 2n \tag{8.3}$$

$$hhl : h + l = 2n \tag{8.4}$$

$$h00 : h = 4n \tag{8.5}$$

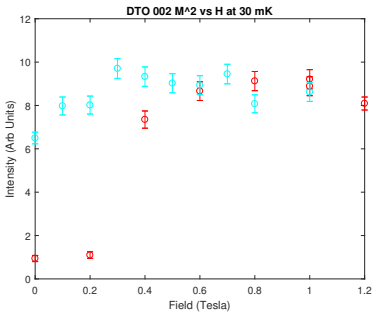

(a) Measurement at 30 millikelvin.

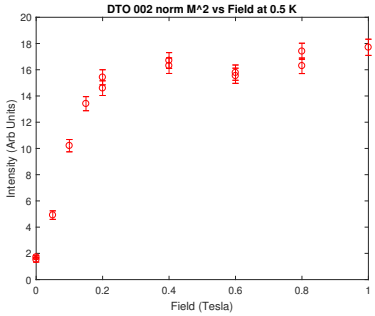

(b) Measurement at 0.5 K.

Figure 8.2: The neutron scattering intensity vs H on the 002 peak of sample 07:Dy500nm(001)19 at (a) 30 millikelvin and (b) 0.5 kelvin. Despite there being only one measurement in (a), two different markers were used (red and light blue circles) to make the ferromagnetic-like hysterisis more clear.

Figure 8.3 presents some of the other neutron peaks that were scanned in a similar way to those in Figure 8.2. Figure 8.3a displays what appears to be a magnetic peak, but it actually is a magnetic and nuclear peak because the $11\bar{1}$ is an allowed reflection. An example of a nuclear peak is presented in Figure 8.3b. There is not a magnetic response to an increasing applied field, which suggests that the signal is entirely nuclear in origin. Lastly, the intensity of the magnetic peak 240 was negligible under fields of 0 and 1 tesla.

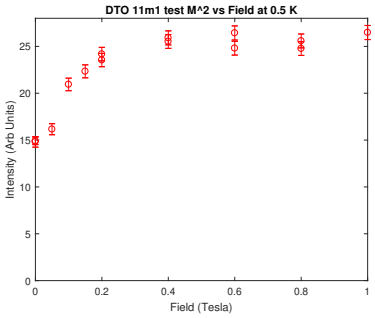

(a) Measurement of the $11\bar{1}$ peak at 0.5 K.

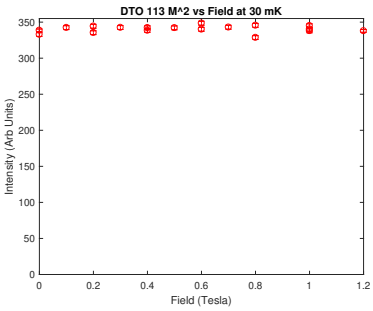

(b) Measurement of the 113 peak at 30 millikelvin.

Figure 8.3: The neutron scattering intensity vs H of different nuclear peaks at different temperatures of sample 07:Dy500nm(001)19.

8.6 Conclusion

The neutron scattering experiments have been used to predict the temperature range at which the blocking temperature occurs and to measure the field-dependence of magnetic peaks at different temperatures, revealing ferromagnetic-like hysterisis at 30 millikelvin, which is consistent with theoretical predictions of a surface-ordering of magnetic charges. Additionally, attempts were made to measure the diffuse scattering of the film, but the signal was too weak to make any progress. One possible explanation for why the experiments seem to support a theoretical model that is of a film which is 1 - 3 monolayers thick (3 showing results that are increasingly more consistent with the bulk) is that the strain in the film isolates each layer from the others, causing them to behave like an array of separate layers. In the future, this could be tested by growing multilayers of $Dy_2Ti_2O_7$ and $Y_2Ti_2O_7$ such that the $Dy_2Ti_2O_7$ layers are sufficiently separated. If the current 07:Dy500nm(001)19 film does have layers which act independently of each other, then the results between these two films would be similar. While the entropy of the film is also consistent with the surface-ordering transition, it remains only a possible explanation for this film.

The neutron experiments have focused solely on the magnetic properties of 07:Dy500nm(001)19 because any attempt at nuclear scattering on the film would be dominated by the substrate, which has an almost identical structure. The magnetic measurements have demonstrated that 500 nm of film is large enough for experiments to be carried out successfully. In the future, nuclear scattering experiments could be attempted on a thick film if its substrate were ground down without destroying the film. This approach would be more desirable than finding a different substrate that has a different unit cell size to the film. The main reason for using $Y_2Ti_2O_7$ as the films' substrate is due to the high quality films that are able to be grown on it thanks to its similar structure.

Chapter 9

Conclusion

This thesis reports on the results of thin films of spin ice and its related materials, which have been grown on $Y_2Ti_2O_7$ substrates. A series of exceptionally thick films ($\sim$ 500 nm) were grown and characterised with heat capacity, magnetometry and XRD techniques. XRD showed that the $Dy_2Ti_2O_7$ film had grown fully strained. Its magnetic moment is similar to that of the bulk, and its residual magnetic entropy is smaller than the bulk's, meaning it has partially recovered the bulk's residual entropy. This makes this film different from the bulk and the previous thinner $Dy_2Ti_2O_7$ films, which were able to recover all of the residual entropy. The XRD of the thick $Yb_2Ti_2O_7$ film is fully strained with potentially two different phases. Its magnetic moment is close to the expected value for $\langle 111 \rangle$ Ising spins and is less than bulk $Yb_2Ti_2O_7$. Its magnetic entropy lies between $R \ln(2)$ J K^{-1} mol$_{\mathrm{Yb}}^{-1}$, seen in the bulk, and the Pauling entropy. Unlike the other two samples, the thick $Tb_2Ti_2O_7$ film was not fully strained. Its magnetic moment is significantly lower than the bulk value, as is its magnetic entropy, which lies between $R \ln(2)$ J K^{-1} mol$_{\mathrm{Tb}}^{-1}$ and $R \ln(3)$ J K^{-1} mol$_{\mathrm{Tb}}^{-1}$. The bulk value of $Tb_2Ti_2O_7$ is $R \ln(4)$ J K^{-1} mol$_{\mathrm{Tb}}^{-1}$.

A number of $Yb_2Ti_2O_7$ thin films were grown of varying length along the crystal directions [111], [1$\bar{1}$0] and [100]. The $Yb_2Ti_2O_7$ chapter broke the films into two groups: the thickness series and the epitaxial series. The thickness series included all of the [111] films, which were shown to not grow epitaxially. XRD was used to show that the [1$\bar{1}$0] and [100] films had grown epitaxially. The specific heat for these films matched the bulk $Yb_2Ti_2O_7$ entropy. The M vs T measurements revealed that these films have magnetic impurities in the substrate, which are most likely ferromagnetic. An equation was fit to the M vs H measurements, which implied that there were paramagnetic impurities in the samples. The impurities present in the samples are thought to have come from the initial components of the $Y_2Ti_2O_7$ substrate. It is suspected that the purest grade of Y_2O3 was not used in the synthesis of the $Y_2Ti_2O_7$ crystals.

Previous characterisation work on some $Tb_2Ti_2O_7$ thin films had been carried out by Bovo *et al.* This work was furthered by investigating the epitaxial strain's impact on the magnetic specific heat of these films. The series included films with an out-of-plane crystal direction of [100], [110] and [111]. This investigation is relevant to a recent debate over the structure of the energy levels of bulk $Tb_2Ti_2O_7$ [34, 35]. Specifically, it was regarding whether or not the ground state of bulk $Tb_2Ti_2O_7$ was a doublet state or two singlet states. The results presented in this report are impactful on this debate because they suggest that $Tb_2Ti_2O_7$ thin films have a ground state doublet. While this does not necessarily mean that this is the case for the bulk, these results present an answer to a perturbation on this debate. In this analysis, the hyperfine contribution was also investigated and was found to be negligible in the measuring window investigated.

Successes and lessons learned over this research will be summarised in the most logical order, beginning with the $Yb_2Ti_2O_7$ thin films, which were the first $Yb_2Ti_2O_7$ thin films that were epitaxially grown on $Y_2Ti_2O_7$ substrates. This respresents the third spin ice related material to be successfully grown in this way. The key results in this chapter were the RSMs shown in Figures 5.3 and 5.13, which imply that these films are more challenging to grow along the [111] crystal direction of $Y_2Ti_2O_7$ substrates, and Figure 5.7, which highlighted the importance of verifying the purity of the substrates before attempting any film growth in the future. The neutron scattering experiments performed on the thick $Dy_2Ti_2O_7$ film were the first neutron scattering measurements on any spin ice related film grown on a $Y_2Ti_2O_7$ substrate. This is a significant milestone as it opens up the possibility for future neutron scattering experiments with the potential to see the way in which spin ice's characteristic pattern changes when the system is perturbed via epitaxial strain. The key results arising from these measurements are shown in Figure 8.2a, which display the predicted ferromagnetic-like hysterisis. This discovery gave new meaning to the sample's entropy shown in Figure 6.4d, which was also in agreement with the theoretical predictions.

This body of work has contributed to the general field of spin ice and frustrated magnetism by: introducing and characterising a new spin ice related system in the form of $Yb_2Ti_2O_7$ thin films that are grown on $Y_2Ti_2O_7$ substrates; presenting the first neutron scattering results on any spin ice thin film; contributing to an area of controversy within the field through the analysis of a $Tb_2Ti_2O_7$ thin film, which is a perturbed version of the original controversial system; and showing that there is so much more to be discovered in this family

of materials through the surprising thickness of the fully strained $Dy_2Ti_2O_7$ thin film.

The research presented in this thesis could be built upon along a number of different directions. The thick film work showed that $Dy_2Ti_2O_7$ thin films could be grown as single crystals to thicknesses greater than that of $Tb_2Ti_2O_7$ and $Yb_2Ti_2O_7$ while remaining fully strained. In the future, even thicker $Dy_2Ti_2O_7$ thin films could be grown in an attempt to find out the limit of how thick these films can be grown on $Y_2Ti_2O_7$ substrates, before the strain forces them to relax or create additional phases. Electrical conductivity experiments could be carried out to try and identify how the chemical makeup of the films change. It is known that the majority of the titanates' volume is made up of oxygen ions, and so the change in lattice constants may be a result of oxygen vacancies, which also impact a material's electrical conductivity [40].

It has been shown that it was a mistake to investigate the $Yb_2Ti_2O_7$ [111] film series since it failed to grow epitaxially. Both [100] and $[1\bar{1}0]$ films were successfully grown epitaxially, which opens up the possibility of investigating a thickness series of these films in the future. The work shown in this thesis has revealed that future growth of $Yb_2Ti_2O_7$ thin films would require purer $Y_2Ti_2O_7$ crystals. This has not been an issue before in characterising $Dy_2Ti_2O_7$ and $Tb_2Ti_2O_7$ thin films, but this may be due to their larger magnetic moments.

Hirschberger has reported that bulk $Tb_2Ti_2O_7$ has a large thermal Hall effect [44]. A future collaboration with Dr. Tom Fennell has been briefly discussed, which will attempt to explain or reproduce the reported results in a more insightful way. This experiment will involve using a novel technique and will compare the thin films with bulk $Tb_2Ti_2O_7$ crystals with and without disorder.

Appendix A

Maximum Measurable Magnetic Moment of Rare-Earth Titanates

The following calculation aims to calculate the maximum measurable magnetic moment of rare-earth titanates. The calculation assumes that that there is strong anisotropy along the $\langle 111 \rangle$ crystal directions such that its spins can be treated as Ising spins, which have only two states: up and down. The equation below shows how Ising spins change the theoretical maximum measurable magnetisation:

$$g^2 = g_{\parallel}^2 \cos^2\theta + g_{\perp}^2 \sin^2\theta$$

$$g_{\perp}^2 \sin^2\theta = 0$$

$$g = g_{\parallel} \cos\theta$$

The theoretical value is given by $g_{\parallel}$, the maximum possible measurable value is g, and so the average value of $\cos\theta$ must be found. The Ising spins point along the $\langle 111 \rangle$ set of crystal directions. The crystal directions in this set are $[111]$, $[\bar{1}11]$, $[1\bar{1}1]$ and $[11\bar{1}]$. To find the average value of $\cos\theta$, the contributions of each spin along each direction in the $\langle 111 \rangle$ set must be calculated. The dot product is used to find the proportion of the magnetic moment along each direction. It is unclear how the $\langle 111 \rangle$ set of crystal directions are oriented in relation to the crystal's tetrahedra and so the sign of each $\langle 111 \rangle$ set direction was chosen to give a positive value. This method calculates the maximum theoretically possible measurable value, rather than the theoretical measurable

value. In the examples displayed below, the theoretical $Yb_2Ti_2O_7$ g-factor of 4 has been used:

The maximum measurable magnetic moment along the [111] direction:

$$\pm \begin{bmatrix} 1 \\ 1 \\ 1 \end{bmatrix} \cdot \begin{bmatrix} 1 \\ 1 \\ 1 \end{bmatrix} = \frac{1}{3} + \frac{1}{3} + \frac{1}{3} = 1$$

$$\pm \begin{bmatrix} -1 \\ 1 \\ 1 \end{bmatrix} \cdot \begin{bmatrix} 1 \\ 1 \\ 1 \end{bmatrix} = -\frac{1}{3} + \frac{1}{3} + \frac{1}{3} = \frac{1}{3}$$

$$\pm \begin{bmatrix} 1 \\ -1 \\ 1 \end{bmatrix} \cdot \begin{bmatrix} 1 \\ 1 \\ 1 \end{bmatrix} = \frac{1}{3} - \frac{1}{3} + \frac{1}{3} = \frac{1}{3}$$

$$\pm \begin{bmatrix} 1 \\ 1 \\ -1 \end{bmatrix} \cdot \begin{bmatrix} 1 \\ 1 \\ 1 \end{bmatrix} = \frac{1}{3} + \frac{1}{3} - \frac{1}{3} = \frac{1}{3}$$

$$\cos\theta = \frac{1 + \frac{1}{3} + \frac{1}{3} + \frac{1}{3}}{4} = \frac{1}{2}$$

$$g = \frac{g_{\parallel}}{2} = 2\ \mu_{\mathrm{B}}$$

The maximum measurable magnetic moment along the $[\bar{1}\bar{1}2]$ direction:

$$\pm \begin{bmatrix} 1 \\ 1 \\ 1 \end{bmatrix} \cdot \begin{bmatrix} -1 \\ -1 \\ 2 \end{bmatrix} = 0 = \sqrt{3}\sqrt{6}\cos(\theta) => \cos(\theta) = 0$$

$$\pm \begin{bmatrix} -1 \\ 1 \\ 1 \end{bmatrix} \cdot \begin{bmatrix} -1 \\ -1 \\ 2 \end{bmatrix} = 1 - 1 + 2 = 2 = \sqrt{3}\sqrt{6}\cos(\theta) => \cos(\theta) = \frac{\sqrt{2}}{3}$$

$$\pm \begin{bmatrix} 1 \\ -1 \\ 1 \end{bmatrix} \cdot \begin{bmatrix} -1 \\ -1 \\ 2 \end{bmatrix} = -1 + 1 + 2 = \sqrt{3}\sqrt{6}\cos(\theta) => \cos(\theta) = \frac{\sqrt{(2)}}{3}$$

$$\pm \begin{bmatrix} 1 \\ 1 \\ -1 \end{bmatrix} \cdot \begin{bmatrix} -1 \\ -1 \\ 2 \end{bmatrix} = 1 + 1 + 2 = 4 = \sqrt{3}\sqrt{6}\cos(\theta) => \cos(\theta) = \frac{2\sqrt{2}}{3}$$

$$\cos\theta = \frac{0 + \frac{\sqrt{2}}{3} + \frac{\sqrt{2}}{3} + \frac{2\sqrt{2}}{3}}{4} = \frac{\sqrt{2}}{3}$$

$$g = \frac{\sqrt{2}g_{\|}}{3} = 1.886\ \mu_{\mathrm{B}}$$

The maximum measurable magnetic moment along the 010 direction:

$$\pm \begin{bmatrix} 1 \\ 1 \\ 1 \end{bmatrix} \cdot \begin{bmatrix} 0 \\ 1 \\ 0 \end{bmatrix} = 1 = \sqrt{3}\sqrt{1}\cos(\theta) => \cos(\theta) = \frac{1}{\sqrt{3}}$$

$$\pm \begin{bmatrix} -1 \\ 1 \\ 1 \end{bmatrix} \cdot \begin{bmatrix} 0 \\ 1 \\ 0 \end{bmatrix} = 1 = \sqrt{3}\sqrt{1}\cos(\theta) => \cos(\theta) = \frac{1}{\sqrt{3}}$$

$$\pm \begin{bmatrix} 1 \\ -1 \\ 1 \end{bmatrix} \cdot \begin{bmatrix} 0 \\ 1 \\ 0 \end{bmatrix} = 1 = \sqrt{3}\sqrt{1}\cos(\theta) => \cos(\theta) = \frac{1}{\sqrt{3}}$$

$$\pm \begin{bmatrix} 1 \\ 1 \\ -1 \end{bmatrix} \cdot \begin{bmatrix} 0 \\ 1 \\ 0 \end{bmatrix} = 1 = \sqrt{3}\sqrt{1}\cos(\theta) => \cos(\theta) = \frac{1}{\sqrt{3}}$$

$$\cos\theta = \frac{\frac{1}{\sqrt{3}} + \frac{1}{\sqrt{3}} + \frac{1}{\sqrt{3}} + \frac{1}{\sqrt{3}}}{4} = \frac{1}{\sqrt{3}}$$

$$g = \frac{g_{\|}}{\sqrt{3}} = 2.309\ \mu_{\mathrm{B}}$$

Appendix B

M vs H Fitting Equation

The derivation of the M vs H fitting equation is shown below, where M is the sample magnetisation, χ_{VV} is the Van Vleck susceptibility, H is the applied field, μ is the measured sample magnetic moment, n is the number of spin $\frac{1}{2}$ paramagnetic ions per unit volume (no distinction between film rare-earth ions and spin 1/2 magnetic impurities), B is the magnetic field, k_{B} is the Boltzmann constant and T is the sample temperature. The initial equation is broken into two terms. The first represents the Van Vleck contribution to the magnetisation and the second term represents the magnetisation of a spin $\frac{1}{2}$ paramagnet when it is inside of an applied field. The units of this equation are in A m^{-1}.

$$M = \chi_{\mathrm{VV}} H + \mu n \tanh\left(\frac{\mu B}{k_{\mathrm{B}} T}\right) \tag{B.1}$$

The magnetic moment is converted from A m^2 into Bohr magnetons through the substitution $\mu = \tilde{\mu}\mu_{\mathrm{B}}$, and B is converted to H using $B = \mu_0 (M + H)$ where $M = 0$.

$$M = \chi_{\mathrm{VV}} H + \tilde{\mu}\mu_{\mathrm{B}} n \tanh\left(\frac{\tilde{\mu}\mu_{\mathrm{B}}\mu_0 H}{k_{\mathrm{B}} T}\right) \tag{B.2}$$

In order to get a magnetic moment per Ti ion, n is substituted for $\tilde{n}n_0$ where $\tilde{n}$ represents the number of film ions (and/or defects) per titanium atom and n_0 represents the number of titanium atoms per unit volume. This is estimated as $n_0 = \frac{16}{10.1\times10^{-10}}$ m^{-3}, where 10.1×10^{-10} m is the sample's lattice constant and 16 refers to the number of Ti ions per unit cell.

$$M = \chi_{\mathrm{VV}} H + \tilde{\mu}\mu_{\mathrm{B}} \tilde{n} n_0 \tanh\left(\frac{\tilde{\mu}\mu_{\mathrm{B}}\mu_0 H}{k_{\mathrm{B}} T}\right) \tag{B.3}$$

The final step in this derivation groups together the constants to make c_1 and c_2, where $c_1 = \mu_B n_0 = 9.27 \times 10^{-24} \times \frac{16}{(10.1 \times 10^{-10})^3} = 1.44 \times 10^5$ and $c_2 = \frac{\mu_B \mu_0}{k_B} = \frac{9.27 \times 10^{-24} \times 1.26 \times 10^{-6}}{1.38 \times 10^{-23}} = 8.46 \times 10^{-7}$.

$$M = \chi_{VV} H + \tilde{\mu}\tilde{n} c_1 \tanh\left(\frac{\tilde{\mu} c_2 H}{T}\right) \tag{B.4}$$

The fitting parameters of this equation are χ_{VV}, $\tilde{\mu}$ and $\tilde{n}$.

Bibliography

[1] Bramwell S. T. & Gingras M. J. P., Spin ice state in frustrated magnetic pyrochlore materials, *Science* **294**, 14951501 (2001).

[2] Balents L. Spin liquids in frustrated magnets, *Nature* **464**, 199208 (2010).

[3] Pauling L., The Structure and Entropy of Ice and of Other Crystals with Some Randomness of Atomic Arrangement, *J. Am. Chem. Soc.* **57**, 26802684 (1935).

[4] Bovo L., Prabhakaran D., Soh Y.-A., Boothroyd A. T., Mathur N. D., Aeppli G. & Bramwell S. T., Restoration of the third law in spin ice thin films, *Nature Communications* **5**, 3439 (2014).

[5] Harris M. J, Bramwell S. T. & McMorrow D. F., Geometrical frustration in the ferromagnetic pyrochlore $Ho_2Ti_2O_7$, *Phys. Rev. Lett.* **79**, 36 (1997).

[6] Anderson P. W., Ordering and antiferromagnetism in ferrites, *Phys. Rev.* **102**, 10081013 (1956).

[7] Bramwell S. T. & Harris M. J., Frustration in Ising-type spin models on the pyrochlore lattice, *J. Phys. Condens. Matter* **10**, L215 - L220 (1998).

[8] Vojtěch Kaiser thesis, Dresden (2014).

[9] Siddharthan R., Shastry B. S., Ramirez A. P., Hayashi A., Cava R. J. & Rosenkranz S., Ising Pyrochlore Magnets: Low-Temperature Properties, "Ice Rules," and Beyond, *Phys. Rev. Lett.* **83**, 18541857 (1999).

[10] Den Hertog B. C. & Gingras M. J. P., Dipolar interactions and origin of spin ice in Ising pyrochlore magnets, *Phys. Rev. Lett.* **84**, 3430 - 3433 (2000).

[11] Fluri A., Schneider C. W. & Pergolesi D., Metal Oxide-Based Thin Film Structures, Chapter 5, 109 - 132 (2018).

[12] Bovo L., Rouleau C. M., Prabhakaran D. & Bramwell S. T., Layer-by-layer epitaxial thin films of the pyrochlore $Tb_2Ti_2O_7$, *Nanotechnology* **28**, 18 (2017).

[13] Sluis P. V. D., Determination of strain in epitaxial semiconductor layers by high-resolution x-ray diffraction, *J. Phys. D: Appl. Phys.* **26**, A188 - A191 (1993).

[14] Quantum Design Physical Property Measurement System Hardware Manual Part Number 1070-150, B5, San Diego (2008).

[15] Quantum Design Physical Property Measurement System Heat Capacity Option Users Manual Part Number 1085-150, H-1, San Diego (2004).

[16] Magnetic Property Measurement System Hardware Reference Manual. Quantum Design, San Diego CA., https://mmrc.caltech.edu/MPMS/Manuals/QD%20HWD%20Ref.pdf

[17] Duzer T.V., Turner C.W., Principles of Superconductive Devices and Circuits, Pearson Education Limited, (1999).

[18] Silver A. H., How the SQUID was born, *Supercond. Sci. Technol.* **19**, S173 - S178 (2006).

[19] B*ü*nzli J.-C. G., Benefiting from the Unique Properties of Lanthanide Ions, *Acc. Chem. Res.* **39**, 53-61 (2006).

[20] Martin R. B. & Richardson F. S., Lanthanides as probes for calcium in biological systems, *Quarterly Reviews of Biophysics* **12**, 181 - 209 (1979).

[21] Bramwell S. T. & Harris M. J., The history of spin ice, *J. Phys.: Condens. Matter* **32**, 374010 (2020).

[22] Barry K., Zhang B., Anand N., Xin Y., Vailionis A., Neu J., Heikes C., Cochran C., Zhou H., Qiu Y., Ratcliff W., Siegrist T. & Beekman C., Modification of spin-ice physics in $Ho_2Ti_2O_7$ thin films, *Phys. Rev. Materials* **3**, 084412 (2019).

[23] Jaubert L. D. C., Lin T., Opel T. S., Holdsworth P. C. W. & Gingras M. J. P., Spin ice Thin Film: surface-ordering, Emergent Square ice, and Strain Effects, *PRL* **118**, 207206 (2017).

[24] Twengstr*ö*m M., Henelius P. & Bramwell S. T., Screening and the Pinch Point Paradox in Spin Ice. *Phys. Rev. Research* **2**, 013305 (2020).

[25] Bramwell S. T., Field M. N., Harris M. J. & Parkin I. P., Bulk magnetizations of the heavy rare earth titanate pyrochloresa series of model frustrated magnets, *J. Phys.: Condens. Matter* **12**, 483495 (2000).

[26] Ramirez A. P., Hayashi A., Cava R. J., Siddharthan R. & Shastry B. S., Zero-point entropy in spin ice, *Nature* **399**, 333335 (1999).

[27] Bovo L., Jaubert L. D. C., Holdsworth P. C. W. & Bramwell S. T., Crystal shape-dependent magnetic susceptibility and Curie law crossover in the spin ices $Dy_2Ti_2O_7$ and $Ho_2Ti_2O_7$, *J. Phys.: Condens. Matter* **25**, 386002 (2013).

[28] Arroo D. M. & Bramwell S. T., Experimental measures of topological sector fluctuations in the F-model. *Phys. Rev. B* **102**, 214427 (2020).

[29] Arpino K. E., Trump B. A., Scheie A. O., McQueen T. M. & Koohpayeh, S. M., Impact of Stoichiometry of $Yb_2Ti_2O_7$ on its Physical Properties. *Phys. Rev. B.* **95**, 094407 (2017).

[30] Ross K. A., Savary L. Gaulin B. D. & Balents L., Quantum Excitations in Quantum Spin Ice. *Phys. Rev. X.* **1**, 021002 (2011).

[31] Chang L.-J., Onoda S., Su Y., Kao Y.-J., Tsuei K.-D., Yasui Y., Kakurai K. & Lees M. R., Higgs transition from a magnetic Coulomb liquid to a ferromagnet in $Yb_2Ti_2O_7$. *Nature Communications* **3**, 992 (2012).

[32] Scheie A., Kindervater J., Zhang S., Changlani H. J., Sala G., Ehlers G., Heinemann A., Tucker G. S., Koohpayeh S. M. & Broholm C., Multiphase magnetism in $Yb_2Ti_2O_7$. *PSNA* **117**, 27253 (2020).

[33] Blundred G. D., Bridges C. A. & Rosseinsky M. J., New Oxidation States and Defect Chemistry in the Pyrochlore Structure. *Angew. Chem. Int. Ed.* **43**, 3562-3565 (2004).

[34] Chapuis Y., Yaouanc A., De Réotier P. D., Marin C., Vanishri S., Curnoe S. H., Vâju C. & Forget A., Evidence from thermodynamic measurements for a singlet crystal-field ground state in pyrochlore $Tb_2Sn_2O_7$ and $Tb_2Ti_2O_7$, *Phys. Rev. B* **82**, 100402 (2010).

[35] Gaulin B. D., Gardner J. S., Mcclarty P. A. & Gingras M. J. P., Lack of evidence for a singlet crystal-field ground state in the magnetic pyrochlore $Tb_2Ti_2O_7$, *Phys. Rev. B* **84**, 140402 (2011).

[36] Hayward M. A., Phase Separation during the Topotactic Reduction of the Pyrochlore $Y_2Ti_2O_7$. *Chem. Mater.* **17**, 670-675 (2005).

[37] Jiang Y., Smith J. R. & Odette G. R., Prediction of structural, electronic and elastic properties of $Y_2Ti_2O_7$ and Y_2TiO_5, *Acta Materialia* **58**, 1536 - 1543 (2010).

[38] National Institute for Materials Science, NIMS Materials Database (MatNavi), Available from: https://crystdb.nims.go.jp/crystdb/search-materials

[39] Gingras M. J. P., Hertog B. C. D., Faucher M., Gardner J. S., Dunsiger S. R., Chang L. J., Gaulin B. D., Raju N. P., & Greedan J. E., Thermodynamic and single-ion properties of Tb^{3+} within the collective paramagnetic-spin liquid state of the frustrated pyrochlore antiferromagnet $Tb_2Ti_2O_7$. *Phys. Rev. B* **62**, 6496-6511 (2000).

[40] Mock J., Klingebiel B., Höhler F., Nuys M., Flohre J., Muthmann S., Kirchartz T. & Carius R., Oxygen vacancy doping of hematite analyzed by electrical conductivity and thermoelectric power measurements, *Phys. Rev. Materials* **1**, 065407 (2017).

[41] Kushkov V.D., Zaslavskii A.M. & Zverlin A.V., *Russ. J. Inorg. Chem.* **35**, 1406-1407 (1990)

[42] Byron C., Hertog D. & Gingras M. J. P., Dipolar interactions and origin of spin ice in ising pyrochlore magnets, *Phys. Rev. Lett.* **84**, 34303433 (2000).

[43] Catanese C. A., Skjeltorp A. T., Meissner H. E. & Wolf W. P., Magnetic and Thermal Properties of $Tb(OH)_3$, *Phys. Rev. B* **8**, (1973).

[44] Hirschberger M., Krizan J. W., Cava R. J. & Ong N. P., Large thermal Hall conductivity of neutral spin excitations in a frustrated quantum magnet, *SCIENCE* **348**, 6230 (2015).